ALMA SPECTROSCOPIC SURVEY IN THE HUBBLE ULTRA DEEP FIELD: THE INFRARED EXCESS OF UV-SELECTED $z = 2$–10 GALAXIES AS A FUNCTION OF UV-CONTINUUM SLOPE AND STELLAR MASS

Rychard J. Bouwens[1], Manuel Aravena[2], Roberto Decarli[3], Fabian Walter[3,4,5], Elisabete da Cunha[6,7], Ivo Labbé[1], Franz E. Bauer[8,9,10], Frank Bertoldi[11], Chris Carilli[5,12], Scott Chapman[13], Emanuele Daddi[14], Jacqueline Hodge[1], Rob J. Ivison[15,16], Alex Karim[11], Olivier Le Fevre[17], Benjamin Magnelli[11], Kazuaki Ota[12], Dominik Riechers[18], Ian R. Smail[19], Paul van der Werf[1], Axel Weiss[11], Pierre Cox[20], David Elbaz[14], Jorge Gonzalez-Lopez[8], Leopoldo Infante[8], Pascal Oesch[21], Jeff Wagg[22], and Steve Wilkins[23]

[1] Leiden Observatory, Leiden University, NL-2300 RA Leiden, Netherlands
[2] Núcleo de Astronomía, Facultad de Ingeniería, Universidad Diego Portales, Av. Ejército 441, Santiago, Chile
[3] Max-Planck Institut für Astronomie, Königstuhl 17, D-69117, Heidelberg, Germany
[4] Astronomy Department, California Institute of Technology, MC105-24, Pasadena, CA 91125, USA
[5] NRAO, Pete V. Domenici Array Science Center, P.O. Box O, Socorro, NM 87801, USA
[6] Centre for Astrophysics and Supercomputing, Swinburne University of Technology, Hawthorn, Victoria 3122, Australia
[7] Research School of Astronomy and Astrophysics, Australian National University, Canberra, ACT 2611, Australia
[8] Instituto de Astrofísica, Facultad de Física, Pontificia Universidad Católica de Chile, Casilla 306, Santiago 22, Chile
[9] Millennium Institute of Astrophysics (MAS), Nuncio Monseñor Sótero Sanz 100, Providencia, Santiago, Chile
[10] Space Science Institute, 4750 Walnut Street, Suite 205, Boulder, CO 80301, USA
[11] Argelander Institute for Astronomy, University of Bonn, Auf dem Hügel 71, D-53121 Bonn, Germany
[12] Cavendish Laboratory, University of Cambridge, 19 J. J. Thomson Avenue, Cambridge CB3 0HE, UK
[13] Dalhousie University, Halifax, Nova Scotia, Canada
[14] Laboratoire AIM, CEA/DSM-CNRS-Université Paris Diderot, Irfu/Service d'Astrophysique, CEA Saclay, Orme des Merisiers, F-91191 Gif-sur-Yvette cedex, France
[15] European Southern Observatory, Alonso de Cordova 3107, Casilla 19001, Vitacura Santiago, Chile
[16] Institute for Astronomy, University of Edinburgh, Royal Observatory, Blackford Hill, Edinburgh EH9 3HJ, UK
[17] IRAM, 300 rue de la piscine, F-38406 Saint-Martin d'Hères, France
[18] Cornell University, 220 Space Sciences Building, Ithaca, NY 14853, USA
[19] Centre for Extragalactic Astronomy, Department of Physics, Durham University, South Road, Durham DH1 3LE, UK
[20] Joint ALMA Observatory—ESO, Av. Alonso de Cordova, 3104, Santiago, Chile
[21] Astronomy Department, Yale University, New Haven, CT 06511, USA
[22] SKA Organisation, Lower Withington, Cheshire, UK
[23] Astronomy Centre, Department of Physics and Astronomy, University of Sussex, Brighton BN1 9QH, UK

ABSTRACT

We make use of deep 1.2 mm continuum observations (12.7 μJy beam^{-1} rms) of a 1 arcmin^2 region in the Hubble Ultra Deep Field to probe dust-enshrouded star formation from 330 Lyman-break galaxies spanning the redshift range $z = 2$–10 (to $\sim$2–3 $M_\odot$ yr^{-1} at 1σ over the entire range). Given the depth and area of ASPECS, we would expect to tentatively detect 35 galaxies, extrapolating the Meurer $z \sim 0$ IRX–β relation to $z \geqslant 2$ (assuming dust temperature $T_d \sim 35$ K). However, only six tentative detections are found at $z \gtrsim 2$ in ASPECS, with just three at $>3\sigma$. Subdividing our $z = 2$–10 galaxy samples according to stellar mass, UV luminosity, and UV-continuum slope and stacking the results, we find a significant detection only in the most massive ($>10^{9.75}$ $M_\odot$) subsample, with an infrared excess (IRX $= L_{\rm IR}/L_{\rm UV}$) consistent with previous $z \sim 2$ results. However, the infrared excess we measure from our large selection of sub-L^* ($<10^{9.75}$ $M_\odot$) galaxies is $0.11^{+0.32}_{-0.42} \pm 0.34$ (bootstrap and formal uncertainties) and $0.14^{+0.15}_{-0.14} \pm 0.18$ at $z = 2$–3 and $z = 4$–10, respectively, lying below even an IRX–β relation for the Small Magellanic Cloud (95% confidence). These results demonstrate the relevance of stellar mass for predicting the IR luminosity of $z \gtrsim 2$ galaxies. We find that the evolution of the IRX–stellar mass relationship depends on the evolution of the dust temperature. If the dust temperature increases monotonically with redshift ($\propto (1 + z)^{0.32}$) such that $T_d \sim 44$–50 K at $z \geqslant 4$, current results are suggestive of little evolution in this relationship to $z \sim 6$. We use these results to revisit recent estimates of the $z \geqslant 3$ star formation rate density.

Key words: galaxies: evolution – galaxies: ISM – galaxies: star formation – galaxies: statistics – instrumentation: interferometers – submillimeter: galaxies

1. INTRODUCTION

One particularly interesting and long-standing focus of galaxy studies has been quantifying the total energy output and stellar birth rate in galaxies across cosmic time. The first significant investigations became possible following systematic searches for galaxies to intermediate and high redshifts, $z \sim 3$–4 (Lilly et al. 1996; Madau et al. 1996). The immediate picture was that the star formation rate (SFR) density likely peaked around $z \sim 2$–4 (Madau et al. 1996; Steidel et al. 1999).

Using photometric searches for Lyman-break galaxies at $z > 4$, it later became clear that there was a significant drop in the SFR density to $z > 4$ (Dickinson 2000; see review by Madau & Dickinson 2014). Rough constraints now exist on the SFR density to $z \sim 10$ (e.g., Bouwens et al. 2011, 2015a; Ellis et al. 2013; Oesch et al. 2014, 2015; McLeod et al. 2015; Laporte et al. 2016).

In spite of huge progress in mapping the SFR density from $z \sim 0$ to $z \sim 11$ from surveys in the rest-frame UV, our understanding of the energy output from UV-selected galaxies

at far-infrared wavelengths is most developed over the redshift range $z \sim 0$ to $z \sim 3$, with increasing maturity (Reddy et al. 2008; Daddi et al. 2009; Magnelli et al. 2009, 2011, 2013; Karim et al. 2011; Cucciati et al. 2012; Álvarez-Márquez et al. 2016). This general picture of the energy output from galaxies at rest-frame UV and far-IR wavelengths has been confirmed by many independent probes at X-ray and radio wavelengths and using the Hα emission line, with consistent results (e.g., Reddy & Steidel 2004; Reddy et al. 2006, 2010; Erb et al. 2006b; Daddi et al. 2007).

The observational situation becomes much more uncertain when one considers dust-enshrouded star formation at $z > 3$, as use of standard techniques or facilities becomes more difficult (owing to the features from polycyclic aromatic hydrocarbons shifting out of the *Spitzer*/MIPS 24 μm band or increasing source confusion in *Spitzer* or *Herschel* 70–500 μm observations), effectively limiting studies to the brightest, most intensely star-forming sources at $z > 3$ (e.g., HFLS3: Riechers et al. 2013). As a result of these challenges, various researchers (e.g., Meurer et al. 1999 [M99]; Reddy et al. 2006; Bouwens et al. 2007, 2009, 2012; Daddi et al. 2007) have made use of well-known $z \sim 0$ correlations, i.e., the relationship between infrared excess (IRX = L_{IR}/L_{UV}) and UV-continuum slope (β), to estimate dust extinction in more typical $z \geqslant 3$ galaxies based on the UV slopes measured from the observed UV data. Such correlations have been confirmed to apply out to $z \sim 2$ using a variety of multi-wavelength data (Reddy et al. 2006, 2008; Daddi et al. 2007, 2009; Pannella et al. 2009), but it is unclear if they apply at $z \geqslant 3$.

Despite the power of stacking, e.g., with the SCUBA-2 or *Herschel* data, more direct measurements of the dust-enshrouded star formation have required the advent of some new or upgraded facilities (e.g., Atacama Large Millimeter Array (ALMA), NORthern Extended Millimeter Array (NOEMA)). The first results from these facilities indicated that there was no detectable dust-enshrouded star formation in normal or even extremely bright UV-selected $z > 5$ galaxies (Walter et al. 2012; Ouchi et al. 2013; González-López et al. 2014; Ota et al. 2014; Riechers et al. 2014; Maiolino et al. 2015). Later, some bright $z \sim 5$–6 galaxies were weakly detected in the far-IR continuum (Capak et al. 2015; Willott et al. 2015), but at lower levels than seen in similar galaxies at lower redshifts using well known lower-redshift $z \sim 0$–2 IRX–β relations.

While current results generally suggest much lower dust emission from $z > 3$ galaxies than expected based on $z = 0$–2 IRX–β relations, the number of $z > 3$ sources where such constraints are available remains modest. This is especially the case when one considers only sources that can be confidently placed in $z > 3$ samples and have accurately measured UV continuum slopes, stellar masses, or SFRs. As such, it is clearly helpful to obtain deep continuum observations with ALMA over fields with substantial amounts of legacy observations at other wavelengths from the *Hubble Space Telescope* (*HST*), *Spitzer*, *Herschel*, and ground-based observatories.

Fortunately, with our recent 20 hr, 1.2 mm ALMA program (2013.1.00718.S: Papers I and II in the ALMA Spectroscopic Survey in the HUDF (ASPECS) series (Walter et al. 2016; Aravena et al. 2016a), we were able to acquire very deep continuum observations over a 1 arcmin^2 region of the sky with high-quality multi-wavelength observations. That region was the Hubble Ultra Deep Field (HUDF: Beckwith et al. 2006;

Xue et al. 2011; Illingworth et al. 2013), containing the most sensitive ultraviolet, optical, near-infrared, X-ray, and radio observations available anywhere on the sky (Bouwens et al. 2011; Xue et al. 2011; Ellis et al. 2013; Illingworth et al. 2013; Teplitz et al. 2013; Rujopakarn et al. 2016). Our new observations (12.7 μJy beam^{-1}) were sufficiently deep to probe to an almost-constant dust-enshrouded SFR of 4 $M_\odot$ yr^{-1} at 2σ from $z \sim 2$ to $z \sim 10$ over the field (for dust temperature $T_d \sim 35$ K), allowing us to obtain a census of such star formation over a substantial volume ($\sim 2 \times 10^4$ Mpc^3) in the early universe.

With these deep ALMA observations, we have the capacity not only to detect dust emission from individual sources to almost unprecedented limits, but also to systematically measure how the dust-enshrouded SFRs in galaxies depend on redshift, stellar mass, and UV-continuum slope β. In an earlier paper in this series (Paper II: Aravena et al. 2016a), we identified all those sources that showed significant individual detections ($>3.5\sigma$) in our 1 arcmin^2 mosaic and briefly examined the characteristics of the detected sources, noting that the mean redshift of those sources was approximately $z \sim 1.5$. We also considered stacks of various sources over this field, subdividing these samples by redshift, stellar mass, and SFR. We demonstrated that by combining the individual detections in ASPECS with the stacked measures we could match the measured cosmic background at 1.2 mm.

The purpose of this paper (Paper VI in the ASPECS series) is to focus in particular on the infrared excess (L_{IR}/L_{UV}) of $z = 2$–10 galaxies over our 1 arcmin^2 field and to quantify the dependence of this excess on stellar mass and UV-continuum slope β. Over the 1 arcmin^2 ASPECS field, we have sufficient $z = 2$–10 sources, i.e., ~ 330 in total, to attempt a first exploration of the IRX–β and IRX–stellar mass relations at $z > 2$ for normal galaxies. We can also investigate quantitatively whether the IRX–β relationship shows a dependence on stellar mass and how strong that dependence is (if it exists). Previous work (e.g., Baker et al. 2001; Reddy et al. 2006; Siana et al. 2008, 2009; Álvarez-Márquez et al. 2016) has presented seemingly compelling evidence for such a dependence, with higher- and lower-mass galaxies showing an M99 and a Small Magellanic Cloud (SMC) IRX–β relationship, respectively.[24] However, most of these studies have not extended into the mass regime that we explore with the present data set and have not extended out to $z \geqslant 3$.

The outline of the paper is as follows. We begin with a description of the ASPECS 1.2 mm data set that we employ for this study, our procedure for constructing $z = 2$–10 samples from the HUDF data, and finally our derivation of stellar population parameters for individual sources (Section 2). In Section 3, we discuss the number of $z = 2$–10 galaxies that we would expect to individually detect based on $z = 0$–2 results, compare that with what we find, and then finally measure the stacked signal from the observations, subdividing the samples according to stellar mass, UV-continuum slope β, and apparent magnitude. We discuss our results in Section 4 and their likely implications in Section 5. Finally, Section 6 summarizes our results and the most important conclusions.

---

[24] Reddy et al. (2006) frame the dependence of the IRX–β relation in terms of the stellar population age of a galaxy. Sources with ages <100 Myr and >100 Myr were found to show SMC and M99 IRX–β relations, respectively. In the context of the samples of Reddy et al. (2006), stellar population age is functionally equivalent to stellar mass.

Table 1
2σ Sensitivity Limits for our Probe of Obscured Star Formation from Individual $z \gtrsim 2$ Galaxies and the Dependence on SED

Far-Infrared SED Model	2σ Sensitivity Limits ($10^{10}\ L_\odot$)								
	$z \sim 2$	$z \sim 3$	$z \sim 4$	$z \sim 5$	$z \sim 6$	$z \sim 7$	$z \sim 8$	$z \sim 9$	$z \sim 10$
35 K modified blackbody[a] (*fiducial*)	5.0	4.4	4.0	3.7	3.7	3.8	4.2	4.8	6.0
Modified blackbody with evolving T_d[b]	6.3	7.8	8.8	9.5	10.1	10.2	9.5	9.2	9.1
25 K modified blackbody[a]	1.4	1.4	1.4	1.6	1.9	2.7	4.1	6.9	12.3
30 K modified blackbody[a]	2.7	2.5	2.4	2.4	2.5	2.9	3.6	4.9	7.0
40 K modified blackbody[a]	8.5	7.3	6.3	5.7	5.3	5.2	5.3	5.7	6.4
45 K modified blackbody[a]	13.9	11.6	9.8	8.5	7.7	7.3	7.1	7.2	7.5
50 K modified blackbody[a]	21.6	17.6	14.6	12.4	11.0	10.1	9.5	9.3	9.3
NGC 6946[c]	1.3	1.3	1.4	1.6	1.9	2.5	3.5	5.4	8.7
M51[c]	1.4	1.4	1.5	1.6	1.9	2.5	3.4	5.2	8.2
Arp 220[c]	7.4	6.6	6.1	5.6	5.4	5.5	5.7	5.9	6.6
M82[c]	11.8	10.4	9.4	8.7	8.4	8.4	8.6	9.1	9.9
SED Model	2σ Limit for Probes of the Obscured SFR ($M_\odot\ \mathrm{yr}^{-1}$)[d]								
	$z \sim 2$	$z \sim 3$	$z \sim 4$	$z \sim 5$	$z \sim 6$	$z \sim 7$	$z \sim 8$	$z \sim 9$	$z \sim 10$
35 K modified blackbody[a] (*fiducial*)	5.0	4.4	4.0	3.7	3.7	3.8	4.2	4.8	6.0
Modified blackbody with evolving T_d[b]	6.3	7.8	8.8	9.5	10.1	10.0	9.4	9.0	8.9
25 K modified blackbody[a]	1.4	1.4	1.4	1.6	1.9	2.7	4.1	6.9	12.3
30 K modified blackbody[a]	2.7	2.5	2.4	2.4	2.5	2.9	3.6	4.9	7.0
40 K modified blackbody[a]	8.5	7.3	6.3	5.7	5.3	5.2	5.3	5.7	6.4
45 K modified blackbody[a]	13.9	11.6	9.8	8.5	7.7	7.3	7.1	7.2	7.5
50 K modified blackbody[a]	21.6	17.6	14.6	12.4	11.0	10.1	9.5	9.3	9.3
NGC 6946[c]	1.3	1.3	1.4	1.6	1.9	2.5	3.5	5.4	8.7
M51[c]	1.4	1.4	1.5	1.6	1.9	2.5	3.4	5.2	8.2
Arp 220[c]	7.4	6.6	6.1	5.6	5.4	5.5	5.7	5.9	6.6
M82[c]	11.8	10.4	9.4	8.7	8.4	8.4	8.6	9.1	9.9

Notes.
[a] Standard modified blackbody form (e.g., Casey 2012) with a power-law spectral index for the dust emissivity of $\beta_d = 1.6$ (Eales et al. 1989; Klaas et al. 1997).
[b] Assuming dust temperature T_d evolves as $(35\ \mathrm{K})((1+z)/2.5)^{0.32}$ (Béthermin et al. 2015) such that $T_d \sim 44$–50 K at $z \sim 4$–6. See Section 3.1.3.
[c] Empirical SED template fits to specific galaxies in the nearby universe (Silva et al. 1998).
[d] Using the conversion SFR $= L_{IR}/(10^{10}\ L_\odot)$ appropriate for a Chabrier IMF (Kennicutt 1998; Carilli & Walter 2013).

We refer to the *HST* F225W, F275W, F336W, F435W, F606W, F600LP, F775W, F814W, F850LP, F105W, F125W, F140W, and F160W bands as UV_{225}, UV_{275}, U_{336}, B_{435}, V_{606}, V_{600}, i_{775}, I_{814}, z_{850}, Y_{105}, J_{125}, JH_{140}, and H_{160}, respectively, for simplicity. For consistency with previous work, we find it convenient to quote results in terms of the luminosity $L^*_{z=3}$ that Steidel et al. (1999) derived at $z \sim 3$, i.e., $M_{1700,AB} = -21.07$. Throughout the paper we assume a standard "concordance" cosmology with $H_0 = 70$ km s^{-1} Mpc^{-1}, $\Omega_m = 0.3$, and $\Omega_\Lambda = 0.7$, which are in good agreement with recent cosmological constraints (Planck Collaboration et al. 2015). Stellar masses and obscured SFRs are quoted assuming a Chabrier (2003) initial mass function (IMF) while the SFR density is presented adopting a Salpeter (1955) IMF. Magnitudes are in the AB system (Oke & Gunn 1983).

2. OBSERVATIONS AND SAMPLE

2.1. Band-6 Data Set and Flux Measurements

The principal data used are the ALMA observations from the 2013.1.00718.S program (PI: Aravena) over the HUDF. Those observations were obtained through a full frequency scan in band 6 (212–272 GHz) with ALMA in its most compact configuration. The observations are distributed over seven pointings and cover an approximate area of ~ 1 arcmin^2 to near uniform depth. As described in Paper II (Aravena et al. 2016a), we collapsed our spectral data cube along the frequency axis in the *uv*-plane, inverting the visibilities using the CASA task

CLEAN using natural weighting and mosaic mode, to produce the continuum image. The peak sensitivity we measure in these continuum observations is $12.7\ \mu$Jy (1σ) per primary beam. Our observations fall within the region of the HUDF that possesses the deepest UV, optical, and near-infrared observations (see Illingworth et al. 2013; Teplitz et al. 2013).

The sensitivity of our ALMA observations allows us to provide useful individual constraints on the far-IR dust emission from normal sub-L^* galaxies. If we adopt a modified blackbody form for the shape of the spectral energy distribution (SED) with a dust temperature of 35 K and a power-law spectral index for the dust emissivity of $\beta_d = 1.6$ (Eales et al. 1989; Klaas et al. 1997), and account for the impact of the cosmic microwave background (CMB) (e.g., da Cunha et al. 2013b: Section 3.1.1), we estimate that we should be able to tentatively detect at 2σ any star-forming galaxy at $z > 3$ with an IR luminosity (8–1000 μm rest-frame) in excess of $4 \times 10^{10}\ L_\odot$ (see Table 1 and Figure 1). For comparison, the characteristic luminosity of galaxies in the rest-frame UV is approximately equal to $4 \times 10^{10}\ L_\odot$ from $z \sim 3$ to $z \sim 8$. The implication is that the typical L^* galaxy should be tentatively detected at $\gtrsim 2\sigma$ in our data set if it were outputting equal amounts of energy in the far-IR and rest-frame UV.

We consider tentative 2σ detections in our examination of our ASPECS field, instead of the usual 3σ or 3.5σ limit, to push as faint as possible in looking for evidence of obscured star formation. We can use this aggressive limit because of the relatively modest number of $z = 2$–10 sources over ASPECS
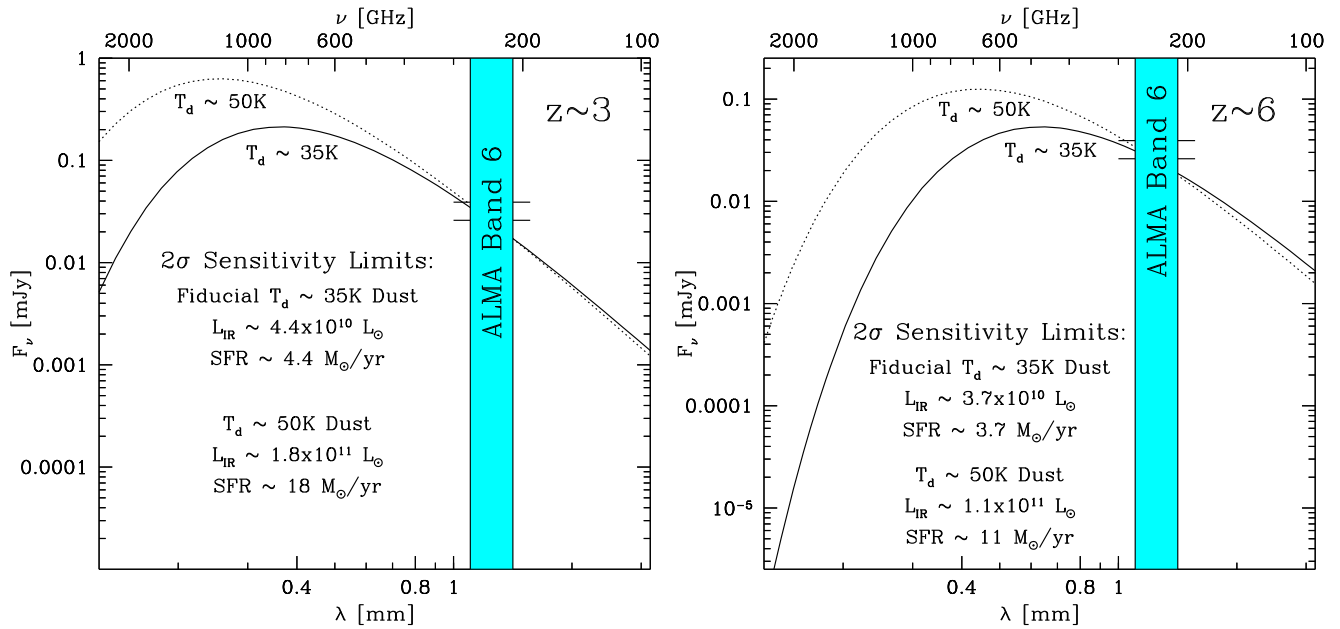
Figure 1. Model SEDs in the far-IR for the faintest $z \sim 3$ and $z \sim 6$ galaxies for which we would be able to obtain tentative individual detections ($>2\sigma$) in our deep ALMA band-6 observations. The plotted SEDs are modified blackbody SEDs with a dust temperature of 35 K and a power-law spectral index for the dust emissivity of $\beta_d = 1.6$ (Eales et al. 1989; Klaas et al. 1997). The two short horizontal lines at 1.2 mm show our 2σ and 3σ sensitivity limits. At both $z \sim 3$ and $z \sim 6$, we would expect to tentatively detect individual galaxies to approximately the same IR luminosity, $\sim 4 \times 10^{10} L_\odot$, which is equivalent to an obscured star formation rate (SFR) of $\sim 4 M_\odot \, \mathrm{yr}^{-1}$. For galaxies with dust temperatures of 50 K, we would expect to tentatively detect galaxies to IR luminosities of $\sim 1.8 \times 10^{11} L_\odot$ and $\sim 1.1 \times 10^{11} L_\odot$ at $z \sim 3$ and $z \sim 6$, equivalent to obscured SFRs of ~ 18 and $\sim 11 M_\odot \, \mathrm{yr}^{-1}$, respectively. These sensitivities account for the impact of the CMB (da Cunha et al. 2013b).

and the availability of sensitive MIPS 24 μm observations and photometrically inferred physical properties to evaluate any tentative detections.

To ensure accurate far-IR flux measurements for sources over our HUDF mosaic, care was taken in determining the offset between the nominal sky coordinates for sources in our deep ALMA continuum observations and the positions in the ultraviolet, optical, and near-IR observations using the six best-continuum-detected sources over the HUDF (Aravena et al. 2016a). The positional offset between the images was found to be such that sources in our ALMA continuum image were positioned $\sim 0\farcs3$ to the south of sources in the *HST* mosaic, with $\sim 0\farcs2$ source-to-source scatter in the derived offset. Such source-to-source offsets from UV to far-IR are not surprising for bright sources, but are expected to be smaller for most of the fainter sources we are stacking, as the results we present in Section 3.2 indicate. Overall, on the basis of the source-to-source scatter, we estimate that we can register the *HST* and ALMA mosaics to better than $0\farcs1$ on average.

Flux measurements themselves were made using the nominal flux at the position of the source in the continuum map divided by the primary beam. We checked those flux measurements against those we derive after convolving the maps by the primary beam and looking at the flux at source center. For this latter procedure, we found that we recovered a flux that was less than 5% higher than using the flux at the position of the source.

For a more detailed summary of the ASPECS data set and the basic results, we refer the reader to Papers I and II in this series (Walter et al. 2016; Aravena et al. 2016a). Paper V in this series (Aravena et al. 2016b) provides a comprehensive discussion of the candidate [C II] 158 μm lines identified in the band-6 data.

2.2. Samples of Lyman-break Galaxies

The high-redshift star-forming galaxies that we analyzed in this study were selected for this study using the best existing *HST* observations over the HUDF.

We briefly describe the $z = 1.5$–3.5 samples that we constructed over the HUDF using the available WFC3/UVIS, ACS/WFC, and WFC3/IR observations. For *HST* optical ACS/WFC and near-infrared WFC3/IR observations, we make use of the XDF reductions (Illingworth et al. 2013), which incorporated all ACS+WFC3/IR data available over the HUDF in 2013. The XDF reductions are ~ 0.1–0.2 mag deeper than original reductions of Beckwith et al. (2006) at optical wavelengths and also provide coverage in the F814W band. The WFC3/IR reductions made available as part of the XDF release include all data from the original HUDF09 (Bouwens et al. 2011), CANDELS (Grogin et al. 2011; Koekemoer et al. 2011), and HUDF12 (Ellis et al. 2013) programs.

In the process of assembling our $z = 1.5$–3.5 samples, we derived our initial source catalogs and performed photometry on sources using our own modified version of the SExtractor (Bertin & Arnouts 1996) software. Source detection was performed on the square root of χ^2 image (Szalay et al. 1999: similar to a coadded image) constructed from the V_{606}, i_{775}, Y_{105}, J_{125}, JH_{140}, and H_{160} images. After correcting fluxes for point-spread function (PSF) to match the H_{160}-band image, color measurements were made in scalable apertures in the style of Kron (1980) with a Kron factor of 1.6. "Total magnitude" fluxes were derived from the smaller scalable apertures by (1) correcting the flux to account for the additional flux seen in a larger scalable aperture (Kron factor of 2.5) as seen on the square root of χ^2 image and (2) correcting for the flux outside these larger scalable apertures and on the wings of

the PSF using tabulations of the encircled energy (Dressel et al. 2012).

Galaxies at intermediate redshift $z \sim 2–3$ were selected by applying simple two-color criteria using the Lyman-break galaxy (LBG) strategy:

$$(UV_{275} - U_{336} > 1) \wedge (U_{336} - B_{435} < 1) \wedge$$
$$(V_{606} - Y_{105} < 0.7) \wedge (S/N(UV_{225}) < 1.5)$$

for $z \sim 2$ galaxies and

$$(U_{336} - B_{435} > 1) \wedge (B_{435} - V_{606} < 1.2) \wedge$$
$$(i_{775} - Y_{105} < 0.7) \wedge (\chi^2_{UV_{225}, UV_{275}} < 2)$$

for $z \sim 3$ galaxies, where $\wedge$, $\vee$, and S/N represent the logical AND, OR symbols, and signal-to-noise in our smaller scalable apertures, respectively. We define $\chi^2_{UV_{225}, UV_{275}}$ as $\Sigma_i \text{SGN}(f_i)(f_i/\sigma_i)^2$ where f_i is the flux in bands UV_{225} and UV_{275} in a small scalable aperture, σ_i is the uncertainty in this flux, and $\text{SGN}(f_i)$ is equal to 1 if $f_i > 0$ and -1 if $f_i < 0$. These criteria are similar to the two-color criteria previously utilized in Oesch et al. (2010) and Hathi et al. (2010).

Our $z = 4–8$ samples were drawn from the samples of Bouwens et al. (2015a) and include all $z = 3.5–8.5$ galaxies located over the 1 arcmin^2 ASPECS region. The samples of Bouwens et al. (2015a) were based on the deep optical ACS and WFC3/IR observations within the HUDF. $z = 4–8$ samples were constructed by applying Lyman-break-like color criteria to the XDF reduction (Illingworth et al. 2013) of the HUDF.

The $z = 9–10$ samples of R. J. Bouwens et al. (2016, in preparation) were constructed applying a Y_{105} or J_{125}-dropout Lyman-break color criterion to the available *HST* data and then splitting the selected sources into $z \sim 9$ and $z \sim 10$ subsamples. Two sources from that $z = 9–10$ sample lie within the ASPECS region (see also Bouwens et al. 2011; Ellis et al. 2013; Oesch et al. 2013b).

To maximize the total number of star-forming galaxies at $z \sim 2–10$ considered in this study, we also applied the EAZY photometric redshift code to the *HST* WFC3/UVIS, ACS, and WFC3/IR photometric catalogs we had available over our deep ALMA field and included all sources with a best-fit redshift solution between $z \sim 1.5$ and $z \sim 8.5$, which were not in our Lyman-break catalogs, and which utilized star-forming or dusty SED templates to reproduce the observed SED. We also made use of the photometric catalog of Rafelski et al. (2015) and included those sources in our samples, if not present in our primary two selections.

The star-forming galaxies selected by photometric redshift added 64, 31, 2, and 1 $z \sim 2$, $z \sim 3$, $z \sim 4$, and $z \sim 7$ galaxies to our study, respectively. Sources in our photometric-redshift selections showed almost identical distributions of properties to our LBG selections at $z \sim 2–3$ (where our photometric-redshift selections add sources), with a median β and stellar mass of -1.84 and $10^{8.41}$ $M_\odot$ for the photometric-redshift selections versus -1.82 and $10^{8.37}$ $M_\odot$ for the $z \sim 2–3$ LBG selections. 9% (7/79) and 3% (3/96) of the sources in our LBG and photometric-redshift selections, respectively, have measured β's redder than -1.

Eighty-one $z \sim 2$ and 81 $z \sim 3$ sources in total were identified using our dropout + photometric-redshift criteria over the 1 arcmin^2 region of the HUDF where we have deep ALMA observations. Our higher-redshift $z \sim 4$, $z \sim 5$, $z \sim 6$,

Table 2
Number of UV-selected $z \sim 2$, $z \sim 3$, $z \sim 4$, $z \sim 5$, $z \sim 6$, $z \sim 7$, $z \sim 8$, $z \sim 9$, and $z \sim 10$ Galaxies Located within our Deep ALMA HUDF Pointing

Redshift	Selection Criterion	# of Sources	Ref.[a]
$z \sim 2$	UV_{275}-dropout or 1.5 < z_{phot} < 2.5	81	This work
$z \sim 3$	U_{336}-dropout or 2.5 < z_{phot} < 3.5	81	This work
$z \sim 4$	B_{435}-dropout or 3.5 < z_{phot} < 4.5	80	B15/This work
$z \sim 5$	V_{606}-dropout	34	B15
$z \sim 6$	i_{775}-dropout	30	B15
$z \sim 7$	z_{850}-dropout or 6.5 < z_{phot} < 7.5	16	B15/This work
$z \sim 8$	Y_{105}-dropout	6	B15
$z \sim 9$	Y_{105}-dropout	1	B16
$z \sim 10$	J_{125}-dropout	1	B16
	Total	330	

Note.
[a] References: B15—Bouwens et al. (2015a), B16—R. J. Bouwens et al. (2016, in preparation)

$z \sim 7$, $z \sim 8$, $z \sim 9$, and $z \sim 10$ samples (Bouwens et al. 2015a, 2016, in preparation) contain 80, 34, 30, 16, 6, 1, and 1 sources, respectively (Table 2) over this same region. The expected contamination rate in these color-selected samples by lower-redshift galaxies (or stars) is estimated to be of the order of 3%–8% (e.g., Bouwens et al. 2015a). In terms of apparent magnitude in the UV continuum, these sources extend from 21.7 mag to 30.8 mag (Figure 2: *left panel*).

2.3. Estimates of the Stellar Mass for Individual Sources in our z = 2–10 Sample

We provide a brief description of our estimates of the stellar mass for $z = 2–10$ sources over the HUDF. As in other work (e.g., Sawicki & Yee 1998; Brinchmann & Ellis 2000; Papovich et al. 2001; Labbé et al. 2005; Gonzalez et al. 2014), we estimate stellar masses for individual sources in our samples by modeling the observed photometry using stellar population libraries and considering variable (or fixed) star formation histories, metallicities, and dust content.

For convenience, we make use of the publicly available code FAST (Kriek et al. 2009) to perform this fitting. We assume a Chabrier (2003) IMF, a metallicity of 0.2 $Z_\odot$, an approximately constant SFR in modeling the star formation history while performing the fits (keeping the parameter τ equal to 100 Gyr where the star formation history is proportional to $e^{-t/\tau}$), and we allow the dust extinction in the rest-frame V band to range from zero to 2 mag. Our fixing the fiducial metallicity to 0.2 $Z_\odot$ is well motivated based on studies of the metallicity of individual $z \sim 2–4$ galaxies (Pettini et al. 2000) or as predicted from cosmological hydrodynamical simulations (Finlator et al. 2011; Wise et al. 2012). While the current choice of parameters can have a sizeable impact on inferred quantities such as the age of a stellar population (changing by >0.3–0.5 dex), these choices typically do not have a major impact ($\gtrsim 0.2$ dex) on the inferred stellar masses.

In deriving the stellar masses for individual sources, we made use of flux measurements from 11 *HST* bands (UV_{225}, UV_{275}, U_{336}, B_{435}, V_{606}, i_{775}, z_{850}, Y_{105}, J_{125}, JH_{140}, H_{160}), one
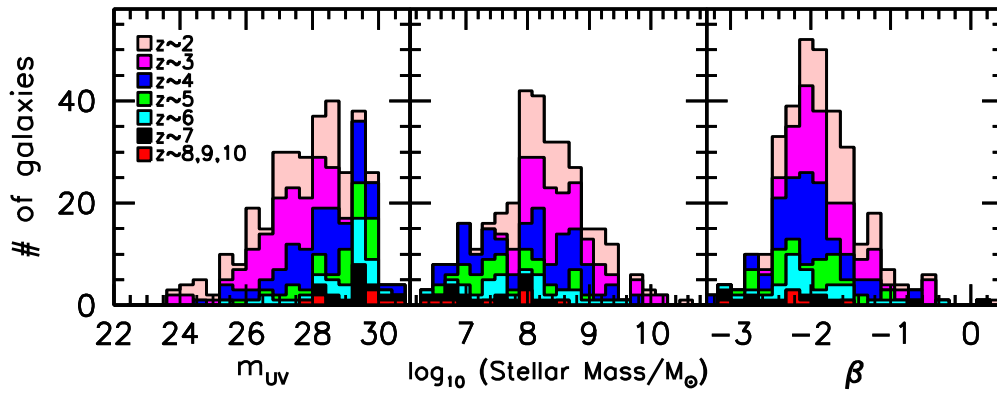
Figure 2. Cumulative histograms showing the composition of the HUDF $z \sim 2$, $z \sim 3$, $z \sim 4$, $z \sim 5$, $z \sim 6$, $z \sim 7$, and $z \sim 8$–10 samples that we consider here (*pink, magenta, blue, green, cyan, black,* and *red* shaded histograms, respectively) as a function of apparent magnitude (measured at wavelengths probing the UV continuum), stellar mass, and UV-continuum slope β (*left, central,* and *right* panels, respectively). The deep far-IR continuum observations (12.7 μJy beam^{-1} rms) from ASPECS make it possible for us to set the best constraints on the average dust emission from ($m_{UV} > 25$, $<10^{10} M_{\odot}$) galaxies thus far.

band in the near-IR from the ground (K_s), and four *Spitzer*/IRAC bands (3.6 μm, 4.5 μm, 5.8 μm, and 8.0 μm). The *HST* photometry we use for estimating stellar masses was derived by applying the same procedure as used for selecting our $z \sim 2$–3 LBG samples (see Section 2.2).

Our *Spitzer*/IRAC flux measurements were derived for individual sources from ~100–200 hr stacks of the IRAC observations over the HUDF (Labbé et al. 2015) from the IUDF program (PI: Labbé) and the *Spitzer*/IRAC program of Oesch et al. (2013a). As has become standard procedure (e.g., Labbé et al. 2005, 2015; Shapley et al. 2005; Grazian et al. 2006; Laidler et al. 2007; Merlin et al. 2015), we use the *HST* observations as a template to model the fluxes of sources in the *Spitzer*/IRAC observations and thus perform photometry below the nominal confusion limit. The model flux from neighboring sources is subtracted before attempting to measure fluxes for the sources of interest. Source photometry is performed in 1″8 diameter circular apertures for the *Spitzer*/IRAC 3.6 μm and 4.5 μm bands and 2″0 diameter circular apertures for the 5.8 μm and 8.0 μm bands. The observed fluxes are corrected to the total based on the inferred growth curve for sources after PSF correction to the *Spitzer*/IRAC PSF. We utilize a similar procedure to derive fluxes for sources based on the deep ground-based K-band observations available from VLT/HAWK-I, VLT/ISAAC, and PANIC observations (Fontana et al. 2014) over the HUDF (5σ depths of 26.5 mag).

A modest correction is made to the IRAC 3.6 μm and 4.5 μm photometry to account for the impact of nebular emission lines on the observed IRAC fluxes, decreasing the brightness of the 3.6 μm and 4.5 μm band fluxes by 0.32 mag to account for the presence of Hα and by 0.4 mag to account for the presence of [O III]+Hβ emission where present. These corrections are well motivated based on observations of $z \sim 4$–8 galaxies (Labbé et al. 2013; Stark et al. 2013; Smit et al. 2014, 2015; Marmol-Queralto et al. 2016; Rasappu et al. 2016) and lower the median inferred stellar mass for $z > 3.8$ galaxies in our sample by ~0.1 dex.

The stellar masses we estimate for the highest-redshift sources in our selection, $z > 5$, are not as well constrained as at lower redshifts, where our sensitive photometry extends to rest-frame 1 μm. To guard against noise in the modeling process scattering lower-mass galaxies into higher-mass bins, we also model the photometry of galaxies and force the dust extinction to be zero in fitting the observed SEDs with FAST. For sources

where the stellar-mass estimates exceed the dust-free stellar-mass estimates by more than 0.9 dex and the photometric evidence for a particularly dusty SED was weak (applicable to only six sources from our total sample of 330 sources), we made use of the dust-free stellar mass estimates instead.

We also estimated stellar masses for our sources by using the MAGPHYS software (da Cunha et al. 2008) to model the photometry for the 330 $z = 2$–10 sources that make up our samples. For sources with redshifts $z < 3.8$, the stellar masses we estimated were in excellent agreement with our fiducial results, with the median and mean stellar mass derived by MAGPHYS being 0.02 dex and 0.04 dex lower, respectively. This points toward no major systematic biases in the results from the present study—which rely on FAST-estimated masses —and from the other papers in the ASPECS series—where the reliance is on MAGPHYS-estimated masses.

The middle panel of Figure 2 illustrates the effective range in stellar mass probed by our $z = 2$–10 sample. Most sources from our HUDF $z = 2$–10 sample have stellar masses in the range $10^{7.5} M_{\odot}$ to $10^{9.5} M_{\odot}$. The most massive sources probed by our program extend from 10^{10} to $10^{11.2} M_{\odot}$. Beyond the stellar mass itself, Figure 2 also illustrates the range in UV-continuum slope β probed by our samples (see Section 3.1 for details on how β is derived). Since the measured β has been demonstrated to be quite effective in estimating the infrared excess for lower-redshift UV-selected samples (e.g., M99; Reddy et al. 2006; Daddi et al. 2007), it is useful for us to probe a broad range in β. As can be seen from Figure 2, our samples probe the range $\beta \sim -1.5$ to ~ -2.5 quite effectively.

3. RESULTS

3.1. Expected Detections in the Far-IR Continuum

3.1.1. Expectations Using the $z \sim 0$ IRX–β Relations

We commence our analysis of our ALMA HUDF observations by first asking ourselves which sources we might expect to detect, given various results at lower redshift. Such an exercise will help us to interpret the results that follow and also to evaluate whether or not the number of sources we detect and the rest-frame far-IR flux density we measure for $z > 2$ galaxies are similar to those found for galaxies at $z \sim 0$.

We adopt as our $z \sim 0$ baseline the now canonical IRX–β relationship of M99, where a connection was found between the infrared excess (IRX) of galaxies and the spectral slope of
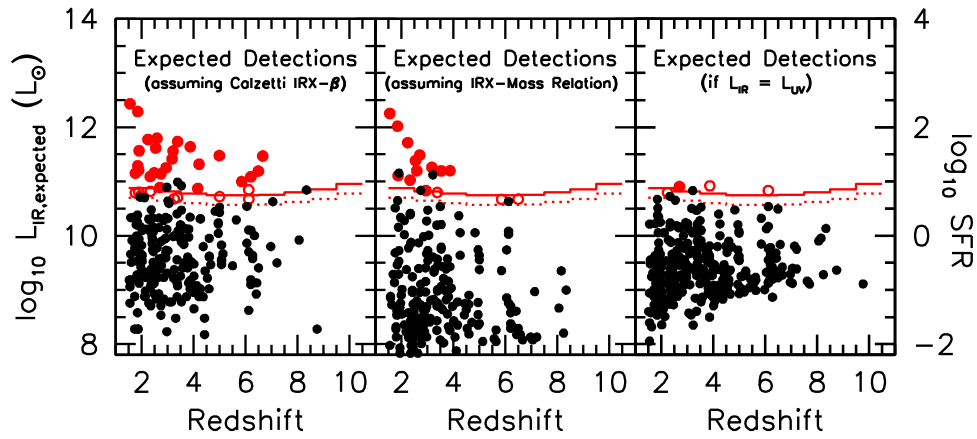
Figure 3. Expected IR luminosities (in $L_\odot$) vs. photometric redshift of $z = 2$–10 galaxies (solid circles) within the 1 arcmin^2 ASPECS region. Expected IR luminosities are based on (1) the M99 IRX–β relationship (*left panel*), (2) the approximate $z \sim 2$–3 IRX–stellar mass relationship (*center panel*: see Appendix A), or (3) assuming $L_{IR} = L_{UV}$ (*right panel*). The solid and dotted red lines indicate the 3σ and 2σ limiting luminosities, respectively, to which we can probe as a function of redshift in the deepest regions within our 1 arcmin^2 field (assuming that the SED is well represented by a 35 K modified blackbody). The solid and open red circles correspond to sources where 3σ and 2σ detections are expected, respectively, adopting the assumptions from a given panel, while the black circles indicate sources where a tentative 2σ detection is not expected. Black sources can appear above the red lines if these sources fall in regions of ASPECS where the sensitivities are lower than the maximum.

the UV continuum:

$$M99:\ IRX_{M99} = 1.75(10^{0.4(1.99(\beta+2.23))} - 1) \quad (1)$$

The factor of 1.75 in the above relationship is needed to express the M99 relation in terms of the IR luminosity, rather than the far-IR luminosity utilized by M99. See the discussion in Section 5.1 of Reddy et al. (2006). This relationship implicitly includes the slope of the dust law of Calzetti et al. (2000). Despite modest scatter (~ 0.3 dex), redder galaxies were systematically found to show higher infrared excesses than blue galaxies. For simplicity, the factor $B = BC(1600)_*/BC(FIR)$ from M99 is taken to equal one, consistent with the measurements made in that study.

Importantly, the M99 IRX–β relationship was shown to have a basic utility that went beyond the $z \sim 0$ universe for UV-selected samples. A series of intermediate-redshift studies (Reddy et al. 2006, 2010; Daddi et al. 2007; Pannella et al. 2009) found this relationship to be approximately valid when comparing the observed IR luminosities of galaxies to the predictions from the M99 IRX–β relationship.

As an alternative baseline, we also consider the expectations when adopting the so-called SMC IRX–β relationship, where a connection is again assumed between the infrared excess of a galaxy and its spectral slope in the UV continuum. However, since the SMC dust curve is steeper in the near-UV than dust laws like that of Calzetti et al. (2000), a small optical depth in dust extinction can have a large impact on the observed color of a galaxy in the UV continuum. The infrared excess, given an SMC extinction, can be expressed as follows:

$$SMC:\ IRX_{SMC} = 10^{0.4(1.1(\beta+2.23))} - 1 \quad (2)$$

This relationship is derived based on the observational results of Lequeux et al. (1982), Prevot et al. (1984), and Bouchet et al. (1985: see also Pei 1992; Pettini et al. 1998; Smit et al. 2015).

For each of the $z = 2$–10 sources in our ALMA field, we fit the *HST* photometry in various bands probing the UV continuum to a power law $f_{1600}(\lambda/1600\ \text{Å})^\beta$ to derive a mean flux at ~ 1600 Å and also a spectral slope β. We derive a

nominal luminosity for the source in the rest-frame UV by multiplying the flux density of the source at 1600 Å by the frequency at that wavelength ($\nu_{1600} f_{1600}$) and convert that to an expected IR luminosity for the source (considered to extend from 8 μm to 1000 μm).[25]

The equivalent flux at an observed wavelength of 1.2 mm is then computed by adopting a modified blackbody form with a dust temperature of 35 K and a power-law spectral index for the dust emissivity of $\beta_d = 1.6$. A value of $T_d = 35$ K is intermediate between the temperatures found for main-sequence galaxies by Elbaz et al. (2011) and Genzel et al. (2015), i.e., ~ 30 K at $z \sim 2$, and ~ 37–38 K found for stacked sources in other studies (Coppin et al. 2015).

Since the flux density we would measure with ALMA is reduced somewhat by the effective temperature of the CMB at $z \sim 2$–10, we multiply the measured flux by C_ν,

$$C_\nu = 1 - \frac{B_\nu(T_{CMB}(z))}{B_\nu(35\ \text{K})}, \quad (3)$$

to compute the expected signal. This treatment follows prescriptions given in da Cunha et al. (2013b).

Performing this exercise over all 330 $z = 2$–10 galaxies with coverage from our ALMA mosaic, we calculated expected fluxes for these sources at 1.2 mm assuming that sources follow the M99 and SMC IRX–β relations. These calculations suggested that 35 and 26 of these galaxies should be detected at $\geqslant 2\sigma$ and $\geqslant 3\sigma$ significance, respectively, in our observations if the M99 IRX–β relation applied, while eight and five of these sources would be detected at $\geqslant 2\sigma$ and $\geqslant 3\sigma$ significance, respectively, if the SMC IRX–β relationship applied to $z = 2$–10 galaxies in our samples.

To illustrate these expectations for our $z \geqslant 2$ study, we present the predicted IR luminosities for our $z \sim 2$–10 sample versus redshift in the left panel of Figure 3. The red solid and

---

[25] In performing these fits, we fix this slope to -2.2 for our two $z = 9$–10 candidate galaxies, given the lack of sufficiently deep long-wavelength data to constrain the UV-continuum slopes β. The β value we utilize here is motivated by the results of Bouwens et al. (2012, 2014b), Finkelstein et al. (2012), Kurczynski et al. (2014), and Wilkins et al. (2016a), who find evidence for bluer slopes for higher-redshift and generally fainter, lower-mass galaxies.

Table 3
$z \gtrsim 2$ UV-Selected Sources Expected to Show Tentative 2σ Detections Adopting the M99 IRX–β Relationship and Assuming a 35 K Modified Blackbody SED and $\beta_d = 1.6$

ID[a]	R.A.	Decl.	$m_{UV,0}$ (mag)	z_{ph}	$\log_{10}(M/M_\odot)$	β[b]	Predicted $f_{1.2mm}$ ([μJy]) Calz.[c]	SMC[e]	Mass[c,d]	Measured $f_{1.2mm}$ (μJy)	Inferred $L_{IR}/(10^{10} L_\odot)$
notice											

ID[a]	R.A.	Decl.	$m_{UV,0}$ (mag)	z_{ph}	$\log_{10}(M/M_\odot)$	β[b]	Calz.[c]	SMC[e]	Mass[c,d]	$f_{1.2mm}$ (μJy)	$L_{IR}/(10^{10} L_\odot)$
z ~ 2–3 Sample											
XDFU-2397246112(C2)	03:32:39.72	−27:46:11.2	24.4	1.55[e]	11.21	0.3 ± 0.1	1426	99	946[f]	261 ± 25	50 ± 5
XDFU-2373546453(C5)	03:32:37.35	−27:46:45.3	23.7	1.85[e]	10.52	−0.5 ± 0.1	1028	121	552[f]	71 ± 14	14 ± 3
XDFU-2393346236	03:32:39.33	−27:46:23.6	25.5	2.59[e]	10.18	−0.5 ± 0.1	369	44	93[f]	−12 ± 13	−2 ± 2
XDFU-2370746171	03:32:37.07	−27:46:17.1	23.7	2.24[e]	10.09	−1.2 ± 0.1	350	67	306[f]	34 ± 14	6 ± 2
XDFU-2358146436	03:32:35.81	−27:46:43.6	24.6	1.90[e]	9.98	−0.9 ± 0.1	194	31	75	16 ± 52	3 ± 10
XDFU-2356746283	03:32:35.67	−27:46:28.3	25.2	3.17	9.93	−1.3 ± 0.1	153	30	108[f]	−13 ± 21	−2 ± 4
XDFU-2385446340(C1)	03:32:38.54	−27:46:34.0	24.3	2.54[e]	9.9	−1.2 ± 0.1	242	47	143[f]	571 ± 14	97 ± 2
XDFU-2388246143	03:32:38.82	−27:46:14.3	26.3	3.38	9.85	−0.5 ± 0.1	321	38	37[f]	10 ± 14	2 ± 2
XDFU-2387446541	03:32:38.74	−27:46:54.1	25.7	2.74	9.85	−1.2 ± 0.1	81	15	40	18 ± 26	3 ± 4
XDFU-2365446123	03:32:36.54	−27:46:12.3	24.1	1.87[e]	9.77	−1.5 ± 0.1	85	19	68[f]	38 ± 16	7 ± 3
XDFU-2384246348	03:32:38.42	−27:46:34.8	23.8	2.70	9.75	−2.0 ± 0.1	46	13	181[f]	36 ± 14	6 ± 2
XDFU-2369146023	03:32:36.91	−27:46:02.3	24.1	2.33[e]	9.47	−1.8 ± 0.1	65	17	56[f]	13 ± 16	3 ± 3
XDFU-2395845544	03:32:39.58	−27:45:54.4	24.4	3.21[e]	9.46	−1.5 ± 0.1	215	47	78	14 ± 64	2 ± 11
XDFU-2369146348	03:32:36.91	−27:46:34.8	24.7	1.76	9.46	−1.3 ± 0.1	75	15	17	9 ± 14	2 ± 3
XDFU-2370846470	03:32:37.08	−27:46:47.0	24.4	1.85[e]	9.44	−1.3 ± 0.1	102	20	23	0 ± 15	0 ± 3
XDFU-2363346155	03:32:36.33	−27:46:15.5	25.3	2.34	9.32	−1.6 ± 0.1	35	8	13	1 ± 16	0 ± 3
XDFU-2366846484	03:32:36.68	−27:46:48.4	25.3	1.88[e]	9.27	−1.0 ± 0.1	84	14	8	−10 ± 19	−2 ± 4
XDFU-2366946210	03:32:36.69	−27:46:21.0	24.9	1.96	9.26	−1.7 ± 0.1	28	7	11	2 ± 13	0 ± 3
XDFU-2382946284	03:32:38.29	−27:46:28.4	26.2	1.76	9.22	−1.0 ± 0.1	32	5	3	−2 ± 14	−0 ± 3
XDFU-2378846451	03:32:37.88	−27:46:45.1	26.4	1.89	8.9	−0.9 ± 0.1	37	6	1	3 ± 15	0 ± 3
XDFU-2372446294	03:32:37.24	−27:46:29.4	27.2	3.25	8.77	−1.2 ± 0.1	28	5	1	−34 ± 14	−6 ± 2
XDFU-2379146261	03:32:37.91	−27:46:26.1	27.1	2.48	8.41	−0.4 ± 0.1	85	10	0	0 ± 13	0 ± 2
XDFU-2379046328	03:32:37.90	−27:46:32.8	26.8	3.38	8.25	−1.4 ± 0.1	30	6	1	−3 ± 14	−1 ± 2
z ~ 4 Sample											
XDFB-2394046224	03:32:39.40	−27:46:22.4	25.5	2.94[g]	9.76	−1.2 ± 0.1	119	22	45[f]	−22 ± 13	−3 ± 2
XDFB-2368245580	03:32:36.82	−27:45:58.0	24.4	3.87[e]	9.45	−1.5 ± 0.1	291	64	105[f]	−6 ± 22	−1 ± 3
XDFB-2375446199	03:32:37.54	−27:46:19.9	25.9	4.21	9.14	−1.3 ± 0.1	139	27	16	4 ± 14	1 ± 2
XDFB-2394246267	03:32:39.42	−27:46:26.7	27.1	4.99	8.73	−0.7 ± 0.2	200	28	3	−8 ± 13	−1 ± 2
XDFB-2381646267[h]	03:32:38.16	−27:46:26.7	28.5	4.16	8.57	−0.6 ± 0.4	50	7	0	−21 ± 13	−3 ± 2
z ~ 5 Sample											
XDFV-2372946175	03:32:37.29	−27:46:17.5	28.1	5.00	8.92	−1.1 ± 0.3	38	7	2	−1 ± 14	−0 ± 2
z ~ 6 Sample											
GSDI-2374046045	03:32:37.40	−27:46:04.5	26.7	5.85	9.52	−1.5 ± 0.8	71	16	34[f]	4 ± 14	1 ± 2
XDFI-2374646327	03:32:37.46	−27:46:32.7	26.4	6.49	9.35	−1.5 ± 0.2	111	25	34[f]	12 ± 14	2 ± 2
XDFI-2364964171	03:32:36.49	−27:46:41.71	25.5	6.12	8.97	−2.0 ± 0.2	50	14	31	−11 ± 18	−2 ± 2

Table 3
(Continued)

ID[a]	R.A.	Decl.	$m_{UV,0}$ (mag)	z_{ph}	$\log_{10}(M/M_\odot)$	β[b]	Predicted $f_{1.2mm}$ ([μJy]) Calz.[c]	SMC[c]	Mass[c,d]	Measured $f_{1.2mm}$ (μJy)	Inferred $L_{IR}/(10^{10} L_\odot)$
GSDI-2382846172	03:32:38.28	−27:46:17.2	26.2	6.12	8.66	−1.9 ± 0.3	34	9	8	−4 ± 14	−1 ± 2
XDFI-2378346180[h]	03:32:37.83	−27:46:18.0	29.3	6.20	8.54	−0.3 ± 0.6	87	9	0	1 ± 14	0 ± 2
					$z \sim 7$ Sample						
XDFZ-2381446048[h]	03:32:38.14	−27:46:04.8	29.5	6.66	7.98	0.2 ± 1.7	196	14	0	−11 ± 15	−2 ± 2

Notes.

[a] Source ID from Bouwens et al. (2015a). Otherwise selected from either a new catalog constructed here or the catalog of Rafelski et al. (2015) based on the *HST* WFC3/UVIS, ACS, and WFC3/IR observations over the HUDF. C1, C2, and C5 correspond to the continuum detections identified in our blind search of our ALMA 1.2 mm observations (Paper II from this series: Aravena et al. 2016a).

[b] UV-continuum slope β estimated by fitting the UV-continuum fluxes to a power law (Bouwens et al. 2012; Castellano et al. 2012; Rogers et al. 2013).

[c] Assuming a standard modified blackbody SED with dust temperature of 35 K and accounting for the impact of the CMB on the measured flux (da Cunha et al. 2013b).

[d] Assuming the consensus $z \sim 2$–3 relationship between the infrared excess and the inferred stellar mass of the galaxy (Appendix A).

[e] Spectroscopic redshift from 3D-*HST* (Momcheva et al. 2015).

[f] Tentative $\gtrsim 2\sigma$ detection of the source is expected.

[g] The B_{435}-dropout color selection criterion from Bouwens et al. (2015a) identifies galaxies with photometric redshifts as low as $z \sim 3$. We retain this source in our $z \sim 4$ sample, consistent with the B_{435}-dropout selection function of Bouwens et al. (2015a).

[h] These sources are nominally expected to be detected in our ALMA mosaic based on their very red measured β's. However, the β measurements for these sources are quite uncertain. It is anticipated that a few of the reddest $z = 6$–8 galaxies over our small field would have these colors due to the impact of noise.

9

open circles indicate those sources for which a 3σ and 2σ detection, respectively, is expected in our 1.2 mm continuum observations, while the solid black circles indicate those sources for which a detection is not expected. The solid and dotted red lines indicate the lowest IR luminosities at which we would detect sources at 3σ and 2σ, respectively, over the $\sim$1 arcmin^2 ASPECS region.

To help guide the discussion that follows, we provide a complete list of the sources with expected detections in Table 3. Comparisons of the actual flux measurements with estimates based upon various $z \sim 0$ IRX–β relations provide us with a quantitative sense of how much these relations have evolved from $z \geqslant 3$, while also illustrating the source-to-source scatter.

M99 found that individual sources exhibited a 0.3 dex scatter in L_{FIR} around the IRX–β relationship preferred in that study. If we include a similar scatter in predicting L_{IR} for individual sources, we predict 36.9 2σ and 28.4 3σ detections instead of 35 and 26, respectively.

The UV-continuum slopes β we use in setting these expectations are not known precisely, especially for the faintest sources in our $z = 6$–8 samples. In particular, if a source is measured to have an especially red β due to the impact of noise, we would predict its detection in the ASPECS data even if this source is actually intrinsically blue. The impact of the scatter is asymmetric since faint blue sources—with β's in the range of $\sim$−2 to $\sim$−2.3 (e.g., Wilkins et al. 2011; Dunlop et al. 2013; Kurczynski et al. 2014)—are already predicted to show essentially no dust emission and so the expected emission can only be larger when adding noise to the photometry of faint sources.

To determine the impact that this would have on the expected number of detected sources, we perturbed the measured β's for individual sources by the estimated uncertainty, and we calculated the total number of sources we would expect to find. Repeating this exercise multiple times, we found that this would boost the expected number of detections by $\sim$3.8 sources to 38.8 in total. This simulation result suggests that noise in the *HST* photometry does boost the expected numbers above what they would be in the noise-free case (by $\sim$11%). If we suppose that a similar correction applies to our nominal expectations for tentative detections (35 sources), $\sim$31.6 may be a better estimate for the expected number of tentative detections of $z \sim 2$–10 galaxies in ASPECS.

3.1.2. Expectations Using the $z \sim 2$ IRX–Stellar Mass Relation and Assuming $L_{IR} = L_{UV}$

Alternatively, we can (1) use the inferred stellar masses of $z \sim 2$–10 galaxies to estimate their IR luminosities or (2) assume that the IR luminosities of galaxies match their luminosities in the rest-frame UV. Previous work at $z \sim 0$–3 (e.g., Pannella et al. 2009) has demonstrated that the infrared excess of galaxies exhibits a strong correlation with the stellar mass, and many different authors (Reddy et al. 2010; Whitaker et al. 2014; Pannella et al. 2015) recover approximately the same relationship over a wide range in redshift, i.e., $z \sim 0$–3.

As an alternative demonstration of the utility of our ALMA observations, we show in the center and right panels of Figure 3 the expected detections in our data (*red solid circles*) if we assume that the luminosities of sources in the IR are either (1) dictated by the observed relationship between IRX and stellar mass at $z \sim 2$ or (2) equal to their luminosity in the rest-frame UV, respectively. We adopt the IRX–stellar mass relation presented in Figure 18 from Appendix A, which shows the approximate consensus relationship at $z \sim 2$–3 from three separate studies (Reddy et al. 2010; Whitaker et al. 2014; Álvarez-Márquez et al. 2016).

Fifteen and four tentative $>2\sigma$ detections are expected, respectively, for those two cases.

3.1.3. Impact of the Dust Temperature

We consider the impact that the assumed dust temperature has on these results. If, for example, the mean dust temperature were equal to 30 K as found by Elbaz et al. (2011), the expected number of detections would increase quite significantly. The totals would be 40 and 13 if we adopt the M99 IRX–β and SMC IRX–β relationships, respectively, while 20 detections would be expected based on the consensus $z \sim 2$–3 IRX–stellar mass relation.

Perhaps, even more importantly, we should consider the possibility that the dust temperature may increase quite substantially as we move out to higher redshift. A variety of work (e.g., Magdis et al. 2012; Béthermin et al. 2015) has found considerable evidence for such an evolution in the typical dust temperature from $z \sim 1.5$ to $z \sim 4$, in terms of the mean intensity in the radiation field $\langle U \rangle$, which is found to evolve as $(1 + z)^{1.8 \pm 0.4}$. As $\langle U \rangle \propto T^{4+\beta}$, the temperature can be inferred to evolve as $(1 + z)^{(1.8 \pm 0.4)/(4+\beta)} \sim (1 + z)^{0.32}$, such that for a mean dust temperature of 35 K at $z \sim 1.5$, the implied dust temperatures at $z \sim 4$ and $z \sim 6$ are equal to 44 K and 49 K, respectively. Such temperatures are very similar to the 40 ± 2 K found for a massive sample of $z \sim 4$ galaxies by Schreiber et al. (2016) and the 40–50 K found by Sklias et al. (2014) for typical $z \sim 2$–3 sources from the Herschel Lens Survey (Egami et al. 2010). We remark that one might naturally expect an evolution in dust temperature given the observed evolution in the SFR surface densities observed in galaxies with cosmic time (e.g., Shibuya et al. 2015) and the correlation of dust temperature with SFR surface density (e.g., Elbaz et al. 2011).

Assuming that the dust temperatures increase monotonically toward high redshift, as $(35\ K)((1 + z)/2.5)^{0.32}$, we predict that we should tentatively detect 20 sources using the M99 IRX–β relationship, three sources using the SMC IRX–β relationship, 11 sources using the consensus $z \sim 2$–3 IRX–stellar mass relationship, and zero sources assuming $L_{IR} = L_{UV}$.

3.2. Continuum Detections of Individual Sources at 1.2 mm

Here we look for possible individual detections of $z = 2$–10 galaxies over our deep ALMA continuum map at 1.2 mm. As results from the previous section illustrate, we could reasonably expect the number of detections to be modest if various IRX–β relations from the $z \sim 0$ universe serve as a useful guide.

Table 4 provides a summary of the properties of the $z \gtrsim 2$ sources from our catalog of 330 $z = 2$–10 sources that are nominally tentatively detected at $\gtrsim 2\sigma$ in our data. The measured flux density for the detected sources was derived by taking the value in our 1.2 mm continuum image at the nominal optical position of each source in our LBG samples (after correcting for the $0\rlap{.}''3$ positional offset between the ALMA and optical maps). We verified that we would retain all of our most significantly detected sources from this table if we

Table 4
$z \gtrsim 2$ UV-Selected Galaxies Showing Tentative 2σ Detections in Our Deep ALMA Continuum Observations[a]

ID	R.A.	Decl.	$m_{UV,0}$ (mag)	z_{ph}	$\log_{10}(M/M_\odot)$	β	Predicted $f_{1.2mm}$ (μJy) Calz.	SMC	Mass	Measured $f_{1.2mm}$ (μJy)	Inferred $L_{IR}/(10^{10} L_\odot)$
					Tentative $>2\sigma$ Detections (Most Credible)[b]						
XDFU-2397246112(C2)	03:32:39.72	−27:46:11.2	24.4	1.55[c]	11.21	0.3 ± 0.1	1426	99	946	261 ± 25	50 ± 5
XDFU-2373546453(C5)	03:32:37.35	−27:46:45.3	23.7	1.85[c]	10.52	-0.5 ± 0.1	1028	121	552	71 ± 14	14 ± 3
XDFU-2370746171	03:32:37.07	−27:46:17.1	23.7	2.24[c]	10.09	-1.2 ± 0.1	350	67	306	34 ± 14	6 ± 2
XDFU-2385446340(C1)	03:32:38.54	−27:46:34.0	24.3	2.54[c]	9.90	-1.2 ± 0.1	242	47	143	571 ± 14	97 ± 2
XDFU-2365446123	03:32:36.54	−27:46:12.3	24.1	1.87[c]	9.77	-1.5 ± 0.1	85	19	68	38 ± 16	7 ± 3
XDFU-2384246348	03:32:38.42	−27:46:34.8	23.8	2.70	9.75	-2.0 ± 0.1	46	13	181	36 ± 14	6 ± 2
					Not Especially Credible $>2\sigma$ Detections[d]						
XDFU-2403146258	03:32:40.31	−27:46:25.8	27.6	1.55	8.21	-1.9 ± 0.1	1	0	0	54 ± 26	10 ± 5
XDFB-2355846304	03:32:35.58	−27:46:30.4	29.9	4.06	8.15	-1.9 ± 1.0	1	0	0	71 ± 26	11 ± 4
					$>2\sigma$ "Detections" in the Negative Continuum Image						
XDFU-2372446294	03:32:37.24	−27:46:29.4	27.2	3.25	8.77	-1.2 ± 0.1	28	5	1	-34 ± 14	-6 ± 2
XDFU-2390646560	03:32:39.06	−27:46:56.0	26.7	2.42	8.75	-1.5 ± 0.1	12	3	1	-82 ± 38	-14 ± 7
XDFU-2390446358	03:32:39.04	−27:46:35.8	28.1	3.25	8.62	-2.0 ± 0.2	1	0	0	-33 ± 14	-6 ± 2
XDFU-2375346041	03:32:37.53	−27:46:04.1	26.4	1.96	8.26	-2.1 ± 0.1	1	0	0	-32 ± 14	-6 ± 3
XDFU-2369446426	03:32:36.94	−27:46:42.6	28.6	1.60	8.08	-1.3 ± 0.2	2	0	0	-32 ± 14	-6 ± 3
XDFB-2401746314	03:32:40.17	−27:46:31.4	28.3	4.01	8.21	-2.0 ± 0.3	1	0	0	-56 ± 26	-8 ± 4
XDFV-2385645553	03:32:38.56	−27:45:55.3	29.8	5.07	6.99	-1.6 ± 0.9	3	1	0	-72 ± 26	-10 ± 4
XDFZ-2375446018	03:32:37.54	−27:46:01.8	29.3	7.05	7.85	-2.3 ± 1.5	0	0	0	-40 ± 16	-6 ± 2

Notes.
[a] Columns in this table are essentially identical to those in Table 3.
[b] The reality of each of these tentatively detected sources is supported by there not being any comparable detections of $>10^{9.75} M_\odot$ sources in the negative continuum images and each of these sources also showing a detection in the MIPS 24 μm observations (see Table 10 from Appendix B).
[c] Spectroscopic redshift from 3D-HST (Momcheva et al. 2015).
[d] While fewer low-mass ($<10^9 M_\odot$) galaxies are tentatively detected at $>2\sigma$ in the positive continuum image than in the negative continuum image, this appears not to be statistically significant. The use of spatially offset positions (by $0\farcs3$) to measure the flux in sources typically results in an essentially equal number of tentative $>2\sigma$ detections in the positive and negative continuum images.

derived flux densities for sources using other methods (e.g., by scaling the normalization of the primary beam to fit the pixels in a $3'' \times 3''$ aperture centered on a source).

Only two sources from the entire catalog are detected at $\gg 3\sigma$ significance. They are the $z = 2.54$ source XDFU-2385446340, where the detection significance is indeed very high, i.e., 41σ, with $f_{1.2\,mm} = 571 \pm 14 \mu$Jy, and the $z = 1.55$ source XDFU-2397246112, where the detection significance is 10σ, with $f_{1.2\,mm} = 261 \pm 25 \mu$Jy. In Paper IV in this series (Decarli et al. 2016), we discuss the far-IR SED and molecular gas properties of both sources in more detail. Based on its X-ray flux in the deep *Chandra* observations over the Chandra Deep Field South (Xue et al. 2011), the latter source (XDFU-2397246112) is known to host an X-ray active galactic nucleus (AGN).

Six other sources from our catalogs show convincing $>3.5\sigma$ or tentative $>2\sigma$ detections in our ASPECS data. However, two of these detections appear to be noise spikes. This can been seen by looking for similar $>2\sigma$ detections in the negative continuum image for sources with similar stellar masses (also presented in Table 4). For the sources with the highest masses (i.e., $>10^{9.75} M_\odot$), only four positive 2σ detections are found and no 2σ "detections" in the negative images. The positive detections correspond to XDFU-2373546453, XDFU-2370746171, XDFU-2365446123, and XDFU-2384246348 with 5.1σ, 2.6σ, 2.4σ, and 2.3σ detections, respectively. Given

that there are only 13 sources in our highest-mass sample and six of them show at least a tentative $>2.3\sigma$ detection in our ALMA observations (expected only 1% of the time assuming Gaussian noise), each of these detections is likely real.[26]

We remark that each of these four sources is also detected in the MIPS 24 μm observations at $\gtrsim 2\sigma$ significance, providing further support for our conclusions here (see Table 10 from Appendix B). This also points toward MIPS 24 μm data being a valuable probe of the infrared excess to $z \sim 3$, given its competitive sensitivity to long exposures with ALMA.

For sources with estimated stellar masses in the range 10^7 to $10^9 M_\odot$, tentative 2σ detections are seen in both the positive and negative images. The excess numbers in the negative image appear not to be statistically significant, because small changes to the positions where the flux measurements are made (by $\sim 0\farcs1$) typically result in essentially identical numbers of tentative 2σ detections in the positive and negative continuum images.

To illustrate the significance of this apparent dependence on the inferred stellar mass, we present in Figure 5 the fraction of

---

[26] Our conclusions here differ significantly from what we would conclude based on a blind search for $>2\sigma$ detected sources across the entire 1 arcmin^2 mosaic (where the fidelity is only 25% for sources with flux densities between 30 and 40 μJy: Paper II: Aravena et al. 2016a). With a blind search, one has many opportunities to find tentative $>2\sigma$-detected sources; however, for the present high-mass sample, one only has 13 opportunities.

HST	IRAC	1.2mm
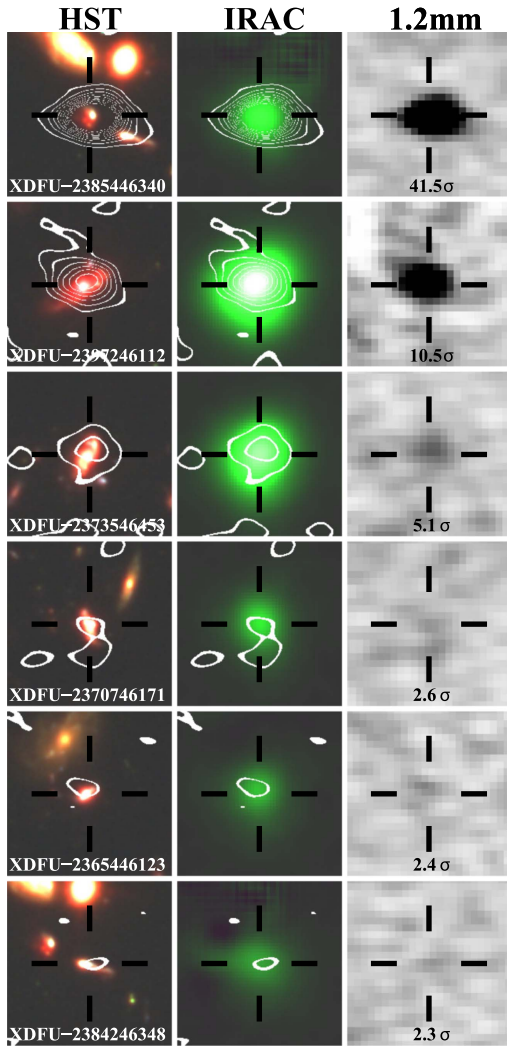
Figure 4. HST $B_{435}i_{775}H_{160}$ (*left*), IRAC 3.6 μm (*middle*), and 1.2 mm ALMA-continuum images (*right*) for six $z \sim 2$–3 galaxies that we detect ($>3.5\sigma$) or tentatively detect ($>2\sigma$) in our 1 arcmin^2 deep ALMA map over the HUDF. The size of the stamps is $7\rlap{.}''2 \times 7\rlap{.}''2$. The positions of our 1.2 mm continuum detections relative to the positions of sources in our HST or Spitzer/IRAC images are illustrated in the left and center stamps with the 2σ, 4σ, 6σ, 8σ, and 10σ contours (*white lines*). Light from neighboring sources on the IRAC images has been removed for clarity. Significantly enough, these sources are among the 13 $z = 2$–10 candidates from that 1 arcmin^2 region with the highest stellar mass estimates. All six have estimated stellar masses $\geqslant 10^{9.75}$ $M_\odot$. Given evidence that dust emission from star-forming galaxies correlates with stellar mass in many studies (e.g., Pannella et al. 2009, 2015; Reddy et al. 2010; Whitaker et al. 2014; Álvarez-Márquez et al. 2016), these sources are among the six sources most likely to show dust emission from our entire $z = 2$–10 LBG selection. The fact that each of them shows ALMA flux at $\geqslant 2.3\sigma$ seems to confirm that stellar mass is an especially useful predictor of dust emission for normal star-forming galaxies at $z \gtrsim 2$. Each of these sources also shows evidence for being detected ($\gtrsim 2\sigma$) in the MIPS 24 μm observations (Table 10 from Appendix B).

detected $z = 2$–10 galaxies versus mass, after correcting the positive $>2\sigma$ detections in a mass bin for the $>2\sigma$ detection seen in the negative image. For this figure, we consider only those sources (172 out of 330) over the ASPECS field for which the 1.2 mm continuum sensitivities are the highest, i.e., with 1σ rms noise <17 μJy. $63^{+14}_{-17}\%$ of the galaxies with stellar mass estimates $>10^{9.75}$ $M_\odot$ are detected; none of the sources with masses lower than $10^{9.75}$ $M_\odot$ is detected. Dust-continuum emission shows a clear connection with the apparent stellar
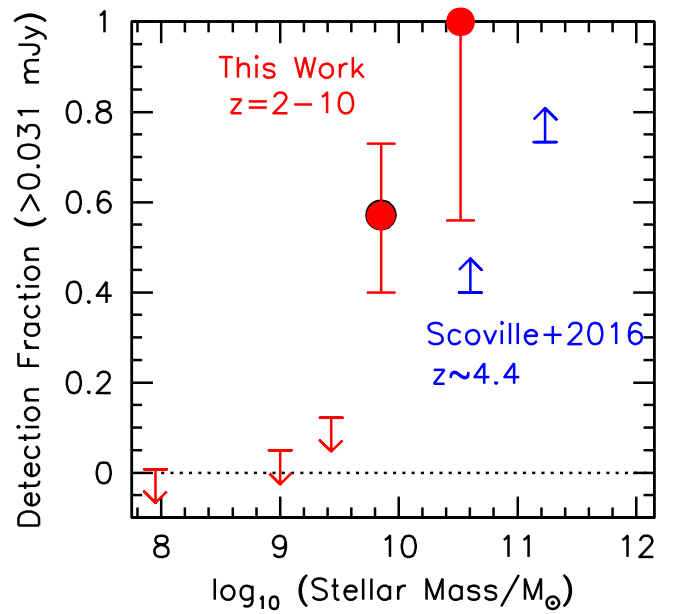

Figure 5. Fraction of tentatively detected ($>2\sigma$) $z = 2$–10 galaxies in our ALMA 1.2 mm continuum observations vs. the inferred stellar mass (*solid red circle*). Errors and upper limits are 1σ. Only the 172 $z = 2$–10 galaxies where our 2σ continuum sensitivity is highest (<34 μJy) are included in this determination. The blue upward-pointing arrows are from Scoville et al. (2016) and indicate lower limits on the detected fraction (i.e., at >0.031 mJy) based on the results of that study. Stellar mass appears to be a very good predictor of dust emission in $z = 2$–10 galaxies, with five of the eight $>10^{9.75}$ $M_\odot$ galaxies probed at the requisite sensitivity being detected at $>2\sigma$ (and several other $>10^{9.75}$ $M_\odot$ galaxies probed by our field show measured 1.2 mm fluxes consistent with the other measurements).

mass in galaxies—which is similar to a few prominent earlier predictions for the expected findings from a deep far-IR continuum survey over the HUDF with ALMA (da Cunha et al. 2013b).

As a separate illustration of the predictive power of stellar mass in estimating the approximate luminosity of galaxies in the IR, we present in Figure 6 the range in stellar mass versus redshift probed by our HUDF sample and indicate the sources we identify as detected in red (open and solid circles detected at $>3\sigma$ and 2σ–3σ, respectively) and those we identify as only found in a blind search in green (ASPECS Paper II: Aravena et al. 2016a). The sources we detected at $>3\sigma$ also appear in the blind search of Aravena et al. (2016a). It is clear that stellar mass is a good predictor of which sources are IR-luminous, for galaxies with $z > 1.5$. The stellar masses used for constructing Figure 6 are taken from the 3D-HST catalogs (Skelton et al. 2014) if at $z < 1.5$ (if available); otherwise, they are inferred as in Section 2.3. For the most obscured systems, estimates of the redshift and stellar mass can be quite uncertain (given degeneracies between dust and age and the challenge in locating spectral breaks), so some caution is needed in interpreting this figure.

We now return to discussing continuum-detected sources in ASPECS. 1.2 mm continuum images of the six sources showing meaningful detections are presented in Figure 4 together with their HST and Spitzer/IRAC images. We remark that the detected sources in the present samples are much fainter than those identified in many previous programs. For example, the typical flux measured by Scoville et al. (2016) for detected $z \sim 4.4$ galaxies in their very high-mass ($\gtrsim 2 \times 10^{10}$ $M_\odot$) sample is ~ 200 μJy, which contrasts with the ~ 35 μJy
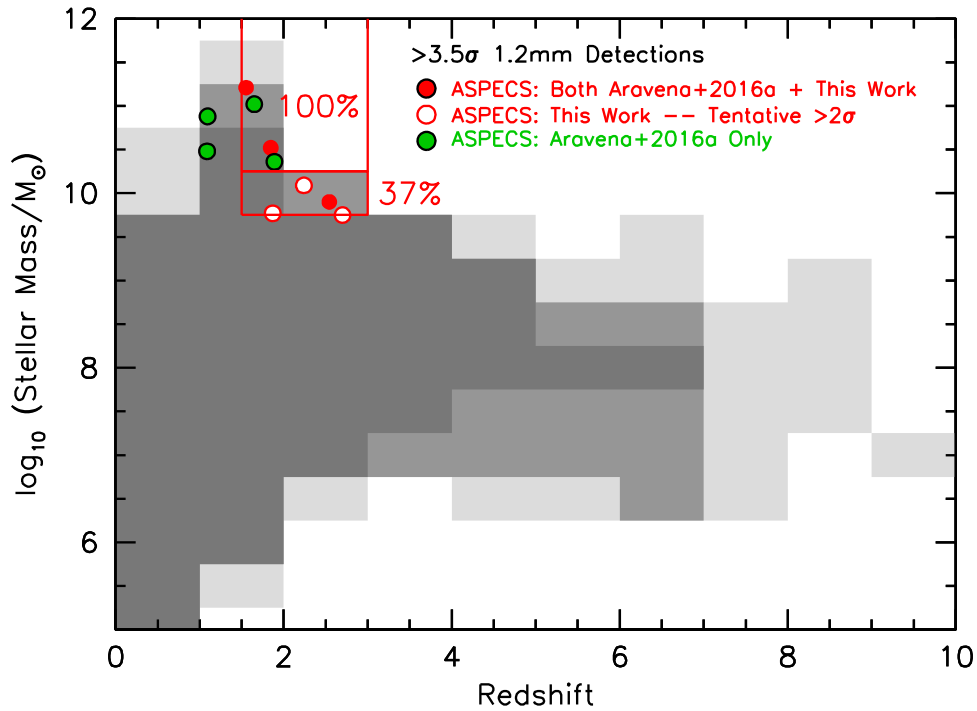
Figure 6. Stellar mass vs. redshift range covered by sources identified over the ~1 arcmin^2 ASPECS region, with light, medium dark, and dark gray indicating regions where ⩾1, ⩾3, and ⩾7 sources are found (where each region subtends $\Delta M \sim 0.5$ dex $\times \Delta z \sim 1$). Large filled red circles indicate those sources where continuum detections (>3.5σ) are found in both the present study and Paper II of the ASPECS series (Aravena et al. 2016a). Green circles indicate sources that are found only in Paper II of ASPECS (Aravena et al. 2016a). Open red circles indicate those galaxies that show tentative >2σ detections in ASPECS. 100% and 37% of the star-forming $z = 1.5$–3.0 sources in the stellar mass ranges $\log_{10}(M/M_\odot) > 10.25$ and 9.75–10.25 (indicated with the *red boxes*), respectively, show detections in the ALMA continuum 1.2 mm data. It is clear that stellar mass is an especially useful predictor of IR luminosity over a wide range in redshift. Inspiration for this figure came in part from Figure 6 of Dunlop et al. (2016).
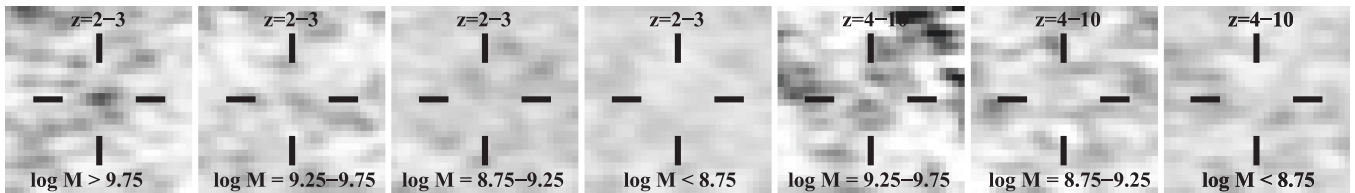
Figure 7. Stacked 1.2 mm continuum images (9″ × 9″) for all candidate $z = 2$–3 and $z = 4$–10 galaxies falling in four different ranges of stellar mass ($< 10^{8.75} M_\odot$, $10^{8.75}$ to $10^{9.25} M_\odot$, $10^{9.25}$ to $10^{9.75} M_\odot$, and $>10^{9.75} M_\odot$). In the stacks, sources are weighted according to the square of their UV flux and the inverse square of the noise. The three sources from this analysis individually detected at >4σ are not included in the stack results shown in this figure.

seen in the three faintest $z \sim 2$–3 galaxies tentatively detected here. The observed differences in the typical fluxes of detected sources are a natural consequence of the relative sensitivities of the data sets, i.e., 12.7 μJy beam^{-1} rms for ASPECS versus 65 μJy beam^{-1} rms in the observations of Scoville et al. (2016).

3.3. Stacked Constraints on the Infrared Excess

In addition to looking at which $z = 2$–10 galaxies over the HUDF we can individually detect in our ALMA continuum observations, we can gain powerful constraints on dust emission from high-redshift galaxies by stacking. For this, we subdivide our samples in terms of various physical properties and then make a weighted stack of the ALMA-continuum observations at the positions of the candidates.

For sources included in the stack, we map the ALMA continuum maps onto the same position and weight the contribution of each source to the stack according to its expected 1.2 mm continuum signal assuming $L_{IR} \propto L_{UV}$ and according to the inverse square of the noise (per beam). We

derive a flux from the stack based on a convolution of the image stack (3″3 × 3″3 aperture) with the primary beam. No spatial extent is assumed in the stacked flux.

3.3.1. IRX versus Stellar Mass

We begin by looking at the average inferred infrared excesses of $z = 2$–10 galaxies as a function of the stellar mass. Segregating our samples in terms of stellar mass certainly is a logical place to start. Not only is there strong support in the literature for such a correlation at lower redshifts (e.g., Pannella et al. 2009, 2015; Reddy et al. 2010), but there is evidence for this correlation being present in our own limited samples (see Section 3.2).

In Figure 7, we show the stacked 1.2 mm continuum observations of $z = 2$–3 and $z = 4$–10 galaxies in four different bins of stellar mass: $>10^{9.75} M_\odot$, $10^{9.25}$–$10^{9.75} M_\odot$, $10^{8.75}$–$10^{9.25} M_\odot$, and $<10^{8.75} M_\odot$. For these stacks, we weight sources according to the square of the expected signal in the
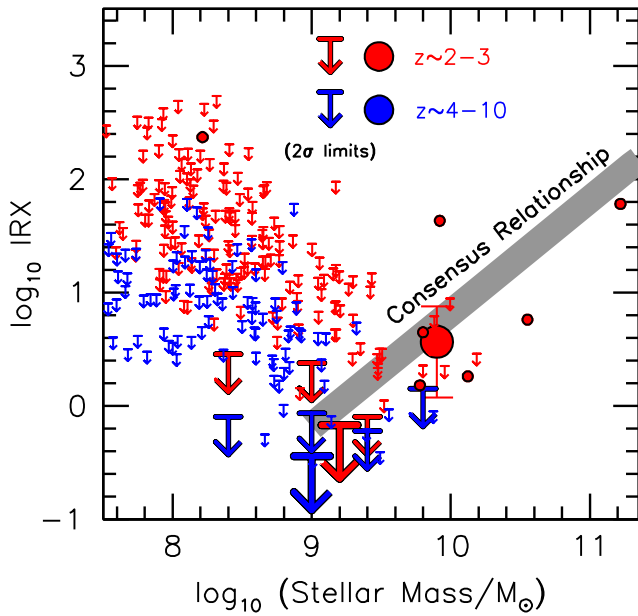
Figure 8. Constraints on the infrared excess of $z = 2$–3 and $z = 4$–10 galaxies (*large red and blue circles* and *downward arrows,* respectively) obtained by stacking the ALMA 1.2 mm observations available for many individual sources over the 1 arcmin^2 ASPECS region (excluding the one source XDFU-2397246112 with an AGN, but not excluding any other sources). The small filled circles and downward arrows are for sources with a positive 2σ measurement of IRX and 2σ upper limit on IRX, respectively. Upper limits and error bars are 2σ and 1σ, respectively. A redshift-independent dust temperature of 35 K is assumed in deriving these results. The presented upper limits on our $z = 4$–10 sample would be 0.4 dex higher if the dust temperature in higher-redshift galaxies were significantly higher than at $z \sim 1.5$ (i.e., 44–50 K as suggested by the results of Magdis et al. 2012 and Béthermin et al. 2015). The thick shaded gray line shows the consensus dependence of IRX on the galaxy stellar mass we derive for $z \sim 2$–3 galaxies (Appendix A) from the literature (Reddy et al. 2010; Whitaker et al. 2014; Álvarez-Márquez et al. 2016). The results of the ALMA stack suggest that only galaxies with stellar masses in excess of $\gtrsim 10^{9.75} M_\odot$ tend to output a significant ($\gg 50\%$) fraction of their energy at far-infrared wavelengths.

1.2 mm continuum observations (assuming $L_{IR} \propto L_{UV}$) and the inverse square of the noise (in μJy), i.e., $(L_{UV}/\sigma(f_{1.2\,mm}))^2$.[27]

The implied constraints on IRX as a function of stellar mass are presented in Figure 8, Table 5, and Table 12 from Appendix D for both our $z = 2$–3 and $z = 4$–10 samples. Significantly enough, the only mass bin where we find a detection is for $>10^{9.75} M_\odot$ galaxies at $z = 2$–3. This is not surprising since six of the 11 sources that compose this mass bin show at least tentative individual detections ($\gtrsim 2\sigma$) in our ALMA observations. All the other mass bins are consistent with the infrared excess showing an approximate 2σ upper limit of IRX ~ 0.4 for $<10^{9.75} M_\odot$ galaxies.

Making use of the collective constraints across our $z \sim 2$–10 sample, we find an approximate 2σ upper limit on the infrared excess of 0.4 for lower-mass ($<10^{9.75} M_\odot$) galaxies. This suggests that dust emission from faint UV-selected sources is typically small.

In our stacking experiments, we also compute a constraint on the flux at 1.2 mm relative to the flux in the UV continuum. For

---

[27] This weighting factor is just equal to the inverse square of the expected noise in a measurement of the infrared excess (noting that $L_{IR} \propto f_{1.2mm}$ and that the fractional uncertainty in L_{UV} is negligible relative to that in L_{IR} for all sources considered in this study). We remark that photometric redshift errors should also have an impact on the uncertainties in L_{IR}/L_{UV} and hence on the weighting, but such uncertainties are small, given that our stacks do not generally yield detections.

Table 5
Inferred IRX versus Galaxy Stellar Mass and β from ASPECS (assuming $T_d = 35$ K and $\beta_d = 1.6$)[a]

Stellar Mass	β	# of sources	IRX[b]
		$z = 2$–3	
$>10^{9.75} M_\odot$	All	11	$3.80^{+3.61}_{-2.40} \pm 0.19$
$<10^{9.75} M_\odot$	All	151	$0.11^{+0.32}_{-0.42} \pm 0.34$
		$z = 4$–10	
$>10^{9.75} M_\odot$	All	2	$-0.49^{+0.69}_{-1.13} \pm 0.71$
$<10^{9.75} M_\odot$	All	166	$0.14^{+0.15}_{-0.14} \pm 0.18$
		$z = 2$–3	
$>10^{9.75} M_\odot$	$-4 < \beta < -1.75$	1	$0.54^{+0.00}_{-0.00} \pm 0.29$
	$-1.75 < \beta < -1.25$	2	$1.31^{+0.67}_{-0.94} \pm 0.72$
	$\beta < -1.25$	8	$6.79^{+5.38}_{-4.51} \pm 0.26$
$<10^{9.75} M_\odot$	$-4 < \beta < -1.75$	89	$0.19^{+0.40}_{-0.76} \pm 0.44$
	$-1.75 < \beta < -1.25$	49	$-0.01^{+0.39}_{-0.35} \pm 0.58$
	$\beta < -1.25$	13	$-0.14^{+4.65}_{-3.64} \pm 2.11$
		$z = 4$–10	
$<10^{9.75} M_\odot$	$-4 < \beta < -1.75$	122	$0.03^{+0.22}_{-0.15} \pm 0.24$
	$-1.75 < \beta < -1.25$	29	$0.33^{+0.11}_{-0.16} \pm 0.29$
	$\beta < -1.25$	11	$-1.03^{+0.29}_{-1.23} \pm 1.46$

Notes.
[a] See Tables 12–14 from Appendix D for a more detailed presentation of the stack results summarized here.
[b] Both the bootstrap and formal uncertainties are quoted on the result (presented in that order).

these results, sources are weighted according to the square of their UV-continuum fluxes and inversely according to the noise in the ALMA 1.2 mm observations. Making use of all sources in our $z \sim 2$–3 and $z \sim 4$–10, $<10^{9.75} M_\odot$ samples, we find 2σ upper limits of 20 and 44, respectively, on the ratio of fluxes at 1.2 mm and in the UV continuum.

The impact of this result is illustrated in Figure 9, by comparing current constraints against several possible SED templates at $z \sim 2$–3 and $z \sim 4$–10. The result provides information on the overall shape of the spectral energy distribution that is independent of the assumed SED template.

3.3.2. IRX versus β

Next we subdivide our $z = 2$–10 samples in terms of their UV-continuum slopes. Given evidence that the infrared excess depends significantly on β at $z \sim 0$ (M99) and also at $z \sim 2$ (Reddy et al. 2006, 2010; Daddi et al. 2007; Pannella et al. 2009), we want to quantify this dependence in our own sample. We split our results by stellar mass (i.e., $<10^{9.75} M_\odot$ and $>10^{9.75} M_\odot$) motivated by the results of the previous section.

We examine the IRX–β relation for $z = 2$–3 sources with $>10^{9.75} M_\odot$ in Figure 10, Table 5, and Table 13 from Appendix D using three different bins in β. The only source from the present ASPECS sample that shows a prominent X-ray detection (XDFU-2397246112) is excluded. Stacks of the ALMA continuum images at the positions of the sources are provided in Figure 11, after excluding those sources detected at $>4\sigma$.

Given the small sample size, it is difficult to compute accurate uncertainties on the IRX–β relationship at $z \sim 2$–3, but the large red solid circles give our best estimates. The present constraints appear most consistent with an SMC IRX–β relationship.
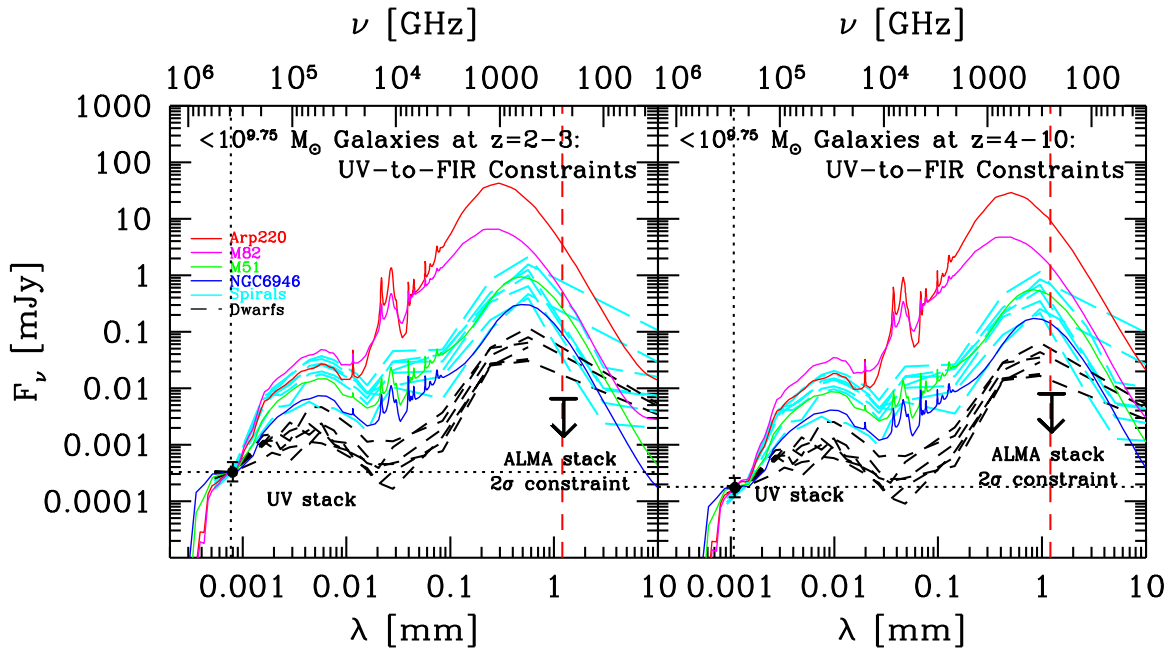
Figure 9. Illustration of the general constraints we can set on the overall shape of the near-UV + far-IR spectral energy distribution for lower-mass ($<10^{9.75} M_\odot$) galaxies at $z = 2$–3 (*left panel*) and $z = 4$–10 (*right panel*) based on the results we obtain by stacking our deep 1.2 mm ALMA HUDF observations at the positions of candidate $z = 2$–10 galaxies. The flux points at ∼0.8 and 1.1 μm show the UV fluxes for our lower-mass stack of $z = 2$–3 and $z = 4$–10 candidates, respectively, while the large upper limit shows the 2σ upper limit we can set on the flux at 1.2 mm (which is just a factor of 20 and 44 higher, respectively, than the weighted flux in the UV continuum that contributes to the stack results shown here: see Table 12 from Appendix D). For reference, we have included model SED templates from Silva et al. (1998), Dale et al. (2007), and some lower-metallicity galaxies studied in the KINGFISH project (Dale et al. 2012) redshifted to $z \sim 4$. Our ALMA observations suggest that faint, lower-mass high-redshift galaxies show less dust emission at 1.2 mm than any of these SED templates.

We formalize this analysis by calculating the region of the IRX–β plane preferred at 68% confidence. For this, we compare the derived IRX–β relationship with what would be predicted based on dust laws with various slopes $dA_{\mathrm{UV}}/d\beta$ (where IRX $= 10^{0.4(dA_{\mathrm{UV}}/d\beta)(\beta+2.23)} - 1$). The result we obtain for $dA_{\mathrm{UV}}/d\beta$ is $1.26^{+0.27}_{-0.36}$ ($1.26^{+0.49}_{-0.91}$ at 95% confidence) and is presented in Figure 10 as a light-red shaded region. It is most consistent with an SMC dust law (where $dA_{\mathrm{UV}}/d\beta \sim 1.1$).

We also quantify the IRX–β relationship for the lower-mass sources at $z = 2$–3 and present the stack results in Figure 10 as 2σ upper limits (*downward green arrows*) and also in Table 13 from Appendix D. The limits are much lower than the constraints we obtained for the highest-mass galaxies considered here and indicate that the IRX–β relationship depends on the stellar mass of the sources. As with our higher-mass sample, we use the stacked constraints to constrain the IRX–β relation (shown with the light-green shaded region in Figure 10), finding $dA_{\mathrm{UV}}/d\beta < 1.22$ at 95% confidence.

We also derive constraints on the IRX–β relationship for our $z = 4$–10 sample. This sample contains only two galaxies with stellar masses in excess of $10^{9.75} M_\odot$—neither of which is detected in our ALMA observations—so we do not consider a higher-mass subsample of galaxies. The image stamps showing the stack results are presented in Figure 11, while the infrared excess derived from these stack results is presented in Table 13 from Appendix D and in Figure 12. As in Figure 10, we determine the implications of these constraints for the IRX–β relationship and present the result in Figure 12 using a green-shaded contour. The 2σ upper limit we derive for $dA_{\mathrm{UV}}/d\beta$ is 0.87. Again, our derived constraints on $dA_{\mathrm{UV}}/d\beta$ suggest that dust emission from lower-mass $<10^{9.75} M_\odot$ galaxies is generally quite small.

Uncertainties in the measured UV-continuum slopes β also have an impact on these results, because scatter toward redder colors could cause us to include intrinsically blue sources in the reddest β bins. Since sources with the reddest colors are expected to have these colors due to dust extinction, these bins have significantly more leverage in determining the value that we derive for $dA_{\mathrm{UV}}/d\beta$. Noise has a particularly significant impact on the β's derived from the highest-redshift sources in our samples, i.e., particularly at $z = 7$–8.

To determine the impact of noise on the values we derive for $dA_{\mathrm{UV}}/d\beta$, we perturbed the best-estimate β values for individual sources by our uncertainty estimates on each β determination, rebinned the sources as for our fiducial results, and then rederived the $dA_{\mathrm{UV}}/d\beta$ for the perturbed data set. We repeated this process 10 times and we found that the 2σ upper limit on $dA_{\mathrm{UV}}/d\beta$ decreased on average by 0.1 for our low-mass, $z = 4$–10 sample, but did not have a noticeable impact on the $dA_{\mathrm{UV}}/d\beta$ value we derived for our $z = 2$–3 sample.

We therefore correct the 1σ upper limit we derive on $dA_{\mathrm{UV}}/d\beta$ by 0.0 and 0.1 for our low-mass $z = 2$–3 and $z = 4$–10 samples, respectively. This translates into 2σ upper limits on $dA_{\mathrm{UV}}/d\beta$ of 1.22 and 0.97 for our low-mass samples at $z = 2$–3 and $z = 4$–10, respectively. All of the present constraints on $dA_{\mathrm{UV}}/d\beta$ for sources at different redshifts and with different stellar masses are summarized in Table 6.

The conclusions here can be impacted by our assumed dust temperatures. If we assume monotonically higher dust temperatures at $z \geqslant 3$ such that $T_d \sim 44$–50 K at $z \sim 4$–6, then the 2σ upper limit on the IRX–β relation increases by 0.37 dex (shown as a *dotted line*), consistent with an SMC IRX–β relationship. Previously, Ouchi et al. (1999) had argued on the basis of SCUBA 850 μm observations over the Hubble Deep Field North (Hughes et al. 1998) that $z \gtrsim 3$ star-forming galaxies could be
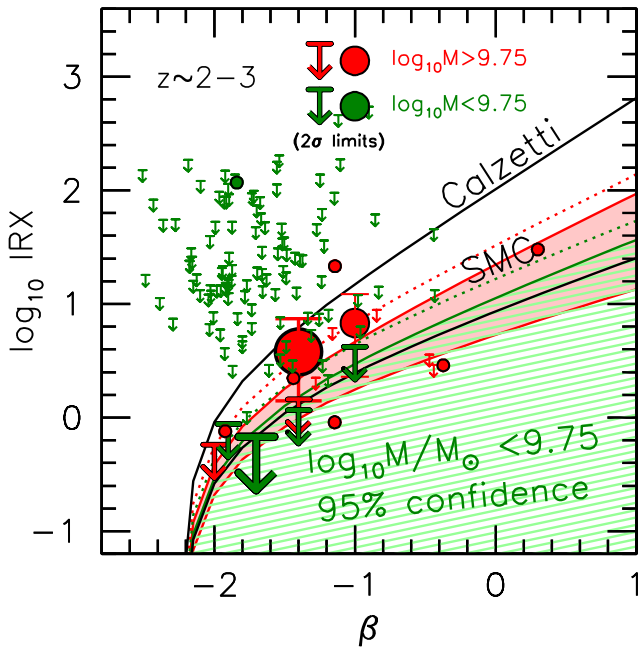
Figure 10. Stacked constraints on the infrared excess in $z = 2$–3 galaxies vs. the UV-continuum slope β. These results are shown for higher- and lower-mass subsamples ($>10^{9.75}$ $M_\odot$ and $<10^{9.75}$ $M_\odot$) of $z = 2$–3 galaxies (*red and green solid circles* and *downward arrows,* respectively) and were obtained by stacking the ALMA 1.2 mm observations of individual sources over the ASPECS region (excluding the one source XDFU-2397246112 with an AGN, but not excluding any other sources). Upper limits and error bars are 2σ and 1σ, respectively. The smaller solid circles and downward arrows indicate a $>2\sigma$ measurement of the infrared excess and 2σ upper limits on this excess. The purpose of the smaller points is to show the constraints that can be derived from individual sources before stacking. The very large red circle and downward-pointing green arrow give the value and 2σ upper limit, respectively, on IRX based on all $>10^{9.75}$ $M_\odot$ and $<10^{9.75}$ $M_\odot$ $z = 2$–3 sources from ASPECS plotted at the weighted value of β that contributes the most signal to this measurement of IRX. The solid lines show the nominal IRX–β relation that one would derive based on the Calzetti and SMC dust laws. The shaded red and light green regions indicate the 68% and 95% confidence intervals we can derive on the IRX–β relationship on the basis of our results for sources with stellar masses of $>10^{9.75}$ $M_\odot$ and $<10^{9.75}$ $M_\odot$, respectively. If the dust temperature increases toward high redshift as indicated by Béthermin et al. (2015), the upper bound on these regions would be given by the dotted red and green regions. Our results are consistent with the IR emission from high-mass ($>10^{9.75}$ $M_\odot$) $z \sim 2$–3 galaxies exhibiting an SMC IRX–β relation. However, for lower-mass ($<10^{9.75}$ $M_\odot$) galaxies, our results suggest lower infrared excesses, less even than expected for an SMC dust law.

consistent with the $z \sim 0$ M99 relation only if the dust temperature was $\gtrsim 40$ K.

The present results are not especially different from IRX versus β results found by Capak et al. (2015) for a small sample of $z \sim 5$–6 galaxies, where most of the sources in their sample lie below the SMC relation, but are clearly lower than the results of Coppin et al. (2015) where IRX was found to be ~ 8 for $z \sim 3$ sources with β's of ~ -2 to -1.5. The results of Coppin et al. (2015) were based on a deep stack of SCUBA-2 (Holland et al. 2013) Cosmology Legacy Survey data (Geach et al. 2013) over the UKIDSS-UDS field (Lawrence et al. 2007). The explanation for differences relative to the results of Coppin et al. (2015) is not entirely clear.[28]

---

[28] Given the broad SCUBA-2 beam, it is possible that the far-IR stacks that Coppin et al. (2015) create of the bluer sources include some flux from their bright neighbors. Also the stack results of Coppin et al. (2015) surely include more massive $z \sim 3$ galaxies than in the present narrow field probe, and since IRX is typically much larger for more massive galaxies at a given β (e.g., Reddy et al. 2006), this could contribute to the observed differences.

3.3.3. IRX versus Apparent Magnitude in the Rest-frame UV

Lastly, we look at the infrared excess as a function of the apparent magnitude of sources in the rest-frame UV. Knowing the dependence of the infrared excess on the apparent magnitude is valuable, given the relevance of this variable to source selection and also its close connection to the SFR (if dust obscuration is low).

Again we break up our samples into two different redshift bins, $z = 2$–3 and $z = 4$–10. We consider a bright sample, $m_{UV,AB} < 25$ ($z = 2$–3) and $m_{UV,AB} < 26$ ($z = 4$–10), and a faint sample, $m_{UV,AB} > 25$ ($z = 2$–3) and $m_{UV,AB} > 26$ ($z = 4$–10). As with our other stack results, we weight the signal from individual sources to maximize the signal in our measurement of the infrared excess. Our stack results for the different bins in apparent magnitude are presented in Table 14 from Appendix D.

Only the brightest ($H_{160,AB} < 25$) $z = 2$–3 galaxies show a detection in our stack results. This is consistent with IRX being positively correlated with the SFR observed in the rest-frame UV for galaxies. There has been substantial discussion in previous work (e.g., Reddy et al. 2006) regarding a general correlation of IRX with the SFR, though this correlation appears to show strong evolution as a function of redshift (Reddy et al. 2010; Domínguez et al. 2013) such that $z \sim 2$–3 galaxies show much less extinction at a given SFR than at $z \sim 0$.

### 3.4. Sensitivity of Results to the Dust Temperature

Essentially nothing is known about the typical dust temperature for sub-L^* star-forming galaxies at $z \sim 2$–10. While many star-forming galaxies have measured dust temperatures of ~ 25–30 K (Elbaz et al. 2011; Magnelli et al. 2014; Genzel et al. 2015), there are many faint, individually detected sources that have much higher dust temperatures (Sklias et al. 2014), i.e., ~ 40–50 K. Moreover, the dust temperature is known to depend on its specific SFR relative to that median value on the main sequence, taking values of ~ 20 K, ~ 30 K, or ~ 40 K depending on whether a galaxy is below, on, or above the main sequence, respectively (Elbaz et al. 2011; Genzel et al. 2015).

Uncertainties in the dust temperature of lower-mass, $z \geqslant 2$ galaxies are important since the results we derive depend significantly on the form of the far-IR SED we assume. To illustrate, if we assume that the dust temperatures are lower than 35 K, it would imply lower IR luminosities (and stronger upper limits on the luminosities). On the other hand, if we assume that the dust temperature of sub-L^* galaxies at $z \sim 2$–10 is higher than 35 K, it would imply higher IR luminosities (and weaker upper limits on the IR luminosity) for $z \geqslant 2$ sources probed by the ASPECS program. The latter possibility would appear to be a particularly relevant one to consider in light of recent results from Magdis et al. (2012) and Béthermin et al. (2015), which have suggested that the mean intensity in the radiation field (and hence the typical dust temperature) of galaxies with moderate to high masses increases substantially toward higher redshifts, i.e., as $(1 + z)^{0.32}$ (Section 3.1.3), and therefore T_d is in the range 44–50 K at $z = 4$–10.

For convenience, we provide a table in Appendix C that indicates how the derived luminosities would change depending on the SED template or dust temperature assumed. Included in this table are dust temperatures ranging from 25 K to 45 K and also empirical SED templates for M51, M82, Arp 220, and
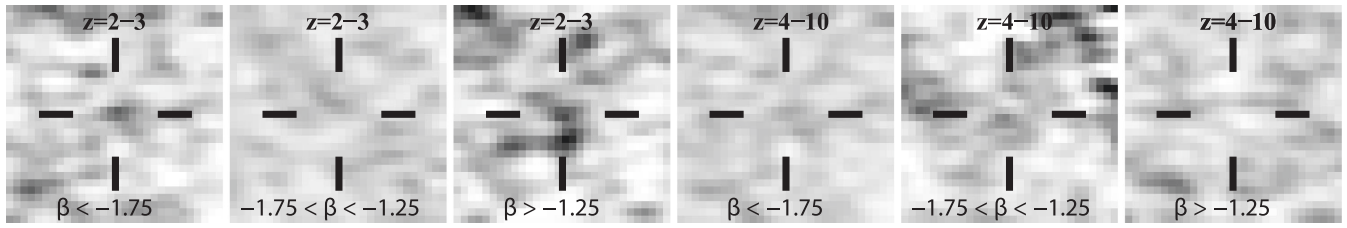
Figure 11. Stacked 1.2 mm continuum images ($9'' \times 9''$) for $z = 2$–3 and $z = 4$–10 galaxies falling in different bins of UV-continuum slope β. All sources that are individually detected at $\geqslant 4\sigma$ are not included in the presented stack results. Only the most massive ($>10^{9.75}\, M_\odot$) sources are included in our $z = 2$–3 stacks, while our $z = 4$–10 stacks include sources over the full mass range (due to the small number of sources with $>10^{9.75}\, M_\odot$). In the stacks, sources are weighted according to the expected 1.2 mm continuum flux (assuming $L_{\rm IR} \propto L_{\rm UV}$) and according to the inverse square of the noise. The three individually detected sources (at $>4\sigma$) are not included in the presented stack results.
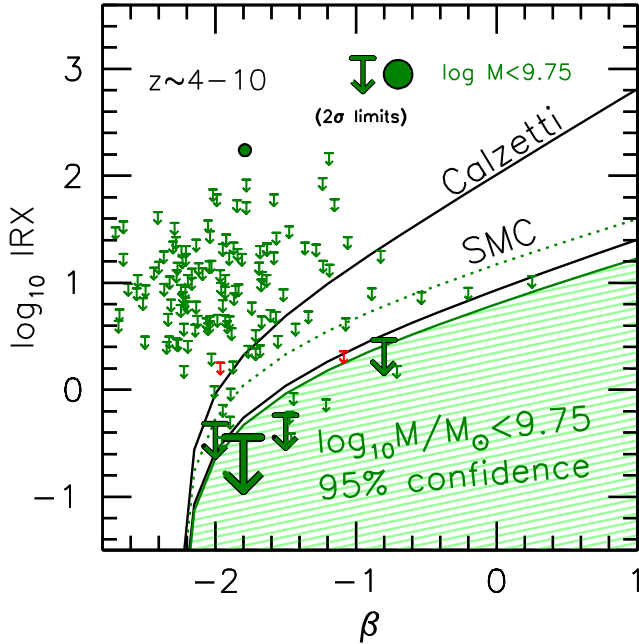
Figure 12. Stacked constraints on the infrared excess in $z = 4$–10 galaxies vs. β. Similar to Figure 10 but for galaxies in the redshift range $z = 4$–10. We present results only for the lower-mass subsample, because we find only two $>10^{9.75}\, M_\odot$ galaxies over the 1 arcmin^2 ASPECS region and those two sources are not detected. Our stack results (indicated by the larger downward-pointing arrows which express the 2σ upper limits) strongly suggest that the infrared excess for the typical lower-mass $<10^{9.75}\, M_\odot$ galaxy is low, even below that expected for an SMC dust law. The very large downward-pointing arrow is as in Figure 10, but for $z = 4$–10 galaxies. The light-green shaded region gives our derived constraints (95% confidence intervals) on the IRX–β relationship for $z = 4$–10 galaxies with all but the highest stellar masses ($<10^{9.75}\, M_\odot$). The dotted green line indicates the upper bound on this region if the dust temperature is much higher at $z = 4$–10 than at $z \sim 1.5$ (i.e., 44–50 K as suggested by the results of Béthermin et al. 2015).

Table 6
Present Constraints on the IRX–β Relationship

Sample	Mass Range	$dA_{\rm UV}/d\beta$
	Current Determinations	
$z \sim 2$–3	$>10^{9.75}\, M_\odot$	$1.26^{+0.27}_{-0.36}$
$z \sim 2$–3	$<10^{9.75}\, M_\odot$	<1.22[a]
$z \sim 4$–10	$<10^{9.75}\, M_\odot$	<0.97[a,b]
	Canonical IRX–β Relations	
Meurer/Calzetti		1.99
SMC		~ 1.10

Notes.
[a] Upper limits are 2σ.
[b] Upper limit is corrected for the expected noise in the derived β values.

NGC 6946 from Silva et al. (1998). The typical amplitude of these dependencies is a factor of 3 at $z \sim 2$–3, a factor of 2 at $z \sim 6$, and a factor of <1.5 at $z \sim 8$–10.

While we would expect some uncertainties in the infrared excesses or IR luminosities we derive from the ALMA data, we have verified that the derived values are nonetheless plausible in the redshift range $z \sim 2$–3 by comparing them with independent estimates made from the MIPS 24 μm observations and using a prescription from Reddy et al. (2010) to convert these 24 μm fluxes to IR luminosities (Appendix B). The IR luminosities we derive for the few detected sources agree to within 0.3 dex with the ALMA-estimated luminosities (Table 10 from Appendix B) if we adopt a fiducial dust temperature of 35 K. Even better agreement is obtained if we adopt higher values for the dust temperature.

3.5. Synthesis of the Present Results with Earlier $z = 5$–6 Results from ALMA

Finally, we combine the current constraints on the infrared excess with those available in the literature to construct a more complete picture of the impact of dust obscuration on the overall energy output from star-forming galaxies at $z = 4$–10.

We focus in particular on constraints available from ALMA on luminous $z = 4$–10 galaxies due to the limited number of sources within the 1 arcmin^2 footprint of ASPECS. We focus on 12 fairly luminous $z = 5$–7 galaxies originally identified as part of wide-area surveys in the rest-frame UV (e.g., Willott et al. 2013) and recently examined with ALMA by Capak et al. (2015) and Willott et al. (2015). Results from those studies are particularly useful, since the 1.2 mm continuum fluxes, UV luminosities, and estimates of the stellar mass for individual sources are available. Six of the 12 galaxies from those two studies show tentative detections in the available ALMA data.

Combining our own results with those from Capak et al. (2015) and Willott et al. (2015)—self-consistently converting the observed ALMA fluxes to IR luminosities—we present our IRX versus stellar mass constraints in Figure 13 with the solid blue squares and large blue upper limits. For context, we compare these results with the consensus IRX–stellar mass relationship we derive from various results on IRX–mass found at $z \sim 2$–3 (Reddy et al. 2010; Whitaker et al. 2014; Álvarez-Márquez et al. 2016: see Appendix A).

For the case of a fixed dust temperature of 35 K, we find we can approximately match the current constraints at $z = 4$–10 (light thick dotted blue line in Figure 13) using the consensus IRX–stellar mass relationship at $z \sim 2$–3 if sources of a given stellar mass exhibit IR luminosities at least ~ 0.5 dex lower than
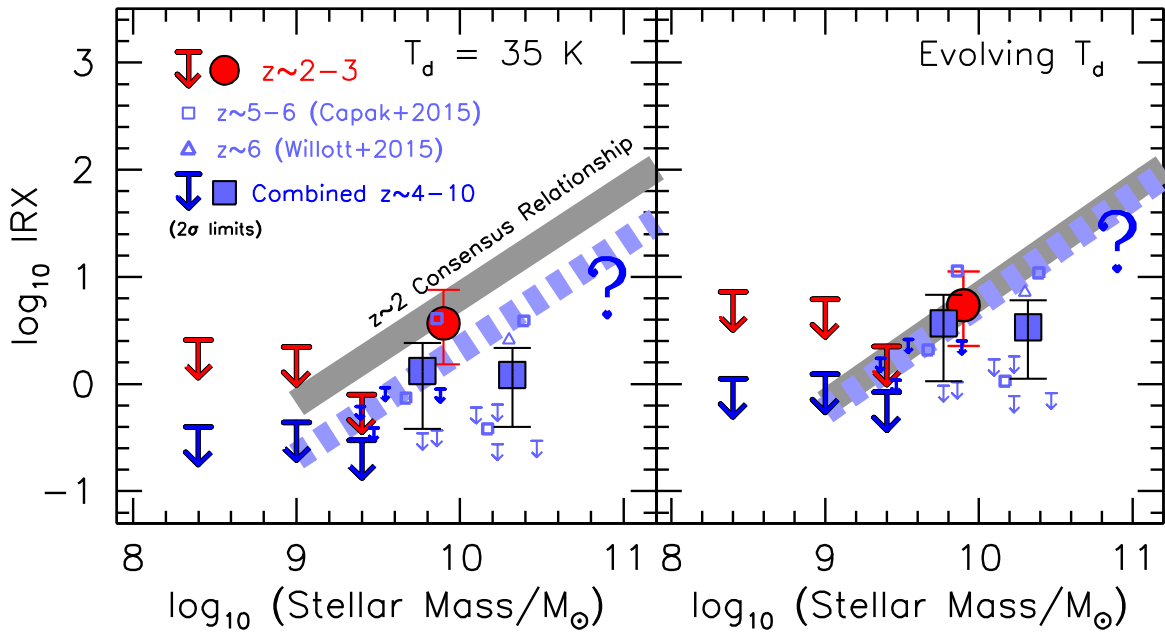
Figure 13. Constraints on the infrared excess as a function of stellar mass including selected results from the literature (*large solid blue squares*), assuming a fixed dust temperature of 35 K (*left panel*) and a dust temperature that increases monotically toward higher redshift as found by Béthermin et al. (2015: *right panel*). Large downward-pointing arrows indicate 2σ upper limits on the infrared excess for the average sources, after combining results from the literature with the current constraints. The specific results for the infrared excess from individual sources in the studies of Capak et al. (2015: *open blue squares*) and Willott et al. (2015: *open blue triangles*) are explicitly shown. Blue downward arrows indicate 2σ upper limits on the inferred infrared excesses seen in five sources from the study of Capak et al. (2015). The thick light blue dotted line shows one potential IRX–stellar mass relationship at $z \sim 4$–10 that roughly fits the available constraints. For fixed dust temperature (*left panel*), this is possible by shifting the consensus IRX–stellar mass relationship at $z \sim 2$–3 (*thick gray line*) to lower values of the dust extinction (and the observational constraints may support an even larger shift than the 0.5 dex shift presented) while for a monotonically increasing dust temperature (*right panel*) no evolution in the consensus IRX–stellar mass relationship is required to match current high-redshift results.

at $z \sim 2$–3. This would suggest lower dust extinctions at high redshift at a fixed stellar mass.

However, we should also look at how evolution in the dust temperature could impact the results. If the dust temperature exhibited a monotonic increase toward higher redshift, e.g., as found by Magdis et al. (2012) and Béthermin et al. (2015), we would infer much higher (by ~ 0.4–0.5 dex) IR luminosities for the detected sources from the three samples considered here. This would translate into similarly higher infrared excesses at $z = 4$–10, which would be plausibly consistent with the IRX–stellar mass relationship at $z = 0$–3 (right panel of Figure 13), suggesting no significant evolution in this relationship from $z \sim 6$ to $z \sim 0$.

Pannella et al. (2015) found no strong evidence for evolution in the IRX–stellar mass relation to $z \sim 3.5$. Recent $z \sim 3$–5 results on the average infrared excess for bright $z \sim 3$–5 galaxies by Coppin et al. (2015), where IRX ~ 5–6 (drawing values from their Table 2) for sources with UV SFRs of ~ 18–33 (corresponding to a stellar mass of $\log_{10}(M/M_{\odot}) \sim 9.8$: Duncan et al. 2014), are also consistent with no evolution in the IRX–stellar mass relation to $z \sim 5$ (assuming minimal biases from stacking). While one might expect some evolution in this relationship due to the observed evolution in the mass–metallicity relation (e.g., Erb et al. 2006a), it is possible that higher amounts of gas and mass in the interstellar medium in $z \gtrsim 2$ galaxies could

compensate for the lower metal content to produce a relatively unevolving IRX–stellar mass relation (Tan et al. 2014).

4. DISCUSSION

4.1. Is Dust Emission from Lower-mass Galaxies Really Negligible at $z \gtrsim 3$?

The results we obtained in the previous section imply that dust emission from lower-mass galaxies is not large, particularly relative to the emission from galaxies in the rest-frame UV and as apparent at 1.2 mm. The relative energy outputs in the IR from the "average" $< 10^{9.25}\,M_{\odot}$ and $< 10^{9.75}\,M_{\odot}$ galaxies in our HUDF selection are estimated to be less than 42% and 32% (95% confidence), respectively, of what galaxies emit at rest-frame UV wavelengths (Table 12 from Appendix D).

4.1.1. Comparison with $z \sim 2$ Spectroscopic Results

One can obtain a quick check on these results by inspecting the results from spectroscopy, particularly measurements of the Balmer decrement in $z \sim 2$ galaxies. Encouragingly, the decrements seen in results from the MOSDEF program (Kriek et al. 2015) seem consistent with lower-mass, lower-SFR systems showing low dust extinction. This is perhaps most clearly seen by inspecting Figure 20 of Reddy et al. (2015), where galaxies with SFRs $\lesssim 10\,M_{\odot}\,\mathrm{yr}^{-1}$ show an $H\alpha/H\beta$ flux

ratio of approximately 3, very close to the intrinsic ratio. This points to little dust extinction in galaxies with lower SFRs.

4.1.2. Do Examples of Low-mass but IR-luminous z ≳ 2 Galaxies Exist?

The present results prompt us to consider whether well-known examples of $z \gtrsim 2$ galaxies in the literature stand in significant violation of these findings, i.e., whether there are sources that are far-IR luminous despite having lower stellar masses.

Perhaps the most prominent source that potentially stands in violation of these general findings is the bright $z \sim 7.5$ galaxy A1689-zD1 initially identified behind Abell 1689 by Bradley et al. (2008), with an estimated stellar mass of $\sim 1.6 \times 10^9 \, M_\odot$ (Watson et al. 2015). Despite its low mass, Knudsen et al. (2016) report a 12σ detection of the source in far-IR continuum observations with ALMA, implying an infrared excess of ~ 3 for the source (Watson et al. 2015). The reported IRX is much higher than our 2σ upper limits we can set on the stack results, suggesting that such a result (if true) is atypical for the $\ll 10^{9.75} \, M_\odot$ population.

There are also five sources out of 122 (4%) followed up by the ALESS survey with ALMA (da Cunha et al. 2015) with estimated stellar masses $< 10^{9.75} \, M_\odot$ which nevertheless show moderately high IR luminosities of $\sim 10^{10.5}$ to $\sim 10^{11.6} \, L_\odot$. Likewise, seven sources out of the 48 sources (15%) from the AzTEC/ASTE survey (Scott et al. 2010), also identified based on their IR properties, have stellar masses below $10^{9.75} \, M_\odot$. Additionally, from the Capak et al. (2015) sample of ~ 10 $z = 5$–6 galaxies, there is one source (HZ4) below our $10^{9.75} \, M_\odot$ threshold (stellar mass of $10^{9.67 \pm 0.21} \, M_\odot$), which nonetheless has a moderately high IR luminosity ($10^{11.13} \, L_\odot$).

As more ALMA constraints become available for lower-mass $z \geqslant 2$ galaxies, it will be important to see if any other sources are found to be so bright in the far-IR.

4.2. Prescription for the Average Infrared Excess in Star-forming Galaxies at z ≳ 3

Synthesizing the results from our own program with those from other programs, we can derive an approximate expression for the average infrared excess in star-forming galaxies. For sources with stellar masses in excess of $10^{9.75} \, M_\odot$, we find that the IRX–β relationship is most consistent with an SMC IRX–β relation. While many previous studies (e.g., Reddy et al. 2006, 2010; Daddi et al. 2007) found evidence that the highest-mass sources followed an IRX–β relation such as that of Calzetti et al. (2000) or M99, implying more obscured star formation, here we are probing a smaller volume, and the highest-mass sources from the present study may not be especially dissimilar from the lowest-mass sources in many previous studies. For sources with stellar masses of $10^{10} \, M_\odot$ and less, many previous studies also found evidence for an SMC IRX–β relation in $z \sim 2$ galaxies, e.g., Baker et al. (2001), Reddy et al. (2006: their Figure 10), Reddy et al. (2010), and Siana et al. (2008, 2009).

Indeed, the present ALMA results are interesting in that they allow us to extend these analyses into an even lower mass regime than was generally studied before. Despite some dependence on the assumed SED template, our results suggest that dust emission from these lower-mass sources is much less significant than for even our high-mass subsample, i.e., with an

IRX not larger than 0.40 (2σ) assuming $T_d \sim 35$ K. Even if we conservatively adopt a modified blackbody SED with an evolving dust temperature similar to that found by Béthermin et al. (2015), our results imply that the infrared excess for lower-mass galaxies is not larger than 0.94 (2σ).

These results recommend to us a relatively simple recipe for the infrared excess of star-forming galaxies at $z \gtrsim 2$. For galaxies with stellar masses of $> 10^{9.75} \, M_\odot$, we make use of an IRX–β relationship intermediate between the dust laws of the SMC and Calzetti et al. (2000):[29]

$$A_{\rm UV} = 1.5(\beta + 2.23). \tag{4}$$

For galaxies with stellar masses below $10^{9.75} \, M_\odot$, the dust extinction is much lower, as demonstrated, e.g., by our own results. For such systems, we postulate that IRX can be derived more reliably by using the correlation between IRX and stellar mass. Utilizing the IRX–stellar mass relationship from the previous section (keeping in mind the ± 0.2 dex uncertainties), we propose that

$$\log_{10} {\rm IRX} = \log_{10}[M/M_\odot] - 9.67 \tag{5}$$

where M is the inferred stellar mass (assuming a fixed dust temperature of 35 K). If the dust temperature evolves with cosmic time as found by Béthermin et al. (2015), i.e., as $(1 + z)^{0.32}$ (Section 3.1.3), the latter expression could plausibly be replaced by $\log_{10} {\rm IRX} = \log_{10}[M/M_\odot] - 9.17$, i.e., approximately the same relationship as at $z = 0$–3 (see Section 3.5). Encouragingly enough, the IRX–stellar mass prescription we apply in the low-mass regime (Equation (5)) gives very similar estimates for the dust corrections in the high-mass regime ($> 10^{9.75} \, M_\odot$) as we find using our primary prescription (which relies on an IRX–β relationship). As such, there is a basic consistency to the present approach (despite some arbitrariness in how one parameterizes IRX in terms of various physical variables, i.e., stellar mass, β, or even the SFR itself).

With future data—including both deeper and wider continuum mosaics with ALMA—it should be possible to improve on this prescription. Particularly valuable will be observations at bluer wavelengths (closer to the peak of the far-IR emission: see Figure 1) and complementary information from other probes, i.e., stacks of the PACS fluxes, X-ray, and near-IR spectra for even lower-mass sources. In addition, a measurement of the Balmer decrement out to $z \sim 6$ should soon be possible with the *James Webb Space Telescope*.

5. IMPLICATIONS OF THESE RESULTS

5.1. Inferred Dust Corrections for z ≳ 3 Samples

The purpose of this section is to determine the approximate correction we should apply to the observed UV luminosity densities to correct for dust extinction and therefore obtain the SFR density.

We base our estimates of dust extinction on the large catalog of $z = 4$–10 galaxies from Bouwens et al. (2015a) in the CANDELS GOODS-North, GOODS-South, and Early Release Science (Windhorst et al. 2011) fields. Critically, each of the

---

[29] The dust-free UV-continuum slope β would plausibly be bluer at earlier times due to a younger average age of the stellar population (Wilkins et al. 2013; Castellano et al. 2014), potentially decreasing the intrinsic slope of -2.23 by ~ 0.2 to ~ -2.5.

$z \sim 2$–10 galaxies in these fields possesses individually estimated stellar masses and UV-continuum slopes β, all derived on the basis of the deep *HST* and *Spitzer*/IRAC photometry available over the GOODS-North and South (Labbé et al. 2015). Stellar mass, in particular, is an important variable to establish given its utility for predicting the IR luminosity and infrared excess for individual galaxies. In addition, as we saw in Section 3.3.2, the estimated stellar mass clearly impacts the dependence of IRX on β.

We estimate the dust correction in individual 0.5 mag bins of UV luminosity. For each bin, we first consider what fraction of galaxies have stellar masses in excess of $10^{9.75}\, M_{\odot}$. For galaxies in this mass range, we compute the estimated dust correction based on an IRX–β relation intermediate between those of the SMC and Calzetti et al. (2000) that utilizes the β distribution measured for such high-mass galaxies. In making use of the observed β's to derive the correction for galaxies in a given luminosity bin, we either make use of the full distribution of β's derived for individual sources (where the typical uncertainty in the β's measured for individual sources is <0.3) or make use of a model distribution (where the typical uncertainty in β is >0.3). The UV-continuum slope β we measure for an individual source is estimated based on the fit of a power-law slope to its UV-continuum fluxes (e.g., Castellano et al. 2012), avoiding those flux measurements that could be impacted by absorption by the intergalactic medium or rest-frame optical $\gtrsim 3500$ Å light.[30]

However, for galaxies with estimated stellar masses $<10^{9.75}\, M_{\odot}$, we derive the dust correction from the prescription given in Equation (5).

The top panel of Figure 14 shows the fraction of galaxies in our $z \sim 4$, $z \sim 5$, $z \sim 6$, and $z \sim 7$ samples whose estimated stellar masses exceed $10^{9.75}\, M_{\odot}$. As expected, the fraction of sources with masses $>10^{9.75}\, M_{\odot}$ is relatively high for the brightest sources in the rest-frame UV, but decreases rapidly faintward of -21 mag, and is <3% at -19 mag.

In the middle panel of Figure 14, we present the dust corrections we estimate for our samples based on our ALMA results and using the prescription that we describe above. The dust correction we estimate is only particularly significant at $M_{\mathrm{UV,AB}} < -21$ mag and becomes negligible faintward of -20 mag. In the bottom panel of Figure 14, we present an alternative estimate of the dust correction assuming that IRX–stellar mass relation does not evolve from $z \sim 0$–3 to $z \sim 7$ (partially motivated by the findings in the right panel of Figure 13).

We can determine the approximate impact of dust corrections on the inferred SFR densities at $z > 3$ by multiplying the UV luminosity function (LF) by the inferred dust corrections and integrating to specific faint-end limits. For convenience, these dust corrections are presented in Table 7. For the brightest (<25.5 mag) galaxies in the rest-frame UV at $z \sim 3$, we assume (e.g., Reddy & Steidel 2004) that the average dust correction for UV-bright (<25.5 mag) galaxies at $z \sim 3$ is ~ 5.

For the case of an evolving IRX–stellar mass relation, the corrections are smaller (by ~ 0.2 dex) than earlier correction factors (e.g., Madau & Dickinson 2014, Bouwens et al. 2015a). This can be seen by comparing the dust extinction estimates in

---
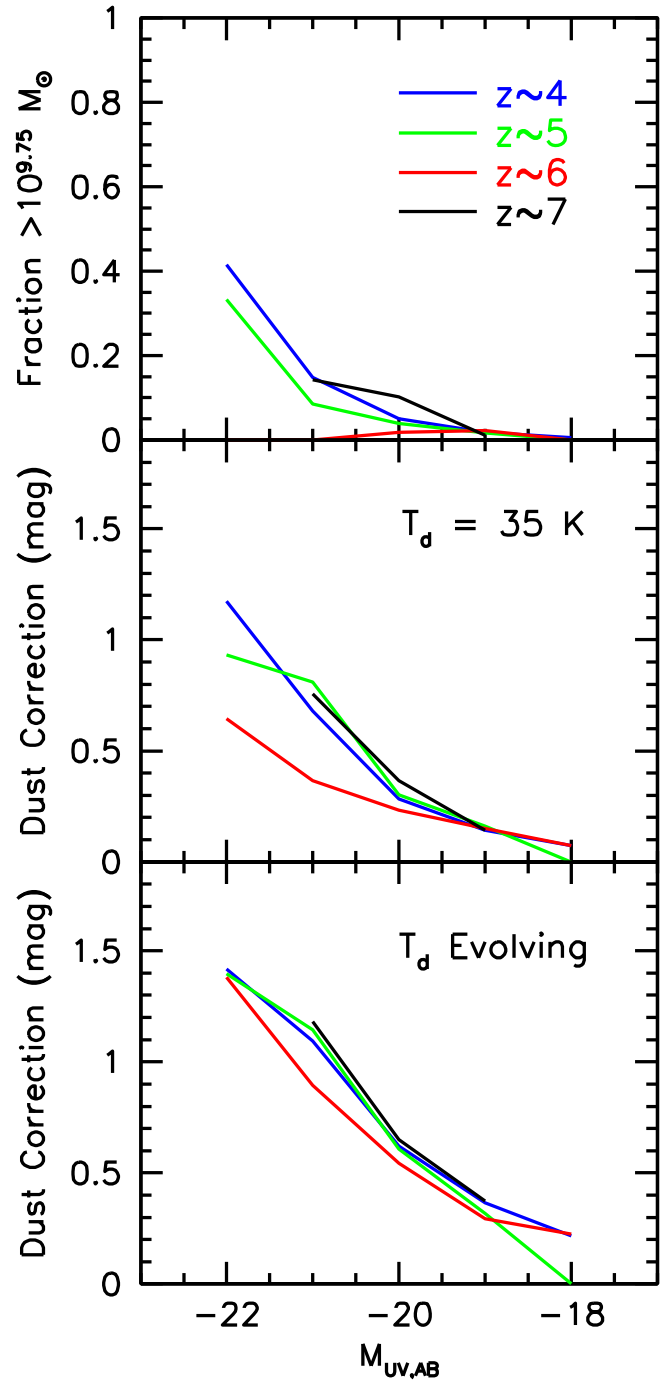
Figure 14. Upper panel: Fraction of $z \sim 4$ (*blue line*), $z \sim 5$ (*green line*), $z \sim 6$ (*red line*), and $z \sim 7$ (*black line*) galaxies in a given 0.5 mag bin of UV luminosity estimated to have a stellar mass in excess of $10^{9.75}\, M_{\odot}$ where the dust extinction appears to be especially significant. Middle panel: Estimated correction for dust extinction vs. UV luminosity for $z \sim 4$ (*blue line*), $z \sim 5$ (*green line*), $z \sim 6$ (*red line*), and $z \sim 7$ (*black line*). For sources with stellar masses in excess of $10^{9.75}\, M_{\odot}$, dust extinction is computed using the M99 IRX–β relation, while for those with stellar masses lower than $10^{9.75}\, M_{\odot}$, dust extinction is computed based on the consensus $z \sim 2$–3 IRX–stellar mass relation (but shifted lower by 0.5 dex). Lower panel: Similar to the middle panel, but computing dust extinction for the lowest-mass galaxies assuming no evolution in the IRX–stellar mass relation from $z \sim 0$–3 (appropriate if the dust temperature increases monotonically to high redshifts). See Figure 13.

the middle set of rows in Table 8 (to be presented in Section 5.2) with the top set of rows.

However, if the IRX–stellar mass relation does not evolve significantly from $z \sim 0$ to $z \sim 6$ (i.e., as in the right panel of

Table 7
Estimated Dust Corrections to Apply the Results of UV Luminosity Density to Various Faint-End Limits

	log₁₀(Dust Correction)	
Sample	($>0.05\ L^*_{z=3}$)[a]	($>0.03\ L^*_{z=3}$)[a]
Assuming $T_d = 35$ K (fixed)		
$z \sim 3$	0.37[b]	0.34[b]
$z \sim 4$	0.15	0.14
$z \sim 5$	0.16	0.14
$z \sim 6$	0.09	0.07
$z \sim 7$	0.04	0.03
$z \sim 8$	0.04	0.03
Assuming Evolving T_d[c]		
$z \sim 3$	0.37[b]	0.34[b]
$z \sim 4$	0.27	0.25
$z \sim 5$	0.27	0.24
$z \sim 6$	0.21	0.18
$z \sim 7$	0.09	0.07
$z \sim 8$	0.08	0.06

Notes.
[a] The specified limits 0.05 $L^*_{z=3}$ and 0.03 $L^*_{z=3}$ correspond to faint-end limits of −17.7 and −17.0, respectively, which is the limiting luminosity to which $z \sim 7$ and $z \sim 10$ galaxies can be found in current probes (Ellis et al. 2013; McLure et al. 2013; Oesch et al. 2013b; Schenker et al. 2013; Bouwens et al. 2015a).
[b] For uniquely the $z \sim 3$ sample, we make use of the finding by, e.g., Reddy & Steidel (2004) and Reddy et al. (2010) that the average infrared excess for galaxies brighter than 25.5 mag at $z \sim 3$ is a factor of ~5.
[c] We adopt $T_d = ((1 + z)/2.5)^{0.32}(35$ K) for the evolution following Béthermin et al. (2015). See Section 3.1.3.

Figure 13), our estimated dust corrections are only slightly smaller (~0.1 dex) than inferred in earlier work. Previously, Capak et al. (2015) had also considered the impact of new ALMA results for the implied SFR densities at $z \sim 4$–7, finding suggestive evidence for smaller dust corrections than had previously been utilized.

5.2. Implied SFR Densities at $z \geqslant 3$

We apply the dust corrections we derived in the previous sections to the UV luminosity densities and integrate the UV LF of Bouwens et al. (2015a) to 0.05 $L^*_{z=3}$ (−17.7 mag) and to 0.03 $L^*_{z=3}$ (−17.0 mag). Both the dust corrections and UV LFs were derived over a similar range in UV luminosity, so this process is self-consistent.

As in previous work, the UV luminosity densities are converted into SFR densities using canonical relationships of Madau et al. (1998) and Kennicutt (1998):

$$L_{\rm UV} = \left(\frac{\rm SFR}{M_\odot\,{\rm yr}^{-1}}\right) \times\ 8.0\ \times\ 10^{27}\ {\rm erg\ s}^{-1}\ {\rm Hz}^{-1}. \qquad (6)$$

This relationship assumes a Salpeter (1955) IMF and a constant SFR for 100 million years. We also apply these dust corrections to the LF results of Reddy & Steidel (2009) and McLure et al. (2013).

Our quantitative results for the corrected and uncorrected SFR densities at $z \sim 3$–10 are presented in Table 8. In deriving the corrected SFR densities, we take the uncertainty in the dust correction to be equal to the difference in the estimated dust corrections found by adopting a fixed dust temperature of 35 K and allowing for an evolving dust temperature as implied by

the results of Béthermin et al. (2015). We also present the derived SFR densities along with many previous estimates (Schiminovich et al. 2005; Reddy & Steidel 2009; McLure et al. 2013) in Figure 15.

Of course, in computing the total SFR density from galaxies, we must account not only for the contribution from UV-selected galaxies, but also for the more massive, far-infrared bright sources where standard dust corrections are not effective or which are sufficiently faint in the UV to be entirely missed in standard LBG searches (estimated by Reddy et al. 2008 to occur when galaxies have IR luminosities $>10^{12}\ L_\odot$). Such sources are known to contribute a substantial fraction of the SFR density at $z \sim 0$–2 (Karim et al. 2011; Magnelli et al. 2013; Madau & Dickinson 2014). We account for this contribution by using published IR LFs to integrate those galaxies with IR luminosities $>10^{12}\ L_\odot$. While one might be concerned this would "double count" the SFR coming from specific sources, it has been argued (e.g., Reddy et al. 2008) that the full SFR from such sources would not be properly accounted for in UV-selected samples (for reasons specified at the beginning of this paragraph).

We utilize the results of Magnelli et al. (2013) at $z \sim 0$–2 (which build on the results of Caputi et al. 2007 and Magnelli et al. 2009, 2011), Reddy et al. (2008) at $z \sim 3$, Daddi et al. (2009) and Mancini et al. (2009) at $z \sim 4$, Dowell et al. (2014) at $z \sim 5$, and Riechers et al. (2013) at $z \sim 6$ (see also Wang et al. 2009; Boone et al. 2013; Asboth et al. 2016). All together these results suggest obscured SFR densities of 0.025, 0.01, 0.001, and $< 0.0003\ M_\odot\ {\rm yr}^{-1}\ {\rm Mpc}^{-3}$ at $z \sim 3$, $z \sim 4$, $z \sim 5$, and $z \sim 6$, respectively.

We combine these SFR densities with those we derived by correcting the UV LFs at $z = 3$–10 to present our best estimates for the SFR density at $z = 3$–10 in Table 8 and Figure 15, alternatively assuming a fixed dust temperature $T_d \sim 35$ K and supposing that the dust temperature increases monotonically toward high redshift as found by Béthermin et al. (2015). For context, we also present in Table 8 the SFR density that Bouwens et al. (2015a) estimated based on the M99 IRX–β relationship and making use of the observed β distribution at $z \sim 4$–10.

Figure 16 shows the fraction of the SFR density that would be directly observable in the rest-frame UV and also in the IR. This figure is an update to Figure 12 from Bouwens et al. (2009). Similar to the findings from Bouwens et al. (2009), we find that most of the SFR density at $z > 4.5$ would be observable in the rest-frame UV.

5.3. Implications for the Lyman Continuum Photon Production Efficiencies

Another consequence of our new ALMA results is for the interpretation of the prominent Hα emission lines inferred in galaxies at $z \sim 4$–5 based on the observed *Spitzer*/IRAC 3.6 μm and 4.5 μm fluxes (e.g., Schaerer & de Barros 2009; Shim et al. 2011; Stark et al. 2013).

As first noted by Shim et al. (2011), the total Hα luminosities of galaxies at $z \sim 4$–5 are in excess of what one might expect based on their luminosities in the rest-frame UV. The excess is conservatively as large as a factor of 2 using the general $z \sim 4$–5 LBG selections (Smit et al. 2015) but was earlier reported to be a factor of 6 (Shim et al. 2011) using samples selected based on their emission line properties. One explanation for these high luminosities would be if the selected

Table 8
UV Luminosity Densities and Star Formation Rate Densities to −17.0 AB mag (0.03 $L_{z=3}^{*}$)

Lyman Break Sample	$\langle z \rangle$	$\log_{10} \mathcal{L}$ (erg s^{-1} Hz^{-1} Mpc^{-3})[a]	Dust Correction (dex)[b]	$\log_{10}$ SFR density ($M_{\odot}$ Mpc^{-3} yr^{-1}) Uncorrected	Corrected	Incl. ULIRG[b]
			M99 IRX–β (as in Bouwens et al. 2015)			
B	3.8	26.52 ± 0.06	0.42	-1.38 ± 0.06	-1.00 ± 0.13	-0.96 ± 0.13
V	4.9	26.30 ± 0.06	0.35	-1.60 ± 0.06	-1.26 ± 0.12	-1.25 ± 0.12
i	5.9	26.10 ± 0.06	0.25	-1.80 ± 0.06	-1.55 ± 0.13	-1.55 ± 0.13
z	6.8	25.98 ± 0.06	0.23	-1.92 ± 0.06	-1.69 ± 0.07	-1.69 ± 0.07
Y	7.9	25.67 ± 0.06	0.15	-2.23 ± 0.06	-2.08 ± 0.07	-2.08 ± 0.07
			Fiducial Estimates: Assuming $T_d = 35$ K (fixed)			
U	3.0	26.55 ± 0.06	0.44	-1.35 ± 0.03	-1.01 ± 0.09	-0.91 ± 0.09
B	3.8	26.52 ± 0.06	0.21	-1.38 ± 0.06	-1.24 ± 0.13	-1.17 ± 0.13
V	4.9	26.30 ± 0.06	0.15	-1.60 ± 0.06	-1.46 ± 0.12	-1.45 ± 0.12
i	5.9	26.10 ± 0.06	0.08	-1.80 ± 0.06	-1.73 ± 0.13	-1.72 ± 0.13
z	6.8	25.98 ± 0.06	0.03	-1.92 ± 0.06	-1.89 ± 0.07	-1.89 ± 0.07
Y	7.9	25.67 ± 0.06	0.03	-2.23 ± 0.06	-2.20 ± 0.07	-2.20 ± 0.07
J	10.4	$24.62^{+0.36}_{-0.45}$	0.00	$-3.28^{+0.36}_{-0.45}$	$-3.28^{+0.36}_{-0.45}$	$-3.28^{+0.36}_{-0.45}$
			Assuming Evolving T_d[c]			
B	3.8	26.52 ± 0.06	0.30	-1.38 ± 0.06	-1.13 ± 0.13	-1.08 ± 0.13
V	4.9	26.30 ± 0.06	0.25	-1.60 ± 0.06	-1.36 ± 0.12	-1.35 ± 0.12
i	5.9	26.10 ± 0.06	0.20	-1.80 ± 0.06	-1.61 ± 0.13	-1.60 ± 0.13
z	6.8	25.98 ± 0.06	0.07	-1.92 ± 0.06	-1.85 ± 0.07	-1.85 ± 0.07
Y	7.9	25.67 ± 0.06	0.06	-2.23 ± 0.06	-2.17 ± 0.07	-2.17 ± 0.07

Notes.
[a] Integrated down to 0.03 $L_{z=3}^{*}$. Based upon LF parameters in Table 2 of Bouwens et al. (2015a, see Section 6.1). The SFR density estimates assume $\gtrsim$100 Myr constant SFR and a Salpeter IMF (e.g., Madau et al. 1998). Conversion to a Chabrier (2003) IMF would result in a decrease by a factor of ~1.8 (0.25 dex) in the SFR density estimates given here.
[b] This factor includes both the impact of dust on the $z = 3$–8 UV luminosity densities and also the contribution of far-IR bright ($>10^{12} L_{\odot}$) galaxies, which might be missed in typical probes of Lyman-break galaxies or which might have their IR luminosities underestimated (Reddy et al. 2006; Reddy & Steidel 2009).
[c] We adopt $T_d = ((1 + z)/2.5)^{0.32}(35$ K) for the evolution following Béthermin et al. (2015). See Section 3.1.3.

galaxies predominantly had young stellar ages (given that the Lyα emission was prominent in the spectroscopic sample considered by Shim et al. 2011) or if dust extinction preferentially had a larger impact on the observed UV-continuum fluxes than it did on the observed Hα fluxes (Marmol-Queralto et al. 2016; Smit et al. 2015).

Neither mechanism appears to provide a fully satisfactory explanation for the high Hα fluxes in $z \sim 5$ galaxies. Dust extinction falls off rapidly toward lower masses, but the Hα EWs in these sources remain essentially unchanged (or possibly increase toward lower mass: see Smit et al. 2015). Similarly, young ages for the $z \sim 4$–5 galaxy population cannot provide an explanation, because a high ratio of Hα to UV continuuum is observed for typical star-forming galaxies at $z \sim 4$–5 (Marmol-Queralto et al. 2016; Smit et al. 2015).[31]

This essentially forces us to conclude that the observed ratio of Hα to UV-continuum luminosity must be intrinsic and that star-forming galaxies indeed have very high Hα luminosities relative to their luminosities in the UV continuum, particularly in comparison with conventional stellar population models (i.e., Bruzual & Charlot 2003). It has been speculated that such could be achieved due to binarity or rapid rotation in massive stars,

allowing them to output large amounts of ionizing radiation tens of million of years after an initial burst of star formation (e.g., Yoon et al. 2006; Eldridge & Stanway 2009, 2012; Levesque et al. 2012; de Mink et al. 2013; Kewley et al. 2013; Leitherer et al. 2014; Gräfener & Vink 2015; Szécsi et al. 2015). Changes to the IMF might also be a possibility (e.g., if there are a larger number of high-mass stars), but are disfavored given the general agreement between the observed stellar mass density and the integrated SFR densities (e.g., Stark et al. 2013).

These high ratios of Hα to UV continuum have implications for the Lyman-continuum photon production efficiencies $\xi_{\rm ion}$ used in reionization modeling. In Bouwens et al. (2015c), we pioneered the use of the relative luminosities in Hα and the UV continuum to estimate these efficiencies. Our results were consistent with the high-end assumed values for this efficiency in the literature, but were moderately sensitive to our assumptions about the dust extinction. Specifically, we derived intrinsic values of $\log_{10} \xi_{\rm ion}/({\rm Hz\ erg\ s^{-1}})$ of $25.27^{+0.03}_{-0.03}$ and $25.33^{+0.02}_{-0.03}$ assuming a Calzetti dust law and an SMC one, respectively (where the systematic errors are likely 0.06 dex: see Section 3.3 of Bouwens et al. 2016). These compare to various canonical values ranging from 25.20 to 25.30 in the literature (e.g., Madau et al. 1999; Kuhlen & Faucher-Giguère 2012; Robertson et al. 2013).

The present ALMA results suggest that the dust extinction in $z \sim 4$–5 galaxies is likely to be quite low. It is therefore interesting to estimate the mean Lyman-continuum photon

---

[31] Shim et al. (2011) had speculated that young ages might explain the high ratios of Hα to UV continuum observed in $z \sim 4$–5 galaxies they studied that showed strong Lyα emission. However, it is now clear that such ratios apply both to sources that show Lyα in emission and to those that do not (Smit et al. 2015).
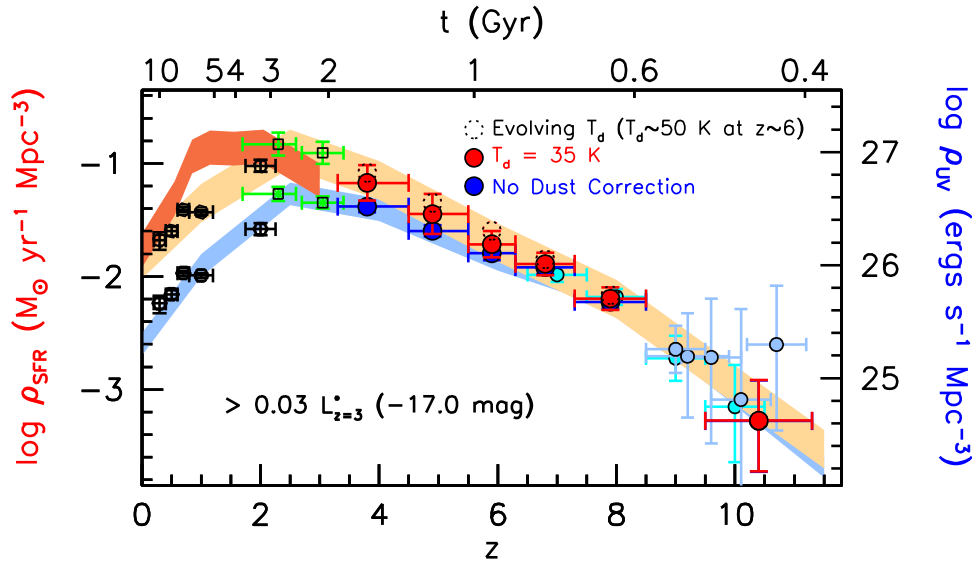
Figure 15. Updated determinations of the derived SFR (*left axis*) and UV luminosity (*right axis*) densities vs. redshift (Section 5.4). The left axis gives the SFR densities we would infer from the measured luminosity densities, assuming the conversion factor of Madau et al. (1998) relevant for star-forming galaxies with ages of $\gtrsim 10^8$ yr (see also Kennicutt 1998). The right axis gives the UV luminosities we infer by integrating the present and published LFs to a faint-end limit of -17 mag ($0.03\,L^*_{z=3}$)—which is the approximate limit we can probe to $z \sim 8$ in our deepest data set. The upper and lower sets of points (*red and blue circles,* respectively) and shaded regions show the SFR and UV luminosity densities corrected and uncorrected for the effects of dust extinction. The dust correction we utilize relies on an IRX–β relation intermediate between SMC and Calzetti for the highest-mass galaxies in the present samples, i.e., $>10^{9.75}\,M_\odot$, but an IRX–stellar mass relation for lower-mass sources (Section 4.2). The dotted black open circles indicate the dust-corrected SFR densities, assuming an unevolving IRX–stellar mass relation (appropriate if the dust temperature increases monotonically toward high redshift: see Figure 13). The dark red shaded region include the contribution from IR-bright sources (Magnelli et al. 2009, 2011, 2013). Also shown are the SFR densities at $z \sim 2$–3 from Reddy et al. (2009: *green crosses*), at $z \sim 0$–2 from Schiminovich et al. (2005: *black hexagons*), at $z \sim 7$–9 from McLure et al. (2013) and Ellis et al. (2013: *cyan solid circles*), and at $z \sim 9$–11 from CLASH (Zheng et al. 2012; Coe et al. 2013; Bouwens et al. 2014a: *light blue circles*) and Oesch et al. (2013: *light blue circles*). The $z \sim 9$–11 constraints on the UV luminosity density have been adjusted upwards to a limiting magnitude of -17.0 mag assuming a faint-end slope α of -2.0 (consistent with our constraints on α at both $z \sim 7$ and $z \sim 8$).
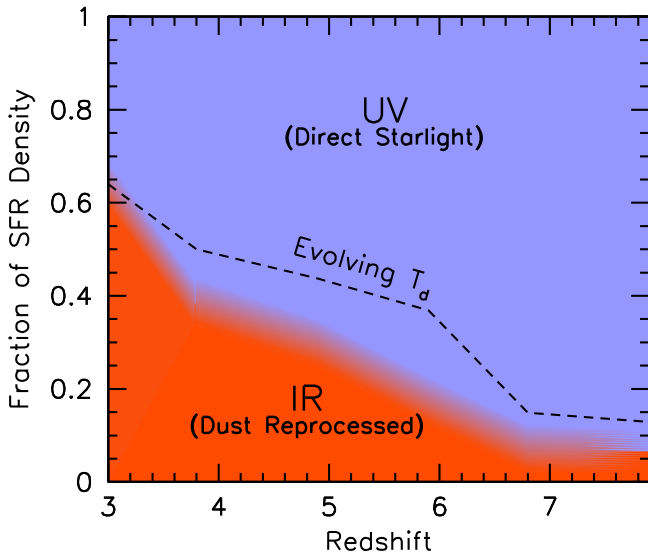
Figure 16. Fraction of the SFR density that would be directly observed in the IR and in the rest-frame UV according to our fiducial estimates of SFR density (Table 8). The dashed line gives the dividing line for our fiducial scenario of evolving T_d (35 K $\times$ $((1 + z)/2.5)^{0.32}$: see Section 3.1.3). The present figure represents an update to Figure 12 from Bouwens et al. (2009). Similar to the conclusions from Bouwens et al. (2009), we find that most of the SFR density at $z \gtrsim 3.5$ appears to be directly observable in the rest-frame UV (see also Burgarella et al. 2013; Bourne et al. 2016; Dunlop et al. 2016).

production efficiency assuming that dust extinction is zero, repeating the estimates made in Bouwens et al. (2015c). This is almost certainly an extreme case, because even lower-mass galaxies likely show a small amount of dust extinction. Our new results for this efficiency factor ξ_{ion} are presented in

Figure 17 as a function of UV luminosity. We compare the case of no dust extinction with the case in which all galaxies exhibit dust extinction according to Calzetti et al. (2000), and using similar dust extinction for nebular lines and the UV continuum.

The impact is fairly dramatic. The Lyman-continuum photon production efficiency $\log_{10} \xi_{ion}/(Hz\ erg\ s^{-1})$ that we derive is $25.51^{+0.03}_{-0.03}$, which is ~ 1.6 times higher than the estimates of Bouwens et al. (2015c) assuming a dust law according to Calzetti et al. (2000) or an SMC one. This is very close to the efficiency of $25.53^{+0.06}_{-0.06}$ that Bouwens et al. (2015c) had previously derived for $z \sim 4$–5 galaxies with the bluest UV continuum slopes β ($\beta < -2.3$) and very close to the values suggested by the stellar population models including the impact of binary stars on the evolution (e.g., Stanway et al. 2016; Wilkins et al. 2016b) or suggested by models including stellar rotation (e.g., Topping & Shull 2015).

Such a production efficiency is equivalent to $z \sim 5$ star-forming galaxies producing ~ 1.8 times as many ionizing photons per UV continuum photon as expected from standard stellar population models (which we take to be $10^{25.2}$ to $10^{25.3}$ (Hz erg s^{-1}) consistent with the use in the literature). In calculating this efficiency, we have assumed that the escape fraction is 0. If we assume that the escape fraction from galaxies is sufficient to reproduce observed constraints on the ionizing emissivity of the universe at $z \sim 4.4$ (Becker & Bolton 2013), this would translate into a 0.02 dex higher mean ξ_{ion}.

To determine the impact of this higher efficiency factor on reionization modeling, we take advantage of the modeling results from Bouwens et al. (2015c). Bouwens et al. (2015c) demonstrate that ionizing emissivity derived from observed $z \geqslant 6$ galaxies matches that inferred from other observations (*Planck*, Lyα emission fractions, etc.) if the following
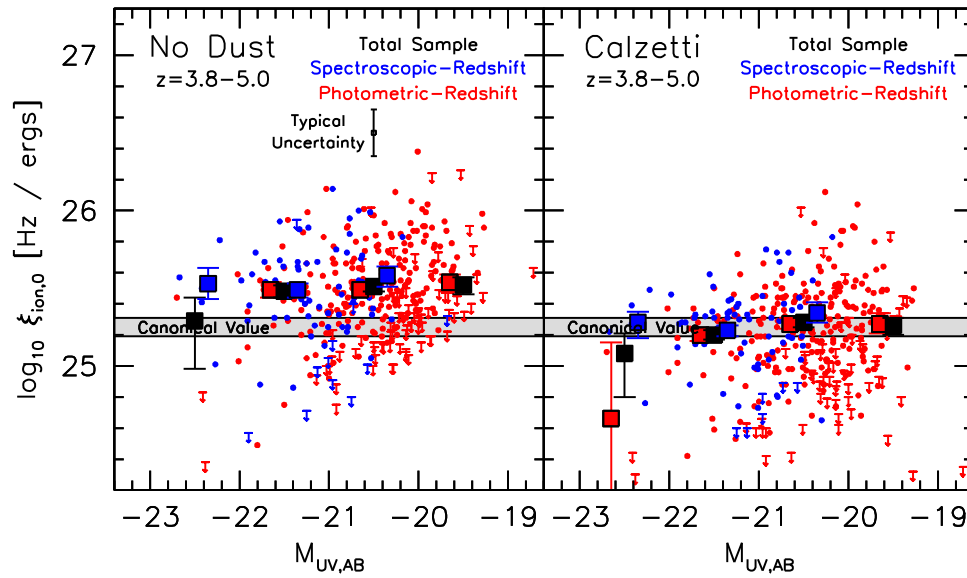
Figure 17. Left panel: New estimates of the Lyman-continuum photon production efficiencies ξ_{ion} in $z = 4$–5 galaxies (following Bouwens et al. 2015c) using IRAC-based Hα luminosities and *HST*-based UV luminosities. Sources where spectroscopic redshifts or well-determined photometric redshifts place the Hα line in a specific IRAC band are indicated by the blue and red points, respectively. 1σ upper limits are included on this diagram with downward arrows in cases where the Hα emission line is not detected at 1σ in the photometry. The solid red and blue squares indicate the mean value of ξ_{ion} for red and blue colored points, while the solid black squares indicate the mean values combining the samples selected by spectroscopic and photometric redshift. The gray band indicates the Lyman-continuum photon production efficiencies ξ_{ion} assumed in typical models (e.g., Madau et al. 1999; Kuhlen & Faucher-Giguère 2012; Robertson et al. 2013). The black error bar near the top of the left panel indicates the typical uncertainties in the derived ξ_{ion}'s. Right panel: Estimated Lyman-continuum photon production efficiencies ξ_{ion} if a Calzetti extinction law is assumed. The derived values are ~0.24 dex lower and were previously presented by Bouwens et al. (2015c). If dust extinction is as low in $z \sim 4$–5 galaxies as suggested using our fiducial $T_d \sim 35$ K results, it would imply that $z \sim 4$–5 galaxies produce up to ~1.8 times as many ionizing photons per unit UV luminosity as expected in conventional models.

condition applies:

$$f_{esc}\xi_{ion}f_{corr}(M_{lim})(C/3)^{-0.3} = 10^{24.50\pm0.10} \, s^{-1}/(ergs^{-1} \, Hz^{-1}) \quad (7)$$

where f_{esc} is the escape fraction, $C = \langle\rho_H^2\rangle/\langle\rho_H\rangle^2$ is the clumping factor, and where $f_{corr}(M_{lim}) = 10^{0.02+0.078(M_{lim}+13)-0.0088(M_{lim}+13)^2}$ corrects the UV luminosity density $\rho_{UV}(z = 8)$ derived to a faint-end limit of $M_{lim} = -13$ mag to account for different faint-end cut-offs. The above constraint is essentially identical to what Robertson et al. (2013) derive based on the available observations, but the above expression also shows how the result depends on the faint-end cut-off M_{lim} to the LF and the clumping factor C.

If we apply such an efficiency to the observed UV LFs and use fairly standard assumptions (integrating the observed LFs down to -13 mag and take the clumping factor C equal to 3: e.g., Robertson et al. 2013), these results would imply that galaxies can reionize the universe if the escape fraction f_{esc} is equal to $(8 \pm 2)\%$. An important corollary is that the escape fraction for $z \geqslant 6$ galaxies cannot be significantly higher than 8%. If it were higher, it would imply an ionizing emissivity from galaxies that is higher than observed. Cosmic reionization would be complete at substantially earlier times than $z \sim 6$ (i.e., $z > 6.5$).

6. SUMMARY

Here we make use of very sensitive (12.7 μJy beam^{-1}: 1σ) 1.2 mm observations to probe dust-enshrouded star formation from 330 robust $z = 2$–10, UV-selected galaxies located within a 1 arcmin^2 field within the HUDF. The present ALMA observations, taken as part of the ASPECS program, represent some of the deepest-ever continuum observations at 1.2 mm (see Papers I and II in the ASPECS series).

Thirty-five $z = 2$–10 galaxies were expected to be detected at $>2\sigma$ by extrapolating the M99 $z \sim 0$ IRX–β relation to $z \gtrsim 2$ and assuming a modified blackbody SED with dust temperature 35 K. Alternatively, using the approximate IRX–stellar mass relation at $z \sim 2$–3, the detection of 15 $z = 2$–10 galaxies was expected.

In significant contrast to these expectations, only six $z = 2$–10 Lyman-break galaxies show convincing evidence for being detected in ASPECS, after accounting for the likely spurious sources at $>2\sigma$. Only three of these $z \gtrsim 2$ sources are detected at substantially greater significance than 3σ (see Paper II (Aravena et al. 2016a) and Paper IV (Decarli et al. 2016)).

The six detected $z = 2$–10 galaxies are among the 13 sources from ASPECS with inferred stellar masses $>10^{9.75}$ $M_\odot$. No other sources show a significant detection (after accounting for the expected number of spurious $>2\sigma$ detections).

The fraction of high-mass $z = 2$–10 galaxies detected (at $>2\sigma$) is therefore 46% (6 out of 13) for stellar mass estimates $>10^{9.75}$ $M_\odot$. If we exclude the five $>10^{9.75}$ $M_\odot$ sources with poor 1.2 mm flux sensitivity (i.e., >17 μJy beam^{-1} rms), the detection fraction increases to $63^{+14}_{-17}\%$ in the $>10^{9.75}$ mass bin. These results point to stellar mass as being perhaps the best predictor of IR luminosity in $z \gtrsim 2$ galaxy samples.

Subdividing our samples of $z \gtrsim 2$ galaxies into different bins of UV luminosity, stellar mass, and UV-continuum slope β and stacking the ALMA continuum observations, we only find a meaningful detection in the stack results for $z = 2$–3 Lyman-break galaxies with stellar masses $>10^{9.75}$ $M_\odot$. Below $10^{9.75}$ $M_\odot$, we find a 2σ upper limit of 0.32 on the infrared

Table 9
Present Inferences for the IRX–β and IRX–Stellar Mass Relations for $z \sim 2$–10 Galaxies (if $T_d \sim 35$ K)

Redshift Range	Stellar Mass Range	Sample	IRX–β Relation	IRX–Stellar Mass Relation
$z \sim 2$–3	$\log_{10}(M/M_\odot) > 9.75$	ASPECS	Consistent with SMC	Consistent with consensus $z \sim 2$–3 relation
$z \sim 2$–3	$\log_{10}(M/M_\odot) < 9.75$	ASPECS	Below SMC	Consistent with consensus $z \sim 2$–3 relation
$z \sim 4$–10	$\log_{10}(M/M_\odot) > 9.75$	ASPECS, Capak et al. (2015), Willott et al. (2015)	Consistent with SMC or below?[a]	$\gtrsim$0.5 dex below consensus $z \sim 2$–3 relation[b]
$z \sim 4$–10	$\log_{10}(M/M_\odot) < 9.75$	ASPECS	Below SMC	$\gtrsim$0.5 dex below consensus $z \sim 2$–3 relation[b]

Notes.
[a] Both the present results and those of Capak et al. (2015) are suggestive of the infrared excess matching the SMC IRX–β relation or falling below it.
[b] If the dust temperature increases monotonically toward higher redshift as found by Béthermin et al. (2015), the present results could be consistent with no evolution in the consensus IRX–stellar mass relation from $z \sim 0$ to $z \sim 6$.
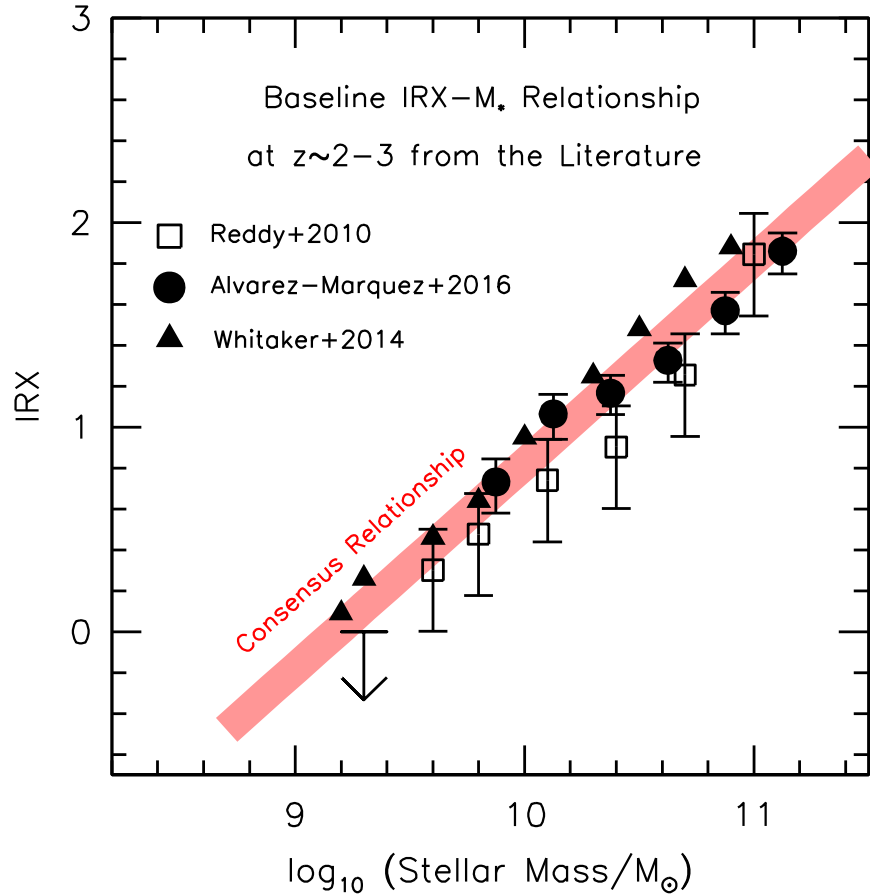
Figure 18. Consensus relationship between the infrared excess of galaxies and their stellar mass at $z \sim 2$–3. The solid circles, open squares, and solid triangles show the results from Álvarez-Márquez et al. (2016), Reddy et al. (2010), and Whitaker et al. (2014). The thick light red line show the consensus relationship (Appendix A).

excess for such galaxies, i.e., $L_{IR}/L_{UV} < 0.32$ (see also Papers II and V of this series: Aravena et al. 2016a, 2016b).

Combining the present results with previous ALMA results on UV-selected samples (i.e., Capak et al. 2015; Willott et al. 2015), we present the collective constraints on the observed infrared excess versus stellar mass at $z = 4$–6. For $T_d = 35$ K, the results point toward lower values of the infrared excess in $z > 3$ galaxies (by $\sim$0.5 dex) than in $z = 2$–3 galaxies of comparable stellar mass. However, if the dust temperature increases monotonically toward higher redshift as found by Magdis et al. (2012) and Béthermin et al. (2015), i.e., as

$(1 + z)^{0.32}$, the results are consistent with an unevolving relation between infrared excess and stellar mass to $z \sim 6$.

We also examine the dependence of the infrared excess on β. For galaxies with stellar masses $>10^{9.75} M_\odot$, the dependence we find for the infrared excess on UV-continuum slope is most consistent with an SMC IRX–β relation. However, for galaxies with stellar masses $<10^{9.75} M_\odot$, we derive 2σ upper limits on the infrared excess that lie below even the SMC IRX–β relationship. These results suggest that dust emission from lower-mass, UV-selected galaxies at $z > 3$ is low ($<40\%$) relative to emission in the rest-frame UV.

Table 10
Comparison between MIPS-inferred and ALMA-inferred IR Luminosities for Bright $z \sim 1.5$–3.0 Galaxies within ASPECS

| | | | | IR Luminosity ($10^{10}\ L_{\odot}$) | | |
| | | | | | ALMA 1.2 mm | |
ID	R.A.	Decl.	MIPS 24 μm	$T_d = 35$ K	Evolving T_d[a]	$T_d = 50$ K
			Best Detected Sources in Our ALMA Observations			
XDFU-2370746171	03:32:37.07	−27:46:17.1	20 ± 5	6 ± 2	9 ± 3	25 ± 8
XDFU-2397246112	03:32:39.72	−27:46:11.2	82 ± 1	50 ± 5	54 ± 5	222 ± 22
XDFU-2373546453	03:32:37.35	−27:46:45.3	57 ± 2	14 ± 3	17 ± 4	61 ± 13
XDFU-2385446340	03:32:38.54	−27:46:34.0	242 ± 4	97 ± 2	152 ± 3	401 ± 8
XDFU-2365446123	03:32:36.54	−27:46:12.3	5 ± 2	7 ± 3	9 ± 4	30 ± 13
XDFU-2384246348	03:32:38.42	−27:46:34.8	12 ± 7	6 ± 2	10 ± 3	25 ± 8
			Other Sources over the ASPECS field			
XDFU-2378846451	03:32:37.88	−27:46:45.1	0 ± 1	0 ± 3	0 ± 4	0 ± 13
XDFU-2379146261	03:32:37.91	−27:46:26.1	1 ± 3	0 ± 2	0 ± 3	0 ± 8
XDFU-2379146261	03:32:37.91	−27:46:26.1	3 ± 4	0 ± 2	0 ± 3	0 ± 8
XDFU-2393346236	03:32:39.33	−27:46:23.6	−1 ± 2	−2 ± 2	−3 ± 3	−8 ± 8
XDFU-2387446541	03:32:38.74	−27:46:54.1	−2 ± 2	3 ± 4	5 ± 7	12 ± 16
XDFU-2366846484	03:32:36.68	−27:46:48.4	1 ± 1	−2 ± 4	−2 ± 5	−9 ± 17
XDFU-2370846470	03:32:37.08	−27:46:47.0	2 ± 1	0 ± 3	0 ± 4	0 ± 13
XDFU-2358146436	03:32:35.81	−27:46:43.6	9 ± 3	3 ± 10	4 ± 12	13 ± 43
XDFU-2369146348	03:32:36.91	−27:46:34.8	−0 ± 1	2 ± 3	2 ± 4	9 ± 13
XDFU-2374446154	03:32:37.44	−27:46:15.4	−0 ± 1	1 ± 3	1 ± 4	4 ± 13
XDFU-2363346155	03:32:36.33	−27:46:15.5	2 ± 2	0 ± 3	0 ± 4	0 ± 13
XDFU-2382946284	03:32:38.29	−27:46:28.4	4 ± 1	−0 ± 3	−0 ± 4	−0 ± 13
XDFU-2366946210	03:32:36.69	−27:46:21.0	1 ± 1	0 ± 3	0 ± 4	0 ± 13
XDFU-2369146023	03:32:36.91	−27:46:02.3	−1 ± 3	3 ± 3	4 ± 4	13 ± 13

Note.
[a] Assuming dust temperature T_d evolves as $(35\ \mathrm{K})((1 + z)/2.5)^{0.32}$ (Béthermin et al. 2015) such that $T_d \sim 44$–50 K at $z \sim 4$–6. See Section 3.1.3.
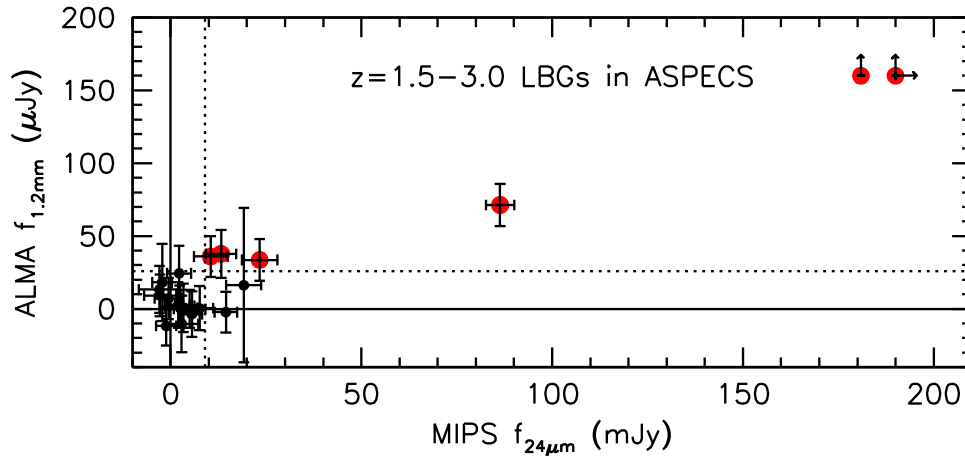
Figure 19. Comparison of the observed MIPS 24 μm fluxes (Whitaker et al. 2014) for sources in our $z \sim 1.5$–3.0 LBG sample with the 1.2 mm continuum fluxes measured from ASPECS (solid black circles with 1σ error bars shown). The larger solid red circles correspond to the sources for which we claim detections or tentative ALMA 1.2 mm detections. The arrows indicate that the measured fluxes lie outside the bounds of the figure. The horizontal and vertical dotted lines show the approximate flux levels where 2σ detections are expected. The MIPS 24 μm fluxes exhibit a broad correlation with the ALMA 1.2 mm fluxes for $z \sim 1.5$–3.0 galaxies, and those sources that are detected at $>2\sigma$ in the ALMA observations also tend to show significant $>2\sigma$ detections in the MIPS observations (see Table 10).

However, if the dust temperature is higher at $z \sim 4$–10, i.e., $T_d \sim 44$–50 K as suggested by the results of Magdis et al. (2012) and Béthermin et al. (2015), the present limits would be ~ 3 times less stringent.

Based on our combined results with Capak et al. (2015) and Willott et al. (2015), we present a crude prescription for the probable infrared excesses in $z \geqslant 3$ galaxies (Section 4.2). For galaxies with stellar masses $>10^{9.75}\ M_{\odot}$, we use an IRX–β relationship intermediate between M99 and SMC to estimate

the probable infrared excesses in galaxies. However, for galaxies with stellar masses $<10^{9.75}\ M_{\odot}$, stellar mass appears to be the best guide. Table 9 summarizes the implications of the ASPECS data set for the IRX–β and IRX–stellar mass relationship as a function of redshift and stellar mass.

We apply this dust prescription to current state-of-the-art catalogs of $z = 4$–8 galaxies to estimate the approximate dust extinction at a given UV luminosity. From this, we derive the SFR density at $z = 3$–10 (Table 8). For redshift-independent

Table 11
Multiplicative Factors to Convert Fiducial Results here for Other Model SEDs

Far-IR SED Model	Conversion Factor to Apply to the Fiducial IR Luminosities and Limits ($L_\odot$) Derived Here[a]								
	$z \sim 2$	$z \sim 3$	$z \sim 4$	$z \sim 5$	$z \sim 6$	$z \sim 7$	$z \sim 8$	$z \sim 9$	$z \sim 10$
35 K modified blackbody[b] (*fiducial*)	1.0	1.0	1.0	1.0	1.0	1.0	1.0	1.0	1.0
Modified blackbody with evolving T_d[b,c]	1.3	1.8	2.2	2.6	2.8	2.7	2.3	1.9	1.5
25 K modified blackbody[b]	0.3	0.3	0.4	0.4	0.5	0.7	1.0	1.4	2.1
30 K modified blackbody[b]	0.5	0.6	0.6	0.6	0.7	0.8	0.9	1.0	1.2
40 K modified blackbody[b]	1.7	1.7	1.6	1.5	1.5	1.4	1.3	1.2	1.1
45 K modified blackbody[b]	2.8	2.6	2.5	2.3	2.1	1.9	1.7	1.5	1.3
50 K modified blackbody[b]	4.3	4.0	3.7	3.4	3.0	2.7	2.3	1.9	1.6
NGC 6946[d]	0.3	0.3	0.4	0.4	0.5	0.7	0.8	1.1	1.5
M51[d]	0.3	0.3	0.4	0.4	0.5	0.7	0.8	1.1	1.4
Arp 220[d]	1.5	1.5	1.5	1.5	1.5	1.5	1.4	1.2	1.1
M82[d]	2.4	2.4	2.4	2.3	2.3	2.2	2.1	1.9	1.7

Notes.
[a] If the typical SED for star-forming galaxies at $z \gtrsim 3$ is any of the following, the following multiplicative conversion factors should applied to fiducial IR luminosities presented throughout this paper.
[b] Standard modified blackbody form (e.g., Casey 2012).
[c] Assuming dust temperature T_d evolves as $(35 \text{ K}) ((1 + z)/2.5)^{0.32}$ (Béthermin et al. 2015). See Section 3.1.3.
[d] Empirical SED template fits to these galaxies (Silva et al. 1998).

dust temperatures $T_d \sim 35$ K, our results point toward lower SFR density estimates at $z \gtrsim 4$ than inferred in the past (by factors of $\sim$2: see also Capak et al. 2015). Nevertheless, if the dust temperature is higher at $z \gtrsim 4$ than $T_d \sim 35$ K, the inferred SFR density would still be lower (than previous estimates), but not by as much.

The present results also help us to interpret the high ratios of Hα to UV-continuum luminosity in high-redshift galaxies (e.g., Shim et al. 2011). If dust does not have a large impact the observed Hα and UV-continuum fluxes from these galaxies, the observed luminosity ratios are close to the intrinsic ones. Star-forming galaxies at $z \sim 5$ would then produce up to $\sim$1.8 times as many ionizing photons per UV continuum photon as expected from standard stellar population models.

This would imply that star-forming galaxies can reionize the universe even if the escape fraction is just $(8 \pm 2)\%$. In fact, if true, the escape fraction cannot be higher than 8% because it would imply a higher ionizing emissivity from galaxies than is observed (e.g., Mitra et al. 2013, 2015; Bouwens et al. 2015b), requiring that the universe finish reionization earlier than $z \sim 6$ (i.e., $z > 6.5$).

Given the small number of detected sources in our deep-continuum probe and the large uncertainties on the IR luminosities of especially faint sources, the ASPECS program represents but a first step. With future observations, we can probe dust emission from galaxies at even lower masses in the high-redshift universe, while also probing much larger areas to improve the overall statistics.

APPENDIX A
CONSENSUS RELATIONSHIP BETWEEN THE INFRARED EXCESS OF GALAXIES AT $z \sim 2$–3 AND THEIR INFERRED STELLAR MASSES

There have been a large number of different measurements of the infrared excess in galaxies as a function of their stellar mass from $z \sim 0$ to $z \sim 3$ (e.g., Pannella et al. 2009; Reddy et al. 2010; Whitaker et al. 2014; Álvarez-Márquez et al. 2016). To simplify the comparisons we make against these expectations, we aim to derive a consensus determination of the infrared excess versus apparent stellar mass that provides a reasonable representation of each determination. Toward this end, in Figure 18, we present three significant recent determinations of the infrared excess of $z \sim 2$–3 galaxies versus the stellar mass. The results are presented with the thick

Table 12
Stacked Results: IRX versus Stellar Mass

Mass (M)	# of sources	$\log_{10}$ $M_{wht}/$ $M_\odot$	β_{wht}	Measured $f_{1.2mm}$ flux (μJy)[a,b]	Predicted $f_{1.2mm}$ flux (μJy) Mass[c,d]	Measured IRX[a,b,d]	Measured $f_{1.2mm}/$ f_{UV}[a,b,e]
				$z = 2$–3			
						(if T_d higher at $z > 2$,[f] multiply by $\sim$1.5–2.0$\times$)	
$>10^{9.75}\,M_\odot$	11	10.0	-1.4	$104^{+91}_{-65} \pm 7$	261	$3.80^{+3.61}_{-2.40} \pm 0.19$	$120^{+92}_{-62} \pm 6$
$>10^{9.75}M_\odot$ (excluding AGN)	10	9.9	-1.5	$103^{+98}_{-68} \pm 7$	254	$3.68^{+3.86}_{-2.55} \pm 0.19$	$112^{+94}_{-67} \pm 6$
$>10^{9.75}M_\odot$ (excluding $\geqslant 4\sigma$ detected sources)	8	9.9	-1.6	$28^{+4}_{-4} \pm 9$	224	$0.74^{+0.25}_{-0.15} \pm 0.21$	$29^{+4}_{-3} \pm 8$
$10^{9.25}M_\odot - 10^{9.75}M_\odot$	11	9.4	-1.6	$8^{+5}_{-10} \pm 9$	68	$0.12^{+0.29}_{-0.52} \pm 0.40$	$4^{+8}_{-10} \pm 11$
$10^{8.75}M_\odot - 10^{9.25}M_\odot$	24	9.0	-1.7	$9^{+6}_{-4} \pm 5$	6	$1.77^{+1.15}_{-1.02} \pm 0.94$	$70^{+46}_{-35} \pm 34$
$<10^{8.75}M_\odot$	116	8.4	-1.9	$-6^{+6}_{-6} \pm 4$	1	$-1.41^{+1.35}_{-1.19} \pm 0.90$	$-57^{+55}_{-56} \pm 38$
$<10^{9.75}M_\odot$	151	9.2	-1.7	$6^{+4}_{-6} \pm 7$	50	$0.11^{+0.32}_{-0.42} \pm 0.34$	$6^{+9}_{-10} \pm 10$
				$z = 4$–10			
						(if T_d higher at $z > 2$,[f] multiply by $\sim$2.5–3.0$\times$)	
$M > 10^{9.75}M_\odot$	2	9.8	-1.7	$-4^{+9}_{-14} \pm 13$	118	$-0.49^{+0.69}_{-1.13} \pm 0.71$	$-41^{+56}_{-44} \pm 45$
$10^{9.25}M_\odot - 10^{9.75}M_\odot$	5	9.4	-1.5	$15^{+3}_{-8} \pm 13$	117	$0.33^{+0.10}_{-0.17} \pm 0.30$	$27^{+13}_{-26} \pm 31$
$10^{8.75}M_\odot - 10^{9.25}M_\odot$	19	9.0	-1.9	$-1^{+10}_{-4} \pm 11$	29	$0.13^{+0.44}_{-0.17} \pm 0.27$	$23^{+18}_{-21} \pm 34$
$<10^{8.75}M_\odot$	142	8.4	-1.9	$-2^{+3}_{-1} \pm 7$	5	$-0.17^{+0.31}_{-0.32} \pm 0.40$	$-15^{+57}_{-57} \pm 65$
$<10^{9.75}M_\odot$	166	9.0	-1.8	$4^{+5}_{-5} \pm 7$	56	$0.14^{+0.15}_{-0.14} \pm 0.18$	$21^{+11}_{-16} \pm 22$
				$z = 2$–10			
						(if T_d higher at $z > 2$,[f] multiply by $\sim$2.5$\times$)	
$<10^{9.75}M_\odot$	317	9.1	-1.8	$5^{+4}_{-4} \pm 6$	55	$0.14^{+0.14}_{-0.13} \pm 0.16$	$8^{+7}_{-7} \pm 9$
$<10^{9.25}M_\odot$	301	8.8	-1.9	$-1^{+4}_{-3} \pm 7$	19	$0.04^{+0.18}_{-0.16} \pm 0.21$	$15^{+21}_{-21} \pm 19$

Notes.
[a] This column presents stack results. Each source is weighted according to the square of its expected 1.2 mm signal in our continuum observations (assuming $L_{IR} \propto L_{UV}$) and the inverse square of the noise. The weightings are therefore independent of stellar mass and UV-continuum slope β.
[b] Both the bootstrap and formal uncertainties are quoted on the result (presented in that order).
[c] The 1.2 mm continuum flux predicted from the consensus $z \sim 2$–3 IRX–stellar mass relationship weighting individual sources in exactly the same way as for the measured 1.2 mm continuum flux. This column should therefore be directly comparable with the column directly to the left, i.e., giving the measured flux.
[d] Assuming a standard modified blackbody SED with dust temperature of 35 K and accounting for the impact of the CMB on the measured flux (da Cunha et al. 2013b).
[e] Results do not depend on the assumed far-IR SED template.
[f] The suggested multiplicative factors are for the scenario in which the dust temperature T_d evolves as $(35\,K)((1 + z)/2.5)^{0.32}$ (Béthermin et al. 2015) such that $T_d \sim 44$–50 K at $z \sim 4$–6. See Section 3.1.3.

light red line and have the form

$$\log_{10} \mathrm{IRX} = \log_{10}[M/M_\odot] - 9.17 \qquad (8)$$

It is clear that this relationship provides an approximate match to the results from each of the three studies (if some allowance is made for modest systematics from one study to another).

APPENDIX B
COMPARISON BETWEEN MIPS-INFERRED AND ALMA-INFERRED INFRARED LUMINOSITIES

Our ALMA continuum observations allow us to set important constraints on dust emission from $z \gtrsim 3$ galaxies. However, these constraints depend significantly on the assumptions we make regarding the form of the far-IR SEDs.

As a sanity check on the present result, we derive independent estimates of the IR luminosities for $z = 1.5$–3.0 galaxies in our selection using deep 24 μm MIPS observations over GOODS-South. The apparent luminosity of $z \sim 2$ galaxies in the 24 μm band, i.e., rest-frame 8 μm, is known to be well correlated with the IR luminosity of distant galaxies.

To convert the measured 8 μm luminosities of sources (L_8) to the equivalent luminosity in the IR, i.e., L_{IR}, we use the prescription of Reddy et al. (2010). For the highest-luminosity sources, the galaxy is assumed to be optically thick, suggesting the following formula:

$$\log[L_{IR}/L_\odot] = (0.95 \pm 0.10)\log_{10}[L_8/L_\odot] + (1.49 \pm 0.87) \qquad (9)$$

Table 13
IRX Versus β

β	# of sources	$\log_{10}$ $M_{\mathrm{wht}}/M_{\odot}$	β_{med}	Measured $f_{1.2\mathrm{mm}}$ $(\mu\mathrm{Jy})^{\mathrm{a,b}}$	Predicted $f_{1.2\mathrm{mm}}$ $(\mu\mathrm{Jy})$ Calz.$^{\mathrm{c,d}}$	SMC$^{\mathrm{c,d}}$	Measured IRX$^{\mathrm{a,b,d}}$	Predicted IRX$_{\mathrm{SMC}}^{\mathrm{c}}$	Measured $f_{1.2\mathrm{mm}}/f_{\mathrm{UV}}^{\mathrm{a,b,e}}$
				$z=2\text{–}3$ (All Masses)					
							(if T_d higher at $z>2$,$^{\mathrm{f}}$ multiply by $\sim1.5\text{–}2.0\times$)		
$-4.0<\beta<-1.75$	90	9.6	-1.9	$20^{+3}_{-13}\pm10$	49	12	$0.43^{+0.12}_{-0.32}\pm0.24$	0.34	$20^{+5}_{-8}\pm10$
$-1.75<\beta<-1.25$	51	9.5	-1.4	$10^{+7}_{-7}\pm8$	183	19	$0.51^{+0.47}_{-0.47}\pm0.45$	1.27	$12^{+13}_{-15}\pm12$
$-1.25<\beta$	21	10.1	-1.0	$176^{+156}_{-122}\pm8$	512	71	$6.69^{+6.14}_{-4.55}\pm0.26$	2.70	$161^{+158}_{-103}\pm7$
$-1.25<\beta$ (excluding AGN)	20	10.1	-1.0	$175^{+150}_{-129}\pm8$	494	70	$6.47^{+5.88}_{-4.90}\pm0.26$	2.62	$151^{+163}_{-102}\pm7$
$-1.25<\beta$ (excluding $\geqslant4\sigma$ individual detections)	18	10.1	-1.1	$32^{+4}_{-32}\pm12$	368	62	$0.87^{+0.17}_{-0.94}\pm0.35$	2.14	$29^{+4}_{-17}\pm11$
All	162	9.8	-1.5	$82^{+63}_{-49}\pm6$	145	37	$2.96^{+2.53}_{-1.80}\pm0.16$	1.41	$92^{+63}_{-49}\pm5$
				$z=2\text{–}3$ ($>10^{9.75}\,M_{\odot}$)					
$-4.0<\beta<-1.75$	1	9.8	-2.0	$26^{+0}_{-0}\pm14$	48	13	$0.54^{+0.00}_{-0.00}\pm0.29$	0.49	$23^{+0}_{-0}\pm13$
$-1.75<\beta<-1.25$	2	9.8	-1.4	$22^{+11}_{-16}\pm13$	163	24	$1.31^{+0.67}_{-0.94}\pm0.72$	2.32	$40^{+1}_{-17}\pm19$
$-1.25<\beta$ (excluding AGN)	8	10.1	-1.0	$179^{+135}_{-121}\pm8$	519	72	$6.79^{+5.38}_{-4.51}\pm0.26$	4.72	$164^{+147}_{-91}\pm7$
$-1.25<\beta$ (excluding $\geqslant4\sigma$ individual detections)	5	10.1	-1.1	$33^{+3}_{-33}\pm12$	376	63	$0.90^{+0.12}_{-0.82}\pm0.36$	2.13	$29^{+2}_{-23}\pm11$
				$z=2\text{–}3$ ($<10^{9.75}\,M_{\odot}$)					
$-4.0<\beta<-1.75$	89	9.2	-1.9	$8^{+5}_{-13}\pm10$	51	11	$0.19^{+0.40}_{-0.75}\pm0.44$	0.48	$15^{+12}_{-21}\pm16$
$-1.75<\beta<-1.25$	49	9.3	-1.4	$2^{+4}_{-3}\pm10$	196	16	$-0.01^{+0.36}_{-0.36}\pm0.58$	1.24	$-4^{+8}_{-8}\pm15$
$-1.25<\beta$	13	9.0	-1.0	$-6^{+12}_{-9}\pm9$	78	10	$-0.14^{+5.04}_{-3.45}\pm2.11$	2.58	$22^{+92}_{-47}\pm51$
				$z=4\text{–}10$ (All masses)					
							(if T_d higher at $z>2$,$^{\mathrm{f}}$ multiply by $\sim2.5\text{-}3.0\times$)		
$-4.0<\beta<-1.75$	123	8.9	-2.0	$-2^{+5}_{-3}\pm8$	40	9	$0.05^{+0.22}_{-0.13}\pm0.23$	0.26	$9^{+18}_{-19}\pm28$
$-1.75<\beta<-1.25$	29	9.4	-1.5	$14^{+4}_{-8}\pm12$	310	44	$0.33^{+0.11}_{-0.14}\pm0.29$	1.19	$37^{+16}_{-10}\pm31$
$-1.25<\beta$	12	9.4	-1.0	$-14^{+8}_{-4}\pm9$	141	23	$-1.39^{+0.41}_{-0.32}\pm0.90$	2.53	$-89^{+3}_{-75}\pm58$
All	168	9.1	-1.8	$4^{+5}_{-4}\pm6$	145	23	$0.10^{+0.13}_{-0.13}\pm0.18$	0.70	$9^{+15}_{-16}\pm19$
				$z=2\text{–}10$ ($<10^{9.75}M_{\odot}$)					
							(if T_d higher at $z>2$,$^{\mathrm{f}}$ multiply by $\sim2.5\times$)		
$-4.0<\beta<-1.75$	211	8.9	-2.0	$0^{+5}_{-4}\pm7$	43	9	$0.07^{+0.20}_{-0.18}\pm0.21$	0.31	$13^{+10}_{-16}\pm14$
$-1.75<\beta<-1.25$	78	9.3	-1.5	$12^{+4}_{-7}\pm10$	287	39	$0.27^{+0.11}_{-0.17}\pm0.26$	1.20	$3^{+8}_{-9}\pm13$
$-1.25<\beta$	24	8.8	-0.8	$-5^{+3}_{-4}\pm8$	141	19	$-0.74^{+1.32}_{-1.49}\pm1.20$	3.24	$13^{+75}_{-48}\pm49$

Notes.

[a] This column presents stack results. Each source is weighted according to the square of its expected 1.2 mm signal in our continuum observations (assuming $L_{\mathrm{IR}}\propto L_{\mathrm{UV}}$) and the inverse square of the noise. The weightings are therefore independent of stellar mass and UV-continuum slope β.

[b] Both the bootstrap and formal uncertainties are quoted on the result (presented in that order).

[c] The 1.2 mm continuum flux predicted using the M99 or SMC IRX–β relationship weighting individual sources in exactly the same way as for the measured 1.2 mm continuum flux, so these two quantities should be directly comparable.

[d] Assuming a standard modified blackbody SED with dust temperature of 35 K and accounting for the impact of the CMB on the measured flux (da Cunha et al. 2013b).

[e] Results do not depend on the assumed far-IR SED template.

[f] The suggested multiplicative factors are for the scenario in which the dust temperature T_d evolves as $(35\ \mathrm{K})((1+z)/2.5)^{0.32}$ (Béthermin et al. 2015). See Section 3.1.3.

where we have modified the prescription from Reddy et al. (2010) to be in terms of the IR luminosity instead of the SFR. For lower-luminosity sources, it is more appropriate to assume that galaxies are less optically thick. Reddy et al. (2010) suggest the following prescription in this case:

$$\log[L_{\mathrm{IR}}/L_{\odot}] = (1.37\pm0.16)\log_{10}[L_8/L_{\odot}] - (3.01\pm1.34) \qquad (10)$$

Table 14
IRX Versus Apparent Magnitude in the Rest-frame UV ($m_{UV,AB}$)

m_{UV}	# of sources	$\log_{10}$ $M_{med}/M_\odot$	β_{med}	Measured $f_{1.2mm}$ (μJy)[a]	Predicted $f_{1.2mm}$ (μJy) Calz.[a]	SMC[a]	Mass[a]	IRX[a]	$f_{1.2mm}/f_{UV}$[a]
						$z = 2$–3			
								(if T_d higher at $z > 2$,[b] multiply by ~1.5–2.0×)	
<25	12	9.9	−1.5	$95^{+79}_{-56} \pm 7$	275	40	239	$3.45^{+3.23}_{-2.09} \pm 0.18$	$100^{+69}_{-52} \pm 5$
<25 (excluding AGN)	11	9.9	−1.5	$94^{+83}_{-55} \pm 7$	266	40	233	$3.34^{+3.27}_{-2.13} \pm 0.18$	$93^{+75}_{-55} \pm 5$
<25 (excluding ≥4σ detected sources)	9	9.8	−1.7	$26^{+4}_{-4} \pm 8$	163	29	201	$0.71^{+0.19}_{-0.13} \pm 0.20$	$24^{+4}_{-5} \pm 6$
25–31	150	9.3	−1.5	$-1^{+3}_{-3} \pm 4$	115	14	46	$-0.20^{+0.44}_{-0.20} \pm 0.45$	$-4^{+19}_{-20} \pm 18$
All	162	9.8	−1.5	$82^{+64}_{-49} \pm 6$	253	37	213	$2.96^{+2.56}_{-1.83} \pm 0.16$	$92^{+62}_{-48} \pm 5$
						$z = 4$–10			
								(if T_d higher at $z > 2$,[b] multiply by ~2.5–3.0×)	
<26	7	9.1	−1.9	$-3^{+6}_{-3} \pm 10$	64	13	43	$-0.09^{+0.17}_{-0.13} \pm 0.26$	$-11^{+19}_{-23} \pm 26$
26–31	160	8.8	−1.8	$4^{+4}_{-4} \pm 5$	56	11	16	$0.20^{+0.26}_{-0.24} \pm 0.30$	$30^{+43}_{-41} \pm 48$
All	168	9.1	−1.8	$4^{+5}_{-5} \pm 6$	145	23	60	$0.10^{+0.14}_{-0.14} \pm 0.18$	$9^{+14}_{-19} \pm 19$

Notes.
[a] Calculated identically to the columns in Table 12, but using the subdivisions of sources indicated in the rows of this table.
[b] The suggested multiplicative factors are for the scenario in which the dust temperature T_d evolves as $(35 \text{ K})((1 + z)/2.5)^{0.32}$ (Béthermin et al. 2015) such that $T_d \sim 44$–50 K at $z \sim 4$–6. See Section 3.1.3.

The 24 μm flux measurements we use for sources are from Whitaker et al. (2014) and rely on the original MIPS data from the GOODS program. They were derived using the same Mophongo software package (e.g., as used in Labbé et al. 2006, 2010; Skelton et al. 2014) as we use to perform IRAC photometry for samples in this paper.

The results are presented in Table 10, and it is clear that there is a good correlation between the MIPS-derived IR luminosities and the ALMA-derived luminosities assuming different dust temperatures of 35 K and 50 K, and also allowing for a monotonically increasing dust temperature toward high redshift following the results of Béthermin et al. (2015).

In general, the MIPS-derived IR luminosities we compute are ~0.3 dex higher than our ALMA-derived IR luminosities, if we adopt a fiducial dust temperature of 35 K, but agree better with these luminosities if we allow the dust temperature to increase somewhat toward higher redshift or adopt a dust temperature of 50 K. Figure 19 illustrates the generally good correlation between the observed 24 μm fluxes and the ALMA 1.2 mm fluxes.

Unfortunately, all aspects of this comparison are uncertain, from source-to-source variations in T_d (Elbaz et al. 2011; da Cunha et al. 2015; Genzel et al. 2015), to the conversion from MIPS 24 μm luminosities to IR luminosities, to the extension of these results to fainter, lower-mass $z = 2$–10 galaxies.

Because of these uncertainties, we persist with the 35 K dust temperature preferred as a compromise between different studies and compute IR luminosities using this assumption. In making this assumption, however, we should realize that our results change by ~0.3–0.5 dex if the dust temperatures we have assumed are too low or too high.

APPENDIX C
CONVERTING THE PRESENT RESULTS TO THOSE APPROPRIATE FOR OTHER ASSUMED SEDs

The IR luminosities and obscured SFRs we quote depend on the form we assume for the far-IR SED. To help our audience convert the present results to the equivalent results for other assumed far-IR SEDs, we have calculated multiplicative factors to allow for such conversions.

We provide these conversion factors in Table 11. Inspecting the results in this table, we can see that our $z \sim 7$–10 results are the least sensitive to the assumed SED shape while our $z \sim 2$–3 results show the greatest dependence. In general, the form of the SED introduces a systematic uncertainty of ~0.2 dex in the overall results at $z \sim 4$–10.

APPENDIX D
COMPREHENSIVE PRESENTATION OF STACK RESULTS

The purpose of this appendix is to provide a much more comprehensive presentation of the stack results from ASPECS than is convenient for the main text. Tables 12–14 show our results for $z \sim 2$–10 samples split by stellar mass, UV-continuum slope β, and apparent magnitude in the UV. The stack results are alternatively presented including or excluding galaxies individually detected at $>4\sigma$ or which show evidence for an AGN (XDFU-2397246112).

REFERENCES

Álvarez-Márquez, J., Burgarella, D., Heinis, S., et al. 2016, A&A, 587, A122
Aravena, M., Decarli, R., Walter, F., et al. 2016a, ApJ, 833, 68 (Paper II)
Aravena, M., Decarli, R., Walter, F., et al. 2016b, ApJ, 833, 71 (Paper V)

Asboth, V., Conley, A., Sayers, J., et al. 2016, MNRAS, 462, 1989
Baker, A. J., Lutz, D., Genzel, R., Tacconi, L. J., & Lehnert, M. D. 2001, A&A, 372, L37
Becker, G. D., & Bolton, J. S. 2013, MNRAS, 436, 1023
Beckwith, S. V. W., Stiavelli, M., Koekemoer, A. M., et al. 2006, AJ, 132, 1729
Bertin, E., & Arnouts, S. 1996, A&AS, 117, 39
Béthermin, M., Daddi, E., Magdis, G., et al. 2015, A&A, 573, A113
Boone, F., Clément, B., Richard, J., et al. 2013, A&A, 559, L1
Bouchet, P., Lequeux, J., Maurice, E., Prevot, L., & Prevot-Burnichon, M. L. 1985, A&A, 149, 330
Bourne, N., Dunlop, J. S., Merlin, E., et al. 2016, MNRAS, submitted (arXiv:1607.04283)
Bouwens, R., Bradley, L., Zitrin, A., et al. 2014a, ApJ, 795, 126
Bouwens, R. J., Illingworth, G. D., Franx, M., et al. 2009, ApJ, 705, 936
Bouwens, R. J., Illingworth, G. D., Franx, M., & Ford, H. 2007, ApJ, 670, 928
Bouwens, R. J., Illingworth, G. D., Oesch, P. A., et al. 2011, ApJ, 737, 90
Bouwens, R. J., Illingworth, G. D., Oesch, P. A., et al. 2012, ApJ, 754, 83
Bouwens, R. J., Illingworth, G. D., Oesch, P. A., et al. 2014b, ApJ, 793, 115
Bouwens, R. J., Illingworth, G. D., Oesch, P. A., et al. 2015a, ApJ, 803, 34
Bouwens, R. J., Illingworth, G. D., Oesch, P. A., et al. 2015b, ApJ, 811, 140
Bouwens, R. J., Smit, R., Labbé, I., et al. 2015c, ApJ, in press (arXiv:1511.08504)
Bradley, L. D., Bouwens, R. J., Ford, H. C., et al. 2008, ApJ, 678, 647
Brinchmann, J., & Ellis, R. S. 2000, ApJL, 536, L77
Bruzual, G., & Charlot, S. 2003, MNRAS, 344, 1000
Burgarella, D., Buat, V., Gruppioni, C., et al. 2013, A&A, 554, A70
Calzetti, D., Armus, L., Bohlin, R. C., et al. 2000, ApJ, 533, 682
Capak, P. L., Carilli, C., Jones, G., et al. 2015, Natur, 522, 455
Caputi, K. I., Lagache, G., Yan, L., et al. 2007, ApJ, 660, 97
Carilli, C. L., & Walter, F. 2013, ARA&A, 51, 105
Casey, C. M. 2012, MNRAS, 425, 3094
Castellano, M., Fontana, A., Grazian, A., et al. 2012, A&A, 540, A39
Castellano, M., Sommariva, V., Fontana, A., et al. 2014, A&A, 566, A19
Chabrier, G. 2003, PASP, 115, 763
Coe, D., Zitrin, A., Carrasco, M., et al. 2013, ApJ, 762, 32
Coppin, K. E. K., Geach, J. E., Almaini, O., et al. 2015, MNRAS, 446, 1293
Cucciati, O., Tresse, L., Ilbert, O., et al. 2012, A&A, 539, A31
da Cunha, E., Charlot, S., & Elbaz, D. 2008, MNRAS, 388, 1595
da Cunha, E., Groves, B., Walter, F., et al. 2013a, ApJ, 766, 13
da Cunha, E., Walter, F., Decarli, R., et al. 2013b, ApJ, 765, 9
da Cunha, E., Walter, F., Smail, I. R., et al. 2015, ApJ, 806, 110
Daddi, E., Alexander, D. M., Dickinson, M., et al. 2007, ApJ, 670, 173
Daddi, E., Dannerbauer, H., Stern, D., et al. 2009, ApJ, 694, 1517
Dale, D. A., Aniano, G., Engelbracht, C. W., et al. 2012, ApJ, 745, 95
Dale, D. A., Gil de Paz, A., Gordon, K. D., et al. 2007, ApJ, 655, 863
de Mink, S. E., Langer, N., Izzard, R. G., Sana, H., & de Koter, A. 2013, ApJ, 764, 166
Decarli, R., Walter, F., Aravena, M., et al. 2016, ApJ, 833, 70 (Paper IV)
Dickinson, M. 2000, RSPTA, 358, 2001
Domínguez, A., Siana, B., Henry, A. L., et al. 2013, ApJ, 763, 145
Dowell, C. D., Conley, A., Glenn, J., et al. 2014, ApJ, 780, 75
Dressel, L., Wong, M. H., Pavlovsky, C., et al. 2012, Wide Field Camera 3 Instrument Handbook, Version 5.0 (Baltimore: STScI)
Duncan, K., Conselice, C. J., Mortlock, A., et al. 2014, MNRAS, 444, 2960
Dunlop, J. S., McLure, R. J., Biggs, A. D., et al. 2016, MNRAS, submitted (arXiv:1606.00227)
Dunlop, J. S., Rogers, A. B., McLure, R. J., et al. 2013, MNRAS, 432, 3520
Eales, S. A., Wynn-Williams, C. G., & Duncan, W. D. 1989, ApJ, 339, 859
Egami, E., Rex, M., Rawle, T. D., et al. 2010, A&A, 518, L12
Elbaz, D., Dickinson, M., Hwang, H. S., et al. 2011, A&A, 533, A119
Eldridge, J. J., & Stanway, E. R. 2009, MNRAS, 400, 1019
Eldridge, J. J., & Stanway, E. R. 2012, MNRAS, 419, 479
Ellis, R. S., McLure, R. J., Dunlop, J. S., et al. 2013, ApJL, 763, L7
Erb, D. K., Shapley, A. E., Pettini, M., et al. 2006a, ApJ, 644, 813
Erb, D. K., Steidel, C. C., Shapley, A. E., et al. 2006b, ApJ, 647, 128
Finkelstein, S. L., Papovich, C., Salmon, B., et al. 2012, ApJ, 756, 164
Finlator, K., Oppenheimer, B. D., & Davé, R. 2011, MNRAS, 410, 1703
Fontana, A., Dunlop, J. S., Paris, D., et al. 2014, A&A, 570, A11
Geach, J. E., Chapin, E. L., Coppin, K. E. K., et al. 2013, MNRAS, 432, 53
Genzel, R., Tacconi, L. J., Lutz, D., et al. 2015, ApJ, 800, 20
González-López, J., Riechers, D. A., Decarli, R., et al. 2014, ApJ, 784, 99
González, V., Bouwens, R., Illingworth, G., et al. 2014, ApJ, 781, 34
Gräfener, G., & Vink, J. S. 2015, A&A, 578, L2
Grazian, A., Fontana, A., de Santis, C., et al. 2006, A&A, 449, 951
Grogin, N. A., Kocevski, D. D., Faber, S. M., et al. 2011, ApJS, 197, 35

Hathi, N. P., Ryan, R. E., Jr., Cohen, S. H., et al. 2010, ApJ, 720, 1708
Holland, W. S., Bintley, D., Chapin, E. L., et al. 2013, MNRAS, 430, 2513
Hughes, D. H., Serjeant, S., Dunlop, J., et al. 1998, Natur, 394, 241
Illingworth, G. D., Magee, D., Oesch, P. A., et al. 2013, ApJS, 209, 6
Karim, A., Schinnerer, E., Martínez-Sansigre, A., et al. 2011, ApJ, 730, 61
Kennicutt, R. C., Jr. 1998, ARA&A, 36, 189
Kewley, L. J., Dopita, M. A., Leitherer, C., et al. 2013, ApJ, 774, 100
Klaas, U., Haas, M., Heinrichsen, I., & Schulz, B. 1997, A&A, 325, L21
Knudsen, K. K., Watson, D., Frayer, D., et al. 2016, MNRAS, submitted (arXiv:1603.03222)
Koekemoer, A. M., Faber, S. M., Ferguson, H. C., et al. 2011, ApJS, 197, 36
Kriek, M., Shapley, A. E., Reddy, N. A., et al. 2015, ApJS, 218, 15
Kriek, M., van Dokkum, P. G., Labbé, I., et al. 2009, ApJ, 700, 221
Kron, R. G. 1980, ApJS, 43, 305
Kuhlen, M., & Faucher-Giguère, C.-A. 2012, MNRAS, 423, 862
Kurczynski, P., Gawiser, E., Rafelski, M., et al. 2014, ApJL, 793, LL5
Labbé, I., Bouwens, R., Illingworth, G. D., & Franx, M. 2006, ApJL, 649, L67
Labbé, I., González, V., Bouwens, R. J., et al. 2010, ApJL, 708, L26
Labbé, I., Huang, J., Franx, M., et al. 2005, ApJL, 624, L81
Labbé, I., Oesch, P. A., Bouwens, R. J., et al. 2013, ApJL, 777, L19
Labbé, I., Oesch, P. A., Illingworth, G. D., et al. 2015, ApJS, 221, 23
Laidler, V. G., Papovich, C., Grogin, N. A., et al. 2007, PASP, 119, 1325
Laporte, N., Infante, L., Troncoso Iribarren, P., et al. 2016, arXiv:1602.02775
Lawrence, A., Warren, S. J., Almaini, O., et al. 2007, MNRAS, 379, 1599
Leitherer, C., Ekström, S., Meynet, G., et al. 2014, ApJS, 212, 14
Lequeux, J., Maurice, E., Prevot-Burnichon, M.-L., Prevot, L., & Rocca-Volmerange, B. 1982, A&A, 113, L15
Levesque, E. M., Leitherer, C., Ekstrom, S., Meynet, G., & Schaerer, D. 2012, ApJ, 751, 67
Lilly, S. J., Le Fevre, O., Hammer, F., & Crampton, D. 1996, ApJL, 460, L1
Madau, P., & Dickinson, M. 2014, ARA&A, 52, 415
Madau, P., Ferguson, H. C., Dickinson, M. E., et al. 1996, MNRAS, 283, 1388
Madau, P., Haardt, F., & Rees, M. J. 1999, ApJ, 514, 648
Madau, P., Pozzetti, L., & Dickinson, M. 1998, ApJ, 498, 106
Magdis, G. E., Daddi, E., Béthermin, M., et al. 2012, ApJ, 760, 6
Magnelli, B., Elbaz, D., Chary, R. R., et al. 2009, A&A, 496, 57
Magnelli, B., Elbaz, D., Chary, R. R., et al. 2011, A&A, 528, A35
Magnelli, B., Lutz, D., Saintonge, A., et al. 2014, A&A, 561, A86
Magnelli, B., Popesso, P., Berta, S., et al. 2013, A&A, 553, A132
Maiolino, R., Carniani, S., Fontana, A., et al. 2015, MNRAS, 452, 54
Marmol-Queralto, E., McLure, R. J., & Cullen, F. 2016, MNRAS, 460, 3587
McLeod, D. J., McLure, R. J., Dunlop, J. S., et al. 2015, MNRAS, 450, 3032
McLure, R. J., Dunlop, J. S., Bowler, R. A. A., et al. 2013, MNRAS, 432, 2696
Merlin, E., Fontana, A., Ferguson, H. C., et al. 2015, A&A, 582, A15
Meurer, G. R., Heckman, T. M., & Calzetti, D. 1999, ApJ, 521, 64 [M99]
Mitra, S., Choudhury, T. R., & Ferrara, A. 2015, MNRAS, 454, L76
Mitra, S., Ferrara, A., & Choudhury, T. R. 2013, MNRAS, 428, L1
Momcheva, I. G., Brammer, G. B., van Dokkum, P. G., et al. 2015, arXiv:1510.02106
Oesch, P., Labbe, I., Illingworth, G., et al. 2013a, Spitzer Proposal, 10076
Oesch, P. A., Bouwens, R. J., Carollo, C. M., et al. 2010, ApJL, 725, L150
Oesch, P. A., Bouwens, R. J., Illingworth, G. D., et al. 2013b, ApJ, 773, 75
Oesch, P. A., Bouwens, R. J., Illingworth, G. D., et al. 2014, ApJ, 786, 108
Oesch, P. A., Bouwens, R. J., Illingworth, G. D., et al. 2015, ApJ, 808, 104
Oke, J. B., & Gunn, J. E. 1983, ApJ, 266, 713
Ota, K., Walter, F., Ohta, K., et al. 2014, ApJ, 792, 34
Ouchi, M., Ellis, R., Ono, Y., et al. 2013, ApJ, 778, 102
Ouchi, M., Yamada, T., Kawai, H., & Ohta, K. 1999, ApJL, 517, L19
Pannella, M., Carilli, C. L., Daddi, E., et al. 2009, ApJL, 698, L116
Pannella, M., Elbaz, D., Daddi, E., et al. 2015, ApJ, 807, 141
Papovich, C., Dickinson, M., & Ferguson, H. C. 2001, ApJ, 559, 620
Pei, Y. C. 1992, ApJ, 395, 130
Pettini, M., Kellogg, M., Steidel, C. C., et al. 1998, ApJ, 508, 539
Pettini, M., Steidel, C. C., Adelberger, K. L., Dickinson, M., & Giavalisco, M. 2000, ApJ, 528, 96
Planck Collaboration, Ade, P. A. R., Aghanim, N., et al. 2015, arXiv:1502.01589 [PC15]
Prevot, M. L., Lequeux, J., Prevot, L., Maurice, E., & Rocca-Volmerange, B. 1984, A&A, 132, 389
Rafelski, M., Teplitz, H. I., Gardner, J. P., et al. 2015, AJ, 150, 31
Rasappu, N., Smit, R., & Labbe, I. 2016, MNRAS, 461, 3886
Reddy, N. A., Erb, D. K., Pettini, M., Steidel, C. C., & Shapley, A. E. 2010, ApJ, 712, 1070
Reddy, N. A., Kriek, M., Shapley, A. E., et al. 2015, ApJ, 806, 259
Reddy, N. A., & Steidel, C. C. 2004, ApJL, 603, L13
Reddy, N. A., & Steidel, C. C. 2009, ApJ, 692, 778

Reddy, N. A., Steidel, C. C., Fadda, D., et al. 2006, ApJ, 644, 792
Reddy, N. A., Steidel, C. C., Pettini, M., et al. 2008, ApJS, 175, 48
Riechers, D. A., Bradford, C. M., Clements, D. L., et al. 2013, Natur, 496, 329
Riechers, D. A., Carilli, C. L., Capak, P. L., et al. 2014, ApJ, 796, 84
Robertson, B. E., Furlanetto, S. R., Schneider, E., et al. 2013, ApJ, 768, 71
Rogers, A. B., McLure, R. J., & Dunlop, J. S. 2013, MNRAS, 429, 2456
Rujopakarn, W., Dunlop, J. S., Rieke, G. H., et al. 2016, ApJ, in press (arXiv:1607.07710)
Salpeter, E. E. 1955, ApJ, 121, 161
Sawicki, M., & Yee, H. K. C. 1998, AJ, 115, 1329
Schaerer, D., & de Barros, S. 2009, A&A, 502, 423
Schenker, M. A., Robertson, B. E., Ellis, R. S., et al. 2013, ApJ, 768, 196
Schiminovich, D., Ilbert, O., Arnouts, S., et al. 2005, ApJL, 619, L47
Schreiber, C., Pannella, M., Leiton, R., et al. 2016, arXiv:1606.06252
Scott, K. S., Yun, M. S., Wilson, G. W., et al. 2010, MNRAS, 405, 2260
Scoville, N., Sheth, K., Aussel, H., et al. 2016, ApJ, 820, 83
Shapley, A. E., Steidel, C. C., Erb, D. K., et al. 2005, ApJ, 626, 698
Shibuya, T., Ouchi, M., & Harikane, Y. 2015, ApJS, 219, 15
Shim, H., Chary, R.-R., Dickinson, M., et al. 2011, ApJ, 738, 69
Siana, B., Teplitz, H. I., Chary, R.-R., Colbert, J., & Frayer, D. T. 2008, ApJ, 689, 59
Siana, B., Smail, I., Swinbank, A. M., et al. 2009, ApJ, 698, 1273
Silva, L., Granato, G. L., Bressan, A., & Danese, L. 1998, ApJ, 509, 103
Skelton, R. E., Whitaker, K. E., Momcheva, I. G., et al. 2014, ApJS, 214, 24
Sklias, P., Zamojski, M., Schaerer, D., et al. 2014, A&A, 561, A149
Smit, R., Bouwens, R. J., Labbé, I., et al. 2014, ApJ, 784, 58
Smit, R., Bouwens, R. J., Labbé, I., et al. 2015, ApJ, submitted (arXiv:1511.08808)

Stanway, E. R., Eldridge, J. J., & Becker, G. D. 2016, MNRAS, 456, 485
Stark, D. P., Schenker, M. A., Ellis, R., et al. 2013, ApJ, 763, 129
Steidel, C. C., Adelberger, K. L., Giavalisco, M., Dickinson, M., & Pettini, M. 1999, ApJ, 519, 1
Szalay, A. S., Connolly, A. J., & Szokoly, G. P. 1999, AJ, 117, 68
Szécsi, D., Langer, N., Yoon, S.-C., et al. 2015, A&A, 581, A15
Tan, Q., Daddi, E., Magdis, G., et al. 2014, A&A, 569, A98
Teplitz, H. I., Rafelski, M., Kurczynski, P., et al. 2013, AJ, 146, 159
Topping, M. W., & Shull, J. M. 2015, ApJ, 800, 97
Walter, F., Decarli, R., Carilli, C., et al. 2012, ApJ, 752, 93
Walter, F., et al. 2016, submitted [ASPECS_I]
Wang, W.-H., Barger, A. J., & Cowie, L. L. 2009, ApJ, 690, 319
Watson, D., Christensen, L., Knudsen, K. K., et al. 2015, Natur, 519, 327
Whitaker, K. E., Franx, M., Leja, J., et al. 2014, ApJ, 795, 104
Wilkins, S. M., Bouwens, R. J., Oesch, P. A., et al. 2016a, MNRAS, 455, 659
Wilkins, S. M., Bunker, A., Coulton, W., et al. 2013, MNRAS, 430, 2885
Wilkins, S. M., Bunker, A. J., Stanway, E., Lorenzoni, S., & Caruana, J. 2011, MNRAS, 417, 717
Wilkins, S. M., Feng, Y., Di-Matteo, T., et al. 2016b, MNRAS, 458, L6
Willott, C. J., Carilli, C. L., Wagg, J., & Wang, R. 2015, ApJ, 807, 180
Willott, C. J., McLure, R. J., Hibon, P., et al. 2013, AJ, 145, 4
Windhorst, R. A., Cohen, S. H., Hathi, N. P., et al. 2011, ApJS, 193, 27
Wise, J. H., Turk, M. J., Norman, M. L., & Abel, T. 2012, ApJ, 745, 50
Xue, Y. Q., Luo, B., Brandt, W. N., et al. 2011, ApJS, 195, 10
Yoon, S.-C., Langer, N., & Norman, C. 2006, A&A, 460, 199
Zheng, W., Postman, M., Zitrin, A., et al. 2012, Natur, 489, 406 (Z12)